



저작자표시-비영리-변경금지 2.0 대한민국

이용자는 아래의 조건을 따르는 경우에 한하여 자유롭게

- 이 저작물을 복제, 배포, 전송, 전시, 공연 및 방송할 수 있습니다.

다음과 같은 조건을 따라야 합니다:



저작자표시. 귀하는 원저작자를 표시하여야 합니다.



비영리. 귀하는 이 저작물을 영리 목적으로 이용할 수 없습니다.



변경금지. 귀하는 이 저작물을 개작, 변형 또는 가공할 수 없습니다.

- 귀하는, 이 저작물의 재이용이나 배포의 경우, 이 저작물에 적용된 이용허락조건을 명확하게 나타내어야 합니다.
- 저작권자로부터 별도의 허가를 받으면 이러한 조건들은 적용되지 않습니다.

저작권법에 따른 이용자의 권리는 위의 내용에 의하여 영향을 받지 않습니다.

이것은 [이용허락규약\(Legal Code\)](#)을 이해하기 쉽게 요약한 것입니다.

[Disclaimer](#)

Doctor of Philosophy

**Investigation of Metal–Support Interactions
and Coking Behavior over Ni/Ce_xZr_{1-x}O₂–Al₂O₃
Catalysts for Ethanol Steam Reforming**

The Graduate School of the University of Ulsan

Department of Chemical Engineering

Mingyan Wang

**Investigation of Metal–Support Interactions and
Coking Behavior over Ni/Ce_xZr_{1-x}O₂–Al₂O₃ Catalysts for
Ethanol Steam Reforming**

Advisor: Professor Eun Woo Shin, Professor Yong Men

A Dissertation

Submitted to

the Graduate School of the University of Ulsan

In partial Fulfillment of the Requirements

for the Degree of

Doctor of philosophy

by

Mingyan Wang

Department of Chemical Engineering

Ulsan, South Korea

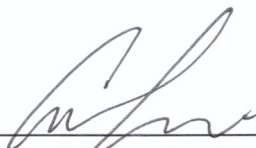
December 2023

**Investigation of Metal–Support Interactions and Coking
Behavior over Ni/Ce_xZr_{1-x}O₂–Al₂O₃ Catalysts for Ethanol Steam
Reforming**

This certifies that the dissertation of
Mingyan Wang is approved.




Committee Chair Prof. Sung Gu Kang



Committee Member Prof. Eun Woo Shin



Committee Member Prof. Yong Men



Committee Member Prof. Seung Hyun Hur



Committee Member Prof. Dong Hwi Jeong

Department of Chemical Engineering

University of Ulsan

Ulsan, South Korea

December 2023

ABSTRACT

With its abundant, renewable, and eco-friendly attributes, hydrogen stands out as a key contender in addressing climate change challenges and attaining carbon neutrality objectives. As the transition to H₂ energy is inevitable in the future, various studies have contributed to the research on H₂ global production, storage, and utilization. From the perspective of sustainable development, the reforming of low-carbon bio-alcohols derived from biomass fermentation emerges as a pivotal avenue for hydrogen production, offering nearly zero net carbon dioxide emissions. In particular, Ethanol Steam Reforming (ESR) garners significant attention, leveraging well-established ethanol production technologies from biomass and capitalizing on ethanol's advantages in terms of transport and toxicity for a prospective carbon-neutral society.

The first research investigates selective Ni locations over Ni/CeZrO_x-Al₂O₃ catalysts at different Ni loading contents and their influences on reaction pathways in ethanol steam reforming (ESR). Depending on the Ni loading contents, the added Ni selectively interacts with CeZrO_x-Al₂O₃, resulting in the stepwise locations of Ni over CeZrO_x-Al₂O₃. This behavior induces a remarkable difference in hydrogen production and coke formation in ESR. The selective interaction between Ni and CeZrO_x for 10-wt.% Ni generates more oxygen vacancies in the CeZrO_x lattice. The Ni sites near the oxygen vacancies enhance reforming via steam activation, resulting in the highest hydrogen production rate of 1863.0 mmol/gcat · min. In contrast, for 15 and 20-wt.% Ni, excessive Ni is additionally deposited on Al₂O₃ after the saturation of Ni-CeZrO_x interactions. These Ni sites on Al₂O₃ accelerate coking from the ethylene produced on the acidic sites, resulting in a high coke amount of 19.1 mgc/gcat · h (20Ni/CZ-Al).

For a deeper understanding of coke formation routes over Ni-based catalysts in ESR, in the second research, we focused on optimizing the active sites distribution via the metal-support interactions and investigating the coke precursor gasification in Ni/Ce_xZr_{1-x}O₂-Al₂O₃ (CZA) catalysts for ethanol steam reforming. We found that the optimized active sites distribution could minimize coke formation by enabling efficient gasification of a coke

precursor on Ni. In the 20Ni/40CZA catalyst, the crystalline CZ exhibited a strong interaction with Ni, maintaining a uniform distribution of highly dispersed Ni nano-particles and creating abundant oxygen vacancies on CZ, even at 20 wt% of Ni loading. Consequently, the resistance to coking over 20Ni/40CZA was significantly enhanced due to the efficient delivery of active oxygen atoms from steam on the abundant oxygen vacancies to the coke precursor on the Ni surface, resulting in fast gasification of the coke precursor.

Finally, we reduced the variables in the support and only investigated the metal–support interactions over Ni/CeO₂–ZrO₂ (Ni/CZ) catalysts for ESR. Different Ni contents (5, 10, and 15 wt%) were loaded onto the CZ support using two catalyst preparation methods, namely one-pot, and successive impregnation methods. Using the one-pot method, the Ni species over the Ni/CZ catalysts strongly interacted with the CZ support, resulting in smaller Ni nanoparticles with abundant oxygen vacancies. In contrast, the successive impregnation method mainly generated an isolated Ni phase at a high Ni content, resulting in large Ni clusters with limited oxygen vacancies. The poor Ni dispersion over the Ni/CZ catalysts prepared by the successive impregnation method induced low ethanol conversions and hydrogen production rates. In addition, the large Ni clusters over the Ni/CZ catalysts prepared by the successive impregnation method achieved a fast-coking behavior, thereby increasing the coke amount. Further, coke gasification was demonstrated to dominate the Ni surface with the Ni/CZ catalysts prepared by the one-pot method because of the high Ni dispersion and abundant oxygen vacancies.

ACKNOWLEDGMENTS

I would like to dedicate this thesis to my advisor, Professor Eun Woo Shin. His unwavering guidance, support, and profound expertise have been instrumental in successfully navigating my Ph.D. journey. Under his mentorship, I not only experienced the fun of in-depth exploration of the research but also enjoyed my life in Korea. I want to show my most sincere appreciation to Professor Yong Men at Shanghai University of Engineering Science, who introduced me to the realm of doctoral studies, sparked my interest in catalysts, and laid the solid foundation for my research.

I extend sincere gratitude to all my former and present labmates, including Thanh-Truc Pham, Nguyen Phu Huy, Do Thi Lien, Haewon Jung, Kaiming Jiang, Hongyan Yu, Kim Anh Nguyen Thi, Sang Yoon Kim, Dao Duc Quang, Phuong Anh Nguyen, Thi Van Anh Hoang, Azam Jamsaz, Nhiem Pham-Ngoc, and Chao Song. Their support not only enriched my academic pursuits but also profoundly influenced me through their outstanding qualities. Additionally, I want to thank all my friends at the University of Ulsan, including Guoen Li, Yujie Wu, Linlin Wang, Di Liu, Yuanyuan Li, Haiji Huang, Yiwen Hong, Yue Xu, Tran Van Tam, Yanchunxiao Qi, Yiming Meng, Jingwen Zhou, and Mi Tian. Their prompt assistance during challenging times and the enduring friendships cultivated are cherished treasures.

I would like to express my heartfelt gratitude to my parents, who have consistently offered support and love. Their commitment to providing me with a quality education, along with their respect and help, has shaped me into a person brimming with confidence and love for the world.

In loving memory of my grandfather, Wang Weining (王维宁), who departed from me in January 2022, I dedicate this thesis to him. Throughout my 27 years of life, he stood as my closest friend, cherished mentor, and the best grandfather. His unyielding thirst for knowledge and curiosity about the world left an indelible mark on me. Born in 1920, he experienced difficult times of war and famine but still maintained a heartfelt optimism, displaying generosity and kindness to all. During the days I lived with him, his words and deeds influenced me all the time. His boundless tolerance and unwavering support provided me with the strength to face any future challenges. In his final days, everything about him was old except his eyes and they were the same color as black gemstones, full of cheerful and vitality. May the memories of his spirit motivate us to contribute positively to the world.

TABLE OF CONTENTS

ABSTRACT	1
ACKNOWLEDGMENTS	3
TABLE OF CONTENTS	5
LIST OF TABLES	7
LIST OF FIGURES	9
LIST OF SCHEME	14
PART I - OVERVIEW OF DISSERTATION	15
Chapter 1. Introduction.....	15
1.1. Background and motivation.....	15
1.2. Research objectives	16
1.3. Outline of the dissertation	17
PART II – EXPLORING METAL-SUPPORT INTERACTIONS IN Ni/CeZrO _x -Al ₂ O ₃ CATALYSTS FOR ETHANOL STEAM REFORMING: IMPACTS ON REACTION PATHWAYS AND COKING BEHAVIOR.....	19
Chapter 2. The priority of the Ni-support interaction over Ni/CeZrO _x -Al ₂ O ₃ catalysts and their influence on reaction pathways and coke formation in ethanol steam reforming.....	19
2.1. Introduction	19
2.2. Experimental.....	21
2.2.1. Catalyst preparation.....	21
2.2.2. Catalyst characterization	22
2.2.3. Ethanol steam reforming reaction test	24
2.3. Results and discussion.....	26
2.3.1. Selective Ni-support interactions at different Ni loading contents	26
2.3.2. Reaction results of ethanol steam reforming over the xNi/CZ-Al catalysts	40
2.3.3. Coking behavior over the xNi/CZ-Al catalysts	49
2.4. Conclusions	59
Chapter 3. Optimizing the metal-support interactions by changing CZ/Al ratio over Ni/CeZrO _x - Al ₂ O ₃ catalysts to minimize coking in ethanol steam reforming via efficient gasification routes.	61
3.1. Introduction	61

3.2. Experimental	63
3.2.1. Catalyst preparation.....	63
3.2.2. Catalyst characterization	65
3.2.3. Ethanol steam reforming reaction test	67
3.3. Results	68
3.3.1 Effect of different CZ/Al ratios on physicochemical properties of the xNi/yCZA catalysts.....	68
3.3.2 Catalytic performance of ethanol steam reforming	87
3.4. Conclusions	103
PART III – ENHANCING ETHANOL STEAM REFORMING PERFORMANCE AND COKE GASIFICATION BY CATALYST SYNTHESIS METHOD OPTIMIZATION	105
Chapter 4. Metal–support interactions over Ni/CeO ₂ –ZrO ₂ catalysts for ethanol steam reforming and their effects on the coke gasification.....	105
4.1. Introduction	105
4.2. Experimental	107
4.2.1. Catalyst preparation.....	107
4.2.2. Catalyst characterization	108
4.2.3. ESR reaction test	110
4.3. Results and discussion.....	111
4.3.1 Physicochemical properties of the Ni/CZ catalysts	111
4.3.2 Catalytic performance of ESR.....	124
4.4. Conclusions	132
PART IV - SUMMARY AND RECOMMENDATIONS FOR FUTURE WORK.....	134
5.1. Summary	134
5.1.1 Developments and findings related to research objective 1	134
5.1.2 Developments and findings related to research objective 2	135
5.2. Recommendation for future work	136
References	138
LIST OF PUBLICATIONS.....	146

LIST OF TABLES

Table 2.1. Physicochemical properties of the xNi/CZ-Al catalysts.

Table 2.2. Acidic sites, Ni metallic site, and relative intensity ratio of the peaks ($I_{\text{Ce-V/Ce-O}}$) related to the oxygen vacancy of the catalysts.

Table 2.3. xNi/CZ-Al catalyst performance of the ESR reaction at 750 °C (reaction conditions: S/C = 3, GHSV = 10,619 h⁻¹).

Table 2.4. xNi/CZ-Al catalyst performance of the ESR reaction in 550 °C (reaction conditions: S/C = 3, GHSV = 10619 h⁻¹).

Table 2.5. Physicochemical properties of 10Ni/Al₂O₃ and 10Ni/CZ-Al catalysts.

Table 2.6. 10Ni/Al₂O₃ and 10Ni/CZ-Al catalyst performance of the ESR reaction in 550 °C (reaction conditions: S/C = 3, GHSV = 10619 h⁻¹).

Table 3.1. Physicochemical properties of the xNi/yCZA catalysts.

Table 3.2. Peak area percentage deconvolved from H₂-TPR and the concentration of the oxygen vacancy (V_o) of xNi/yCZA catalysts.

Table 3.3. Ni metallic site, Ni dispersion, relative intensity ratio of the peaks ($I_{\text{Ce-V/Ce-O}}$ and $O_{\text{ads.}}/(O_{\text{latt.}} + O_{\text{ads.}})$) related to the oxygen vacancy, and Ce³⁺% obtained from XPS of the catalysts.

Table 3.4. ESR reaction results over xNi/yCZA catalysts at 350 °C.

Table 3.5. ESR reaction results over xNi/yCZA catalysts at 550 °C.

Table 4.1. Physicochemical properties of the xNi/CZ catalysts.

Table 4.2. The H₂ consumption data and H₂-TPR peak areas of the catalysts

Table 4.3. The quantification of Ni metal, Ni²⁺, and Ce³⁺ contents from the XPS results.

Table 4.4. Results of the ESR of the xNi/CZ catalysts at 550 °C for 8 h.

Table 4.5. Results of the ESR of the xNi/CZ catalysts at 550 °C for 30 h.

LIST OF FIGURES

Figure 1.1. The structure of the thesis corresponding to the objectives.

Figure 2.1. Schematic setup of the fixed-bed flow reaction system for ethanol steam reforming.

Figure 2.2. (A) N₂ adsorption–desorption isotherms and (B) pore size distribution of the xNi/CZ-Al catalysts

Figure 2.3. NH₃-TPD profiles of the xNi/CZ-Al catalysts.

Figure 2.4. (A) XRD patterns, (B) Raman spectra, and (C) H₂-TPR profiles of the reduced xNi/CZ-Al catalysts: (a) CZ-Al, (b) 5Ni/CZ-Al, (c) 10Ni/CZ-Al, (d) 15Ni/CZ-Al, and (e) 20Ni/CZ-Al.

Figure 2.5. HR-TEM images of the reduced xNi/CZ-Al catalysts.

Figure 2.6. H₂-TPD profiles of the xNi/CZ-Al catalysts.

Figure 2.7. XPS data of (A) Ni 2p, (B) O 1s, and (C) Al 2p of the fresh catalysts, and relative peak areas of (D) Ni_A and Ni_S, (E) O₁ and O₂, and (F) Al₁ and Al₂ in each XPS.

Figure 2.8. X-ray photoelectron spectroscopy (XPS) spectra of (A) O 1s and (B) Al 2p of the fresh catalysts.

Figure 2.9. TGA profiles for the spent catalysts after 750 °C ESR reaction.

Figure 2.10. Gas production concentration over the xNi/CZ-Al catalyst in ESR obtained from 8 h TOS reaction.

Figure 2.11. Carbon-containing gas selectivity of the catalysts (reaction conditions: S/C = 3, T = 550 °C, GHSV = 10619 h⁻¹).

Figure 2.12. (A) H₂ production rate per gram of catalyst and per Ni active site at 550 °C. (B) Selectivity of H₂ and C₂H₄ (reaction conditions: S/C = 3, GHSV = 10619 h⁻¹).

Figure 2.13. (A) TGA profiles for the spent catalysts after 550 °C ESR reaction. (B) XRD patterns of spent xNi/CZ-Al catalysts (a) CZ-Al, (b) 5Ni/CZ-Al, (c) 10Ni/CZ-Al, (d) 15Ni/CZ-Al, and (e) 20Ni/CZ-Al.

Figure 2.14. TEM images of the spent catalysts (A) CZ-Al, (B) 5Ni/CZ-Al, (C) 10Ni/CZ-Al, (D) 15Ni/CZ-Al, and (E) 20Ni/CZ-Al. (F) Raman spectra of the spent catalysts (a) CZ-Al, (b) 5Ni/CZ-Al, (c) 10Ni/CZ-Al, (d) 15Ni/CZ-Al, and (e) 20Ni/CZ-Al after 8h 550 °C ESR reaction.

Figure 2.15. (A) XRD patterns of the reduced 10Ni/CZ-Al and 10Ni/Al₂O₃ catalysts and (B) TEM images of the reduced 10Ni/Al₂O₃ catalyst.

Figure 2.16. (A) TGA profiles for the spent catalysts. (B) XRD patterns of the spent catalysts. (C) TEM images of the spent 10Ni/Al₂O₃ catalyst after the 550 °C ESR reaction.

Figure 3.1. The scheme of the catalyst preparation.

Figure 3.2. N₂ adsorption/desorption isotherms (T=77K) obtained over (a) xNi/20CZA, (b) xNi/40CZA, and BJH pore size distribution of (c) xNi/20CZA and (d) xNi/40CZA catalysts.

Figure 3.3. NH₃-TPD profiles of (a) xNi/20CZA and (b) xNi/40CZA catalysts.

Figure 3.4. (a) XRD patterns of calcined samples of xNi/20CZA. (1) 20CZA, (2) 5Ni/20CZA, (3) 10Ni/20CZA, (4) 15Ni/20CZA, (5) 20Ni/20CZA; (b) XRD patterns of calcined samples of xNi/40CZA. (1) 40CZA, (2) 5Ni/40CZA, (3) 10Ni/40CZA, (4) 15Ni/40CZA, (5) 20Ni/40CZA; (c) relative peak intensity of CeO₂ at 28.6° to NiO at 37.3° for xNi/20CZA; (d)

relative peak intensity of CeO₂ at 28.6° to NiO at 37.3° for xNi/40CZA; (e) XRD patterns of reduced samples of xNi/20CZA. (1) 20CZA, (2) 5Ni/20CZA, (3) 10Ni/20CZA, (4) 15Ni/20CZA, (5) 20Ni/20CZA; (f) XRD patterns of reduced samples of xNi/40CZA. (1) 40CZA, (2) 5Ni/40CZA, (3) 10Ni/40CZA, (4) 15Ni/40CZA, (5) 20Ni/40CZA; (g) enlarge area indicated in Fig.3.4(e); and (h) enlarge area indicated in Fig.3.4(f).

Figure 3.5. (a) HR-TEM images and Ni particle size distribution of reduced xNi/yCZA catalysts; (b,c) relationship between Ni particle size (calculated from XRD and TEM) and Ni loading of reduced xNi/yCZA catalysts (the average Ni particle size of 5, 10Ni/20CZA, and xNi/40CZA is shown in dash line, and the average Ni particle size of 15 and 20Ni/20CZA is shown in dot line).

Figure 3.6. H₂-TPR profiles of (a) xNi/20CZA, (b) xNi/40CZA catalysts, and (c,d) the EDS mapping images of Ni and Ce for 20Ni/20CZA.

Figure 3.7. EDS mapping images of all the elements for 20Ni/20CZA.

Figure 3.8. H₂-TPD profiles of (a) xNi/20CZA and (b) xNi/40CZA catalysts.

Figure 3.9. Raman spectra of reduced (a) xNi/20CZA and (b) xNi/40CZA catalysts; (c) XPS data of O 1s for reduced xNi/yCZA; (d) $O_{ads.}/(O_{latt} + O_{ads.})$ ratio (based on XPS of O 1s) as a function of Ni loading amount.

Figure 3.10. XPS data of Ce 3d for reduced xNi/yCZA catalysts.

Figure 3.11. 8 h time on stream of gas concentrations in ESR at 350 °C for xNi/yCZA catalysts.

Figure 3.12. 8 h time on stream of gas concentrations in ESR at 550 °C for xNi/yCZA

catalysts.

Figure 3.13. (a) The ethanol conversion and average H₂ production rate run at 350 °C, (b,c) the carbon-containing products selectivity over xNi/yCZA catalysts run at 350 °C, (d) The ethanol conversion and average H₂ production rate run at 550 °C, and (e,f) the carbon-containing products selectivity over xNi/yCZA catalysts run at 550 °C (Reaction conditions: S/C = 3, GHSV = 10,619 h⁻¹).

Figure 3.14. XRD patterns of (a) the spent xNi/20CZA catalysts (1) 20CZA, (2) 5Ni/20CZA, (3) 10Ni/20CZA, (4) 15Ni/20CZA, (5) 20Ni/20CZA; (b) the spent xNi/40CZA (1) 40CZA, (2) 5Ni/40CZA, (3) 10Ni/40CZA, (4) 15Ni/40CZA, (5) 20Ni/40CZA after the 8 h reaction at 550 °C, and (c) enlarged XRD pattern of spent 20Ni/20CZA and the deconvoluted peaks.

Figure 3.15. TGA/DTG profiles of spent catalysts (a, c) xNi/20CZA; (b, d) xNi/40CZA after 8 h ESR reaction at 550 °C, and (e,f) amount of coke after 8 h ESR reaction at 550 °C calculated by TGA results as a function of Ni loading amount.

Figure 3.16. TEM images of spent xNi/yCZA catalysts used in the ESR at 550 °C.

Figure 3.17. TGA/DTG profiles of spent catalysts (a, c) xNi/20CZA; (b, d) xNi/40CZA after 8 h ESR reaction at 350 °C, and (e) acidic site concentration of the catalysts and amount of coke after 8 h ESR reaction at 350 °C calculated by TGA results as a function of Ni loading amount.

Figure 3.18. TEM images of the spent xNi/yCZA catalysts in ESR at 350 °C.

Figure 4.1. N₂ adsorption/desorption isotherms (T=77K) obtained over (a) xNi/CZ-IM, and (b) xNi/CZ-OP, and BJH pore size distribution of catalysts (insets).

Figure 4.2. (a) XRD patterns of the reduced catalysts. (b, c) Enlarged XRD patterns of xNi/CZ–OP and xNi/CZ–IM.

Figure 4.3. TEM images and EDS mapping of the prepared catalysts.

Figure 4.4. H₂-TPD profiles of the catalysts.

Figure 4.5. H₂-TPR profiles of the catalysts (based on Table 4.2).

Figure 4.6. Raman spectra of the (b) xNi/CZ–OP and (c) xNi/CZ–IM catalysts.

Figure 4.7. XPS data of Ni 2p for the reduced catalysts.

Figure 4.8. XPS data of Ce 3d for the (b) xNi/CZ–OP and (c) xNi/CZ–IM catalysts.

Figure 4.9. Gas production concentrations for the 5Ni/CZ-IM catalyst obtained from the 8 h ESR.

Figure 4.10. (a) Conversion of ethanol and average H₂ production rate, and (b, c) carbon-containing product selectivity of the xNi/CZ–IM and xNi/CZ–OP catalysts (Reaction conditions: S/C = 3, T = 550 °C, GHSV = 10619 h⁻¹).

Figure 4.11. TGA/DTG profiles of the spent catalysts after the 8-h ESR at 550 °C: (a, c) xNi/CZ–IM and (b, d) xNi/CZ–OP.

Figure 4.12. XRD patterns of the spent catalysts after the 8-h ESR at 550 °C.

Figure 4.13. (a) TGA, (b) DTG profiles, and (c) XRD patterns of the spent 15Ni/CZ–IM and 15Ni/CZ–OP catalysts after the 30-h ESR at 550 °C.

LIST OF SCHEME

Scheme 2.1. Schematic of the priority of the Ni-support interaction based on the Ni loading amounts.

Scheme 2.2. Reaction pathways occurring over the xNi/CZ-Al catalysts in ESR.

Scheme 2.3. Steam reforming and coke generation combined steam activation over Ni active sites.

Scheme 3.1. Schematic illustration of active sites over 10Ni/20CZA, 20Ni/20CZA, 10Ni/40CZA, and 20Ni/40CZA.

Scheme 3.2. Schematic illustration on coke formation and gasification over the xNi/yCZA catalysts at (a) 550 °C and (b) 350 °C.

Scheme 4.1. Illustration of the active sites over the Ni/CZ catalysts.

PART I - OVERVIEW OF DISSERTATION

Chapter 1. Introduction

1.1. Background and motivation

Relying on fossil fuels as primary energy sources has resulted in significant energy crises and environmental issues, such as the depletion of fossil fuels and the emission of pollutants. Mitigating carbon dioxide production and minimizing its concentration has emerged as a pressing global priority [1]. Scientists across the globe are striving to reduce the impact of global warming, which poses a threat to the survival of human civilization [2]. A pivotal aspect of their endeavors involves the development of clean, renewable, and sustainable energy sources. Hydrogen energy, producing only water as a byproduct, stands out as a promising solution. The widespread application of hydrogen energy across various energy and industrial sectors may offer a viable strategy for safeguarding the environment and mitigating the effects of global warming and impending catastrophes [3, 4].

H₂ is industrially manufactured using various processes, including catalytic reactions, and water electrolysis. Among these, steam reforming is a well-established and industrially dominant catalytic process used globally [5, 6]. Specifically, methane (CH₄) is commercially used as a suitable feed for steam reforming. Despite the wide use of CH₄, several works have focused on obtaining environmentally friendly alternative feeds for steam reforming. Ethanol is a potential commercial feed owing to its renewable energy source, availability in terms of transport and toxicity, and thermodynamic feasibility with a lower reaction temperature for ethanol steam reforming (ESR) [7, 8].

In steam reforming, supported noble metal catalysts using Rh, Ir, Pt, Pd, and Ru show high catalytic activity and stability, they are not suitable for industrial hydrogen production due to their high cost [9]. Alternatively, Ni-supported catalysts have been widely used among non-noble catalysts due to their excellent ability for C–C bonding cleavage and acceptable cost for practical applications [10, 11]. However, catalyst deactivation by coke and methane (CH₄) formation as a by-product is considered as a significant challenge over Ni-supported catalysts [12]. Addressing this challenge and enhancing catalytic performance and stability involves a fundamental strategy: the modification of catalytic properties by introducing secondary elements and optimizing metal-support interactions. This approach enables the manipulation of catalytic active sites and the corresponding reaction routes. Among various metal oxide supports, CeO₂–ZrO₂–Al₂O₃ has been widely used for steam reforming because Al₂O₃ with a high specific surface area shows its high mechanical and thermal stability, while CeO₂–ZrO₂ has high oxygen mobility, which is crucial in steam reforming and decoking processes [13-16]. In this thesis, we prepared Ni-based catalysts with CeO₂, ZrO₂, and Al₂O₃ as the supports to investigate the metal-support interactions and the corresponding catalytic behavior in ESR.

1.2. Research objectives

The primary objective is to employ the Ni-Ce_xZr_{1-x}-Al₂O₃ catalyst in the ethanol steam reforming reaction, investigating the interaction between Ni-support and its influence on catalyst performance and coking behavior. Simultaneously, the aim is to enhance the reaction performance through catalyst modification.

The objectives are summarized as follows:

- i. Exploring Metal-Support Interactions over Ni/CeZrO₂-Al₂O₃ Catalysts for ESR:
 - a) The priority of the Ni-support interaction: Explore the impact of Ni loading contents on Ni/CeZrO_x-Al₂O₃ catalysts, focusing on selective Ni interactions with CeZrO_x-Al₂O₃. Investigate how these interactions influence Ni locations, inducing variations in hydrogen production and coke formation during ethanol steam reforming.
 - b) Optimizing active sites distribution by changing CZ/Al ratio: Investigate strategies to optimize active sites distribution over Ni/CeZr_xO₂-Al₂O₃ (CZA) catalysts by changing CZ/Al ratio. Evaluate the influence of metal-support interactions on the distribution of Ni nanoparticles and oxygen vacancies, aiming to minimize coke formation through efficient coke precursor gasification.
- ii. Enhancing Ethanol Steam Reforming Performance and Coke Gasification by Catalyst Synthesis Methods Optimization

Focus on different Ni contents and catalyst preparation methods (One-Pot vs. Successive Impregnation) over Ni/CeO₂-ZrO₂ (Ni/CZ) catalysts for ESR, analyzing their effects on Ni dispersion, oxygen vacancies, ethanol conversions, hydrogen production rates, and coke behaviors.

1.3. Outline of the dissertation

The structure of this dissertation contains four parts. The first part discussed the background and motivation of the research, the objectives will be introduced in this part as well. The second part mainly discussed about Objective 1, including Chapter 2 and Chapter 3.

The third part (Chapter 4) discussed the Objective 2. Finally, the summary and recommendation for future work will be explained in Part 4. **Fig. 1.1** demonstrates the structure of the thesis.

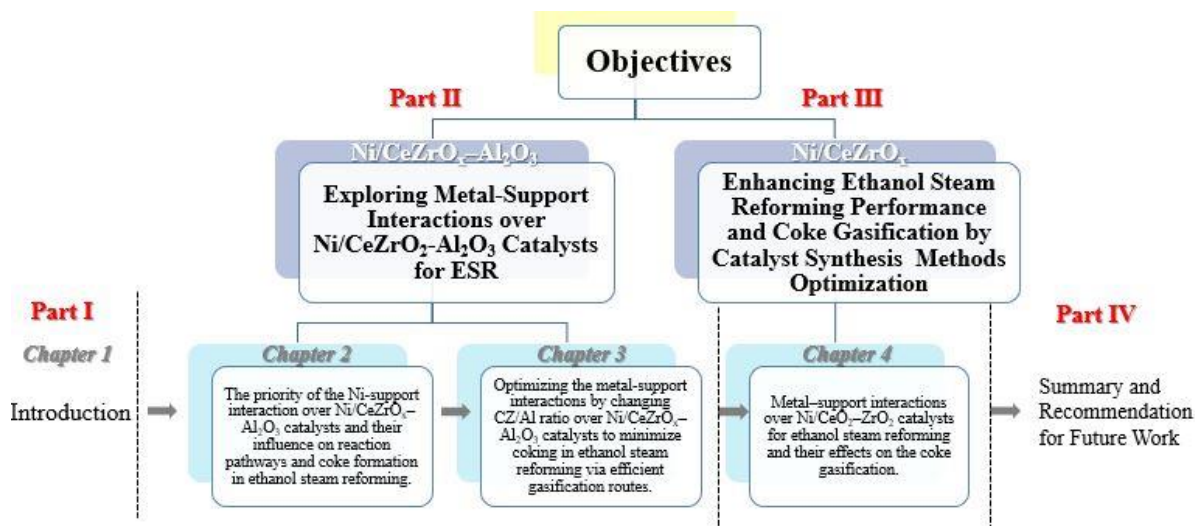


Fig. 1.1. The structure of the thesis corresponding to the objectives

PART II – EXPLORING METAL-SUPPORT INTERACTIONS IN Ni/CeZrO_x-Al₂O₃ CATALYSTS FOR ETHANOL STEAM REFORMING: IMPACTS ON REACTION PATHWAYS AND COKING BEHAVIOR

Chapter 2. The priority of the Ni-support interaction over Ni/CeZrO_x-Al₂O₃ catalysts and their influence on reaction pathways and coke formation in ethanol steam reforming

2.1. Introduction

In this work, Ni/CeZrO_x-Al₂O₃ is chosen as the catalyst system to investigate the optimal Ni-support interaction for preventing coke deactivation; thus, increasing the reforming ability of Ni-based catalysts for ESR. In the Ni/CeZrO_x-Al₂O₃ catalyst system, three active sites are involved in ESR: Ni sites, oxygen vacancies in the CeZrO_x support, and acidic sites on Al₂O₃. The key issues for studying the Ni-support interactions are how they modify different types of active sites and the active site modification influences which reaction pathways in ESR. However, previous literature on the interactions between Ni and various components of the support and their influences on the ESR performance and the reaction pathways are limited because the catalyst has multiple components in the support and ESR is a complex reaction accompanied by numerous side reactions. In contrast to Ni-Al₂O₃ interactions, previous studies on the Ni-support interactions have mainly focused on the Ni-CeO₂ interactions, describing the structural and electronic properties modification of the Ni and oxygen vacancies in CeO₂ [17, 18]. In terms of catalyst deactivation through coking at moderate

temperatures, the coking pathways include the Boudouard reaction route and the polymerization of ethylene from ethanol dehydration on surface acidic sites [19]. The latter reaction route is closely associated with the Al_2O_3 acidity. Therefore, the Ni– Al_2O_3 interactions in the Ni/CeZrO_x– Al_2O_3 catalyst and their role in the coking behavior of ESR must be discussed.

Based on the aforementioned discussion, we prepared Ni/CeZrO_x– Al_2O_3 containing fixed amounts of CeZrO_x and Al_2O_3 and different loading amounts of Ni to investigate the interactions between Ni and each component in the support. Diverse characterization tools were employed to measure the properties related to the active sites in the catalysts. Furthermore, the ESR tests for all the prepared catalysts were conducted at 550 °C to evaluate the catalytic performance, including the reforming ability and coking behavior with a combination of the spent catalyst characterizations. Interestingly, in this study, it has been found that depending on the Ni loading contents, Ni selectively interacts with each support component. At a low Ni loading amount, Ni active sites are mainly located on CeZrO_x by the preferential interaction between Ni and CeZrO_x. In contrast, for the high Ni loading amount, the excessive Ni active sites are mainly deposited on Al_2O_3 . These excessive Ni active sites near the acidic sites on Al_2O_3 accelerate coke formation via the ethylene precursor, whereas the Ni active sites on CeZrO_x enhance the reforming ability through a combination with the steam activation on the oxygen vacancies.

2.2. Experimental

2.2.1. Catalyst preparation

The $\text{CeZrO}_2\text{-Al}_2\text{O}_3$ support employed herein was synthesized by impregnating mesoporous Al_2O_3 with an aqueous solution of Ce and Zr precursors. $\text{Ce}(\text{NO}_3)_3 \cdot 6\text{H}_2\text{O}$ (99%; Sigma-Aldrich, Korea) and $\text{ZrO}(\text{NO}_3)_2 \cdot x\text{H}_2\text{O}$ (99%; Sigma-Aldrich, Gyeonggi, South Korea) were used as the precursors. First, mesoporous Al_2O_3 was prepared through a hydrothermal method using $\text{Al}(\text{NO}_3)_3 \cdot 9\text{H}_2\text{O}$ (JUNSEI, Tokyo, Japan) as a precursor. For this, 24 g of $\text{Al}(\text{NO}_3)_3 \cdot 9\text{H}_2\text{O}$ was completely dissolved in 35-mL deionized water using a magnetic stirrer. Subsequently, 2.6 g of triblock copolymer Pluronic P123 (PEG-PPG-PEG; Sigma-Aldrich, Korea) was dissolved into 75-mL ethanol and then mixed with Al salt solution to obtain a porous structure. Next, 13.5 g of urea was dissolved in the mixed solution as a precipitator. The solution was then transferred into a 200-mL Teflon-lined stainless-steel autoclave, which was placed in an oven at 80 °C for 5 h and 120 °C for 12 h. After cooling to room temperature, the resulting product was filtered and washed with deionized water to acquire the precipitates, which were subsequently dried at 70 °C for 24 h in an oven. As the final step to obtain mesoporous Al_2O_3 , the dried precipitates were calcined in air at 600 °C for 6 h. The salt of the solution containing 1:1 of $\text{Ce}(\text{NO}_3)_3 \cdot 6\text{H}_2\text{O}$ and $\text{ZrO}(\text{NO}_3)_2 \cdot x\text{H}_2\text{O}$ was impregnated into Al_2O_3 using the incipient wetness impregnation method to attain 20 wt.% CeZrO_2 in the support. The obtained paste samples were dried at 70 °C for 12 h in an oven. After drying, the solid samples were calcined in a furnace at 600 °C for 6 h to remove any impurities. The obtained $\text{CeZrO}_2\text{-Al}_2\text{O}_3$ catalyst is designated herein as CZ-Al.

The Ni/CeZrO₂-Al₂O₃ catalysts were prepared through the incipient wetness impregnation method using an aqueous solution of Ni(NO₃)₂·6H₂O (Sigma-Aldrich, Gyeonggi, South Korea). The amount of Ni in the solution was calculated to be 5, 10, 15, and 20 wt.% on each support. After the impregnation, the samples were dried at room temperature for 24 h and at 100 °C for 12 h in an oven, followed by calcination at 600 °C for 6 h in a furnace. The atomic ratio of Ce to Zr in all catalysts was 1:1. The Ni-containing catalysts were reduced in H₂ at 600 °C for 2 h before characterizing the prepared catalysts (except the H₂-TPR experiments). The Ni-containing catalysts are designated as xNi/CZ-Al, where x denotes the wt.% of Ni in the catalysts.

2.2.2. Catalyst characterization

The Brunauer–Emmett–Teller (BET) surface area of the catalysts was determined using nitrogen adsorption/desorption curves recorded on an ASAP 2020 apparatus (Micromeritics, Norcross, GA, USA) at -196 °C. Before the analysis, the samples were degassed for 24 h at 200 °C in vacuum. The acidic sites were counted based on the temperature-programmed desorption of NH₃ (TPD-NH₃) on a MicrotracBEL BELCAT-M instrument (MicrotracBEL Corp., Osaka, Japan). The TPD-NH₃ results were recorded for the temperature range 50 °C–900 °C by a thermal conductivity detector (TCD) detector. A hydrogen temperature-programmed reduction (H₂-TPR) was performed in a multipurpose analytical system (BELCAT-M, MicrotracBEL Corp., Osaka, Japan) using a TCD. Nitrogen and mixture gases (5% H₂ in N₂) were used as the carrier and reducing gases, respectively. The ramp rate was

set to 2 °C/min from 50 °C to 900 °C. Hydrogen temperature-programmed desorption (H₂-TPD) experiments were conducted in a quartz flow reactor installed on the same system (BELCAT-M, MicrotracBEL Corp., Osaka, Japan). Before the adsorption measurements, the samples were reduced in-situ under He (with 5% H₂) at 600 °C. After cooling the samples to 50 °C, 5-vol% H₂/N₂ (70 mL/min) was then pulsed on the catalyst until no further H₂ was consumed. The desorption was programmed at 1.5 °C/min from 50 °C to 900 °C in flowing N₂.

The X-ray diffraction (XRD) patterns for the fresh and spent catalysts were obtained using a Rigaku RAD-3C diffractometer (Rigaku Corp., Tokyo, Japan) with Cu K_{α1} radiation ($\lambda = 1.5418 \text{ \AA}$) at a scattering angle (2θ) scan rate of 2°/min, operating at 35 kV and 20 mA. The Scherrer equation was used to calculate the crystallite sizes. High-resolution transmission electron microscopy (HR-TEM) images were obtained using a JEOL JEM-2100F instrument (JEOL Ltd., Tokyo, Japan) to investigate the morphologies of the fresh and spent catalysts. The Raman spectra were obtained with a DXR Raman microscope (Thermo Fisher Scientific, Waltham, MA, USA) using a 532-nm excitation source.

The X-ray photoelectron spectroscopy (XPS) data were obtained using the Thermo K-Alpha XPS with an aluminum K α X-ray source (Thermo Fisher Scientific, Waltham, MA, USA). The samples were collected using an X-ray spot size of 400 μm , pass energy of 80 eV, and an energy step size of 0.1 eV. The charging effects were corrected by adjusting the binding energy of the C 1s peak from carbon contamination to 284.8 eV. The thermogravimetric analysis (TGA) of the spent catalysts was performed using a TGA Q50

apparatus (TA Instruments, New Castle, DE, USA). The experiments were performed in a flow of air (40 mL/min) and N₂ (60 mL/min) at a heating rate of 10 °C/min and a final temperature of 900 °C. The amount of carbon deposition was calculated based on the mass loss profiles in the TGA test.

2.2.3. Ethanol steam reforming reaction test

ESR was performed in a continuous flow fixed-bed quartz reactor under atmospheric pressure. Accordingly, 0.2 g of catalysts was mixed with glass wool and placed in the middle of a quartz tube. Pure He (30 mL/min) was used as the carrier gas. The system was purged before the reduction step. All the calcined catalysts were in-situ reduced in the flow of H₂ (6 mL/min) and He (30 mL/min) at 600 °C for 2 h before the reaction test. Water and ethanol were mixed in a fixed molar ratio of 6 (H₂O/C₂H₅OH = 6). Then, the liquid mixture, as the reactant, was continuously injected into the reactor using a high-performance liquid chromatography pump (PCS Pump SP-22-12S, FLOM/JAPAN, 0.01–2.00 mL/min, Tokyo). He was also supplied at 70 mL/min into the reactor to serve as a carrier gas during the reaction. The gas hourly space velocity (GHSV) was set to 10,619 h⁻¹ for all the reaction tests. The inlet lines of the reactor were heated with a heating belt for sufficient reactant vaporization. Before the gas-phase product analysis, the condensable vapors were trapped using a dry-ice condenser. During the reaction test, the gas products were injected into a chromatographer (Acme 6000 GC, YL Instrument Co., Ltd., Dongan-gu, South Korea) every 30 min using an on-line auto-injection system and analyzed by a TCD detector connected

with a Carboxen column. The liquid products collected with a condenser were analyzed by a chromatograph with a DB-WAX column and a flame ionization detector. **Fig. 2.1** depicts a schematic of the ESR testing system. The ethanol conversion, hydrogen selectivity and production rate, and C-containing product selectivity were calculated as follows:

$$\text{Ethanol conversion (\%)} = \frac{nEtOH_{in} - nEtOH_{out}}{nEtOH_{in}} \times 100,$$

$$\text{H}_2 \text{ selectivity (\%)} = \frac{nH_2}{nH_2 + 2nCH_4 + 2nC_2H_4 + 3nC_2H_6},$$

$$\text{H}_2 \text{ production rate } (\mu\text{mol}/(\text{g}_{\text{cat.}} \cdot \text{min})) = \frac{nH_2 \text{ per min.}}{\text{mass of catalysts}},$$

$$\text{C - containing product selectivity} = \frac{j \times n_i}{\sum j \times n_i},$$

where n_i denotes the moles of product i , and j represents the number of carbon atoms in the C-containing product.

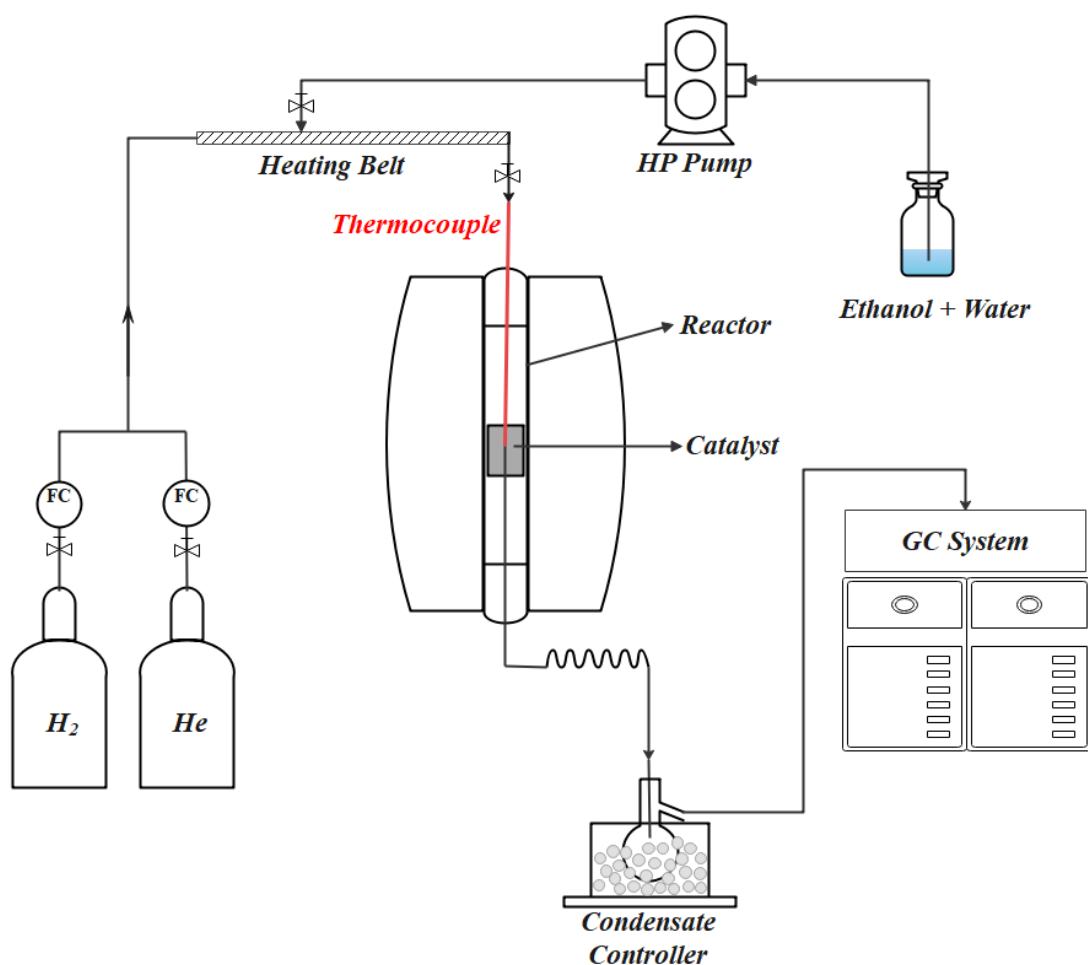


Figure 2.1. Schematic setup of the fixed-bed flow reaction system for ethanol steam reforming.

2.3. Results and discussion

2.3.1. Selective Ni–support interactions at different Ni loading contents

Table 2.1 lists the physicochemical properties of the prepared catalysts. All the catalysts exhibited a Type IV isotherm with the characteristic hysteresis loop, indicating the presence of a mesoporous structure (**Fig. 2.2A**). Interestingly, the pore sizes did not decrease after Ni addition, whereas Ni deposition onto the CZ-Al support significantly decreased the BET surface areas of the Ni-containing catalysts (**Table 2.1** and **Fig. 2.2B**).

Table 2.1. Physicochemical properties of the xNi/CZ-Al catalysts.

Sample	BET Surface area (m ² /g)	Pore size (nm)	Pore volume (cm ³ /g)	I _{CZ} /I _{Al} ^a	CZ size (nm) ^b	Ni size (nm) ^{b, c}	H ₂ consumption (mmol/g) ^d	Ni size of spent samples (nm) ^b	I _{G/D} ^e
CZ-Al	190.3	4.32	0.33	4.8	10.6	n.a.	0.61	n.a.	1.68
5Ni/CZ-Al	152.5	4.90	0.29	3.1	10.4	2.4/1.1	0.77	3.1	1.38
10Ni/CZ-Al	137.7	4.90	0.26	2.5	10.1	5.6/2.9	1.07	5.2	1.08
15Ni/CZ-Al	131.5	4.90	0.24	2.1	10.9	9.4/4.1	1.52	9.3	1.00
20Ni/CZ-Al	129.5	5.64	0.22	2.4	11.0	8.9/3.6	1.68	10.0	0.94

(a) The peak intensity ratio of CZ (111) phase to the Al₂O₃ (441) phase in XRD (a.u.)

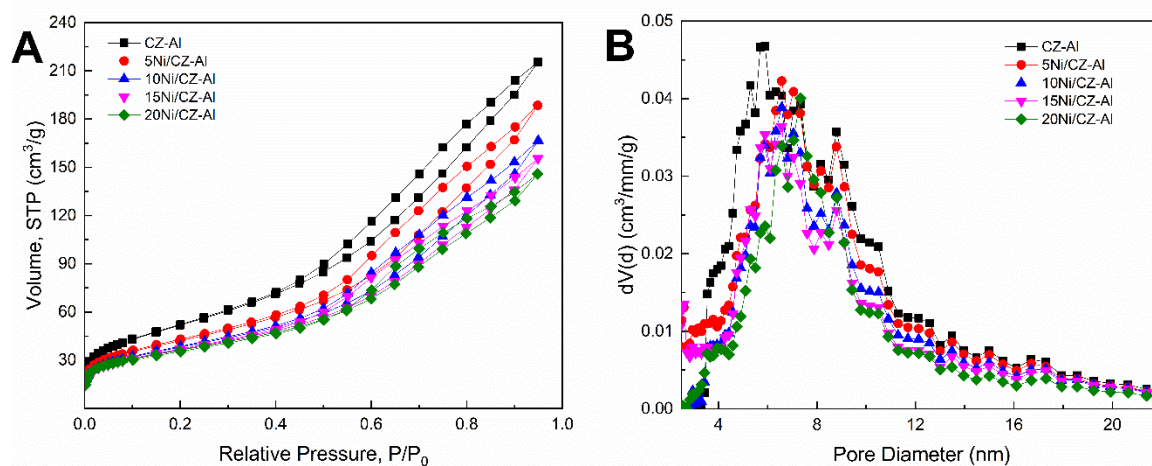
(b) The values were obtained by the application of the Scherrer equation for the characteristic XRD peaks of each crystallite.

(c) The values were obtained from the FFT calculation in the TEM images.

(d) The values were obtained from H₂-TPR.

(e) The values were obtained by calculating the ratio of the peak intensity in the spent catalysts of Raman: I_{G/D} = Intensity (G band)/Intensity (D band).

These results indicate that the Ni addition into the support is not a simple physical impregnation process; however, it is a chemical interaction, as a certain phase is formed and porous structure is changed.

**Figure 2.2.** (A) N₂ adsorption–desorption isotherms and (B) pore size distribution of the xNi/CZ-Al catalysts.

The NH₃-TPD experiments were performed on the xNi/CZ-Al catalysts. **Table 2.2** and **Fig. 2.3** present the results.

Table 2.2. Acidic sites, Ni metallic site, and relative intensity ratio of the peaks ($I_{\text{Ce-V/Ce-O}}$) related to the oxygen vacancy of the catalysts.

Catalyst	Acidic site (mmol _{NH₃} /g _{cat}) ^a	Ni metallic site (mmol _{H₂} /g _{cat}) ^b	$I_{\text{Ce-V/Ce-O}}$ ^c
CZ-Al	0.389	n.a.	0.14
5Ni/CZ-Al	0.334	0.363	0.19
10Ni/CZ-Al	0.297	0.336	0.90
15Ni/CZ-Al	0.292	0.386	0.68
20Ni/CZ-Al	0.309	0.595	0.99

(a) The values were obtained from NH₃-TPD.

(b) The values were estimated based on the H₂-TPD measurement.

(c) The values were obtained by calculating the ratio of the peak intensity in the fresh catalysts of

Raman: $I_{\text{Ce-V/Ce-O}} = \text{Intensity (Ce-V)} / \text{Intensity (Ce-O)}$.

All the catalysts showed two main desorption peaks at approximately 250 °C and 750 °C, which corresponded to the desorption of ammonia adsorbed weakly and strongly on the acidic sites of the catalysts, respectively. The total acidic sites significantly reduced from 0.389 for CZ-Al to 0.334 and 0.297 for 5Ni/CZ-Al and 10Ni/CZ-Al, respectively, when the Ni species was initially impregnated. This result implies that the initial Ni loading reduced the Al₂O₃ support acidity due to the formation of NiAl₂O₄ [20, 21]. However, regardless of increasing the Ni loading amount, the total acidic sites remained the same after 10% Ni

loading, which is consistent with the trend in the BET surface area (**Table 2.1**). In other words, the NiAl_2O_4 formation in the catalysts initially occurred at the stage of low Ni loading (5% and 10%) due to the limited chemical interaction between Ni and Al_2O_3 .

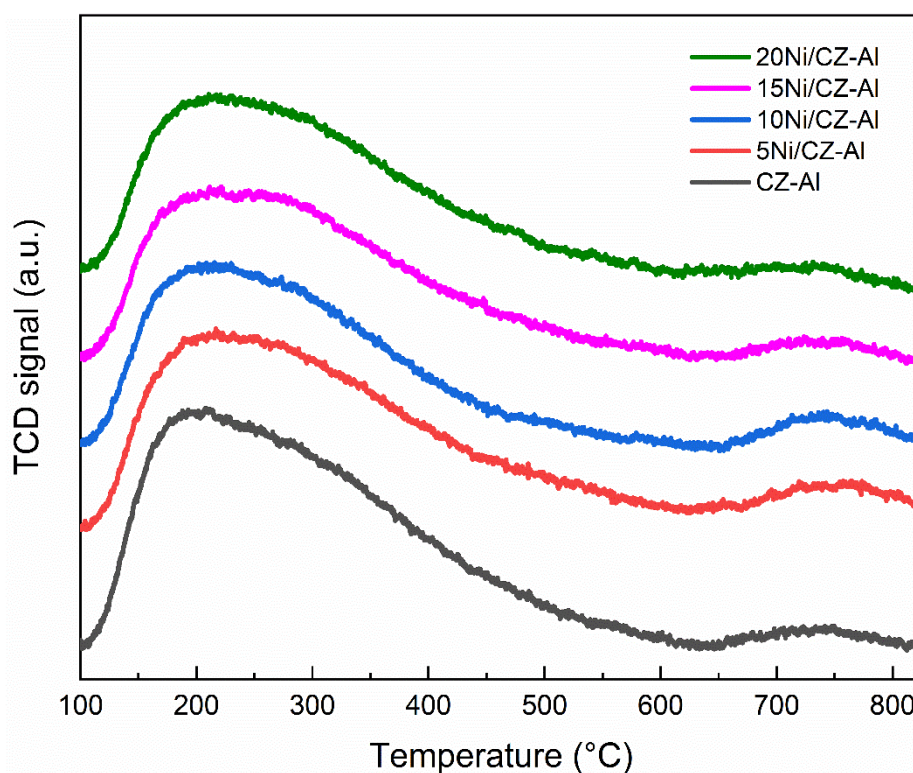


Figure 2.3. NH_3 -TPD profiles of the $x\text{Ni}/\text{CZ-Al}$ catalysts.

The XRD analysis was employed to investigate the crystalline phases of the catalysts. In **Fig. 2.4A**, all catalysts exhibited the characteristic peaks of the $\gamma\text{-Al}_2\text{O}_3$ phase at 37.4° and 67.3° of 2θ (JCPDS#04-0880). For the $\text{Ce}_x\text{Zr}_{1-x}\text{O}_2$ (CZ) solid solution phase, the characteristic XRD peaks appeared at 28.7° , 33.5° , 48.1° , 57.0° , and 77.7° of 2θ for (111), (200), (220), (311), and (331) planes, respectively (JCPDS#28-0271), suggesting a strong crystalline structure. However, as the Ni loading amounts increased, the peak intensities for the CZ (111) phase at $2\theta = 28.7^\circ$ were decreased relatively from 4.8 of $I_{\text{CZ}}/I_{\text{Al}}$ (height ratio of the peaks at 28.7° and 67.3°) to 2.1 (**Table 2.1**), implying the decreasing CZ crystallinity due

to Ni loading. In particular, the I_{CZ}/I_{Al} values dropped for the 10, 15, and 20Ni/CZ-Al catalysts. The decrease in the CZ crystallinity was associated with the Ni–CZ interaction generating more defects, such as oxygen vacancies, in the CeO₂ structure [22].

The typical characteristic XRD peaks for the Ni (111) phase appearing at 44.5° of 2θ (JCPDS#04-0850) intensified with increasing Ni loading amount. The average Ni and CZ crystallite sizes were roughly estimated using the Scherrer equation. From the characteristic peak at 28.7° for the CZ crystallite, the calculated CZ sizes were almost constant in the range of 10.0–11.0 nm (**Table 2.1**), demonstrating that the Ni–CZ interaction did not affect the CZ crystallite size. In contrast, the Ni crystallite sizes calculated on the basis of the Ni (111) phase increased from 2.4 nm for 5Ni/CZ-Al to 5.6, 9.4, and 8.9 nm for 10, 15, and 20Ni/CZ-Al, respectively, implying an agglomeration of Ni nanoparticles at the high Ni loading amount of 10, 15, and 20 wt.%.

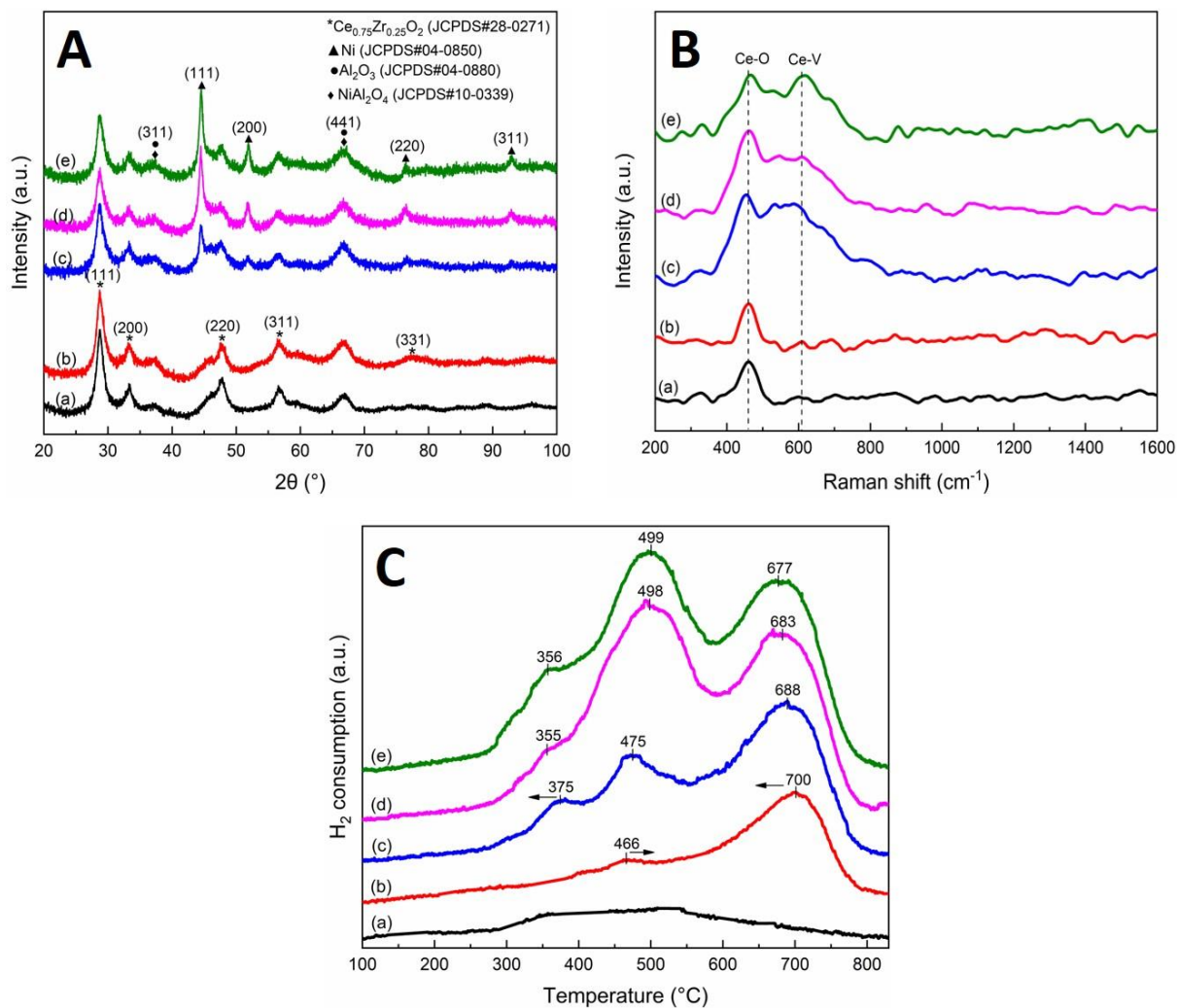


Figure 2.4. (A) XRD patterns, (B) Raman spectra, and (C) H₂-TPR profiles of the reduced xNi/CZ-Al catalysts: (a) CZ-Al, (b) 5Ni/CZ-Al, (c) 10Ni/CZ-Al, (d) 15Ni/CZ-Al, and (e) 20Ni/CZ-Al.

The HR-TEM images of the catalysts were obtained to measure the Ni particle sizes. In **Fig. 2.5**, the Ni nanoparticles revealed a spherical shape. Their size distributions over supports are shown in the insets of each image. The average Ni sizes estimated from the HR-TEM images for xNi/CZ-Al ranged from 1.1 to 4.1 nm (**Table 2.1**). The high Ni loading of 10, 15, and 20 wt.% increased the Ni size, which is consistent with the trend estimated from

the XRD measurements. The XRD and HR-TEM data showed that the 10, 15, and 20Ni/CZ-Al catalysts had similar average Ni sizes, suggesting that Ni active sites might have proportionally increased with increasing Ni loading contents.

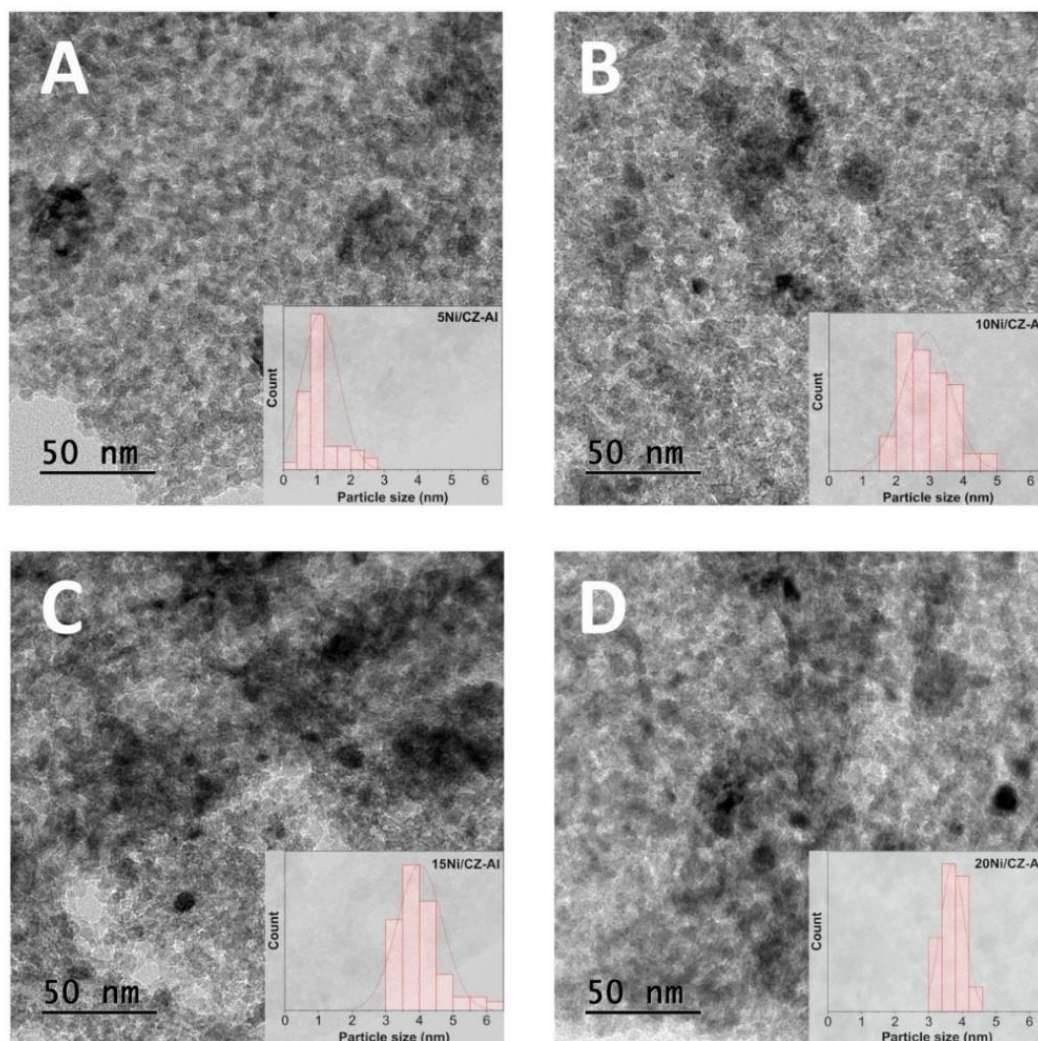


Figure 2.5. HR-TEM images of the reduced xNi/CZ-Al catalysts.

The H₂-TPD measurements can provide information on the Ni active sites of the catalysts. In **Fig. 2.6**, all the catalysts showed only one broad H₂ desorption peak between 200 °C and 800 °C, corresponding to the desorption of H₂ adsorbed on the Ni nanoparticles dispersed over diverse supports [23]. The Ni sites for the Ni-containing catalysts were

calculated based on the desorption amounts (**Table 2.2**). Interestingly, the amount of Ni sites for 5Ni/CZ-Al was higher than that of 10Ni/CZ-Al in spite of a half Ni loading amount. The amount of Ni sites for 15 and 20Ni/CZ-Al catalysts gradually increased with Ni loading amount compared with that of 10Ni/CZ-Al. The observed behavior is in good agreement with the XRD and HR-TEM data for the Ni dispersion. The dispersion of Ni for 5Ni/CZ-Al was much higher than that for 10Ni/CZ-Al, resulting in the higher number of Ni surface sites. In contrast, the Ni dispersions of 10, 15, and 20Ni/CZ-Al were similar; thus, the Ni sites for the three catalysts proportionally increased with the Ni loading amount, as aforementioned.

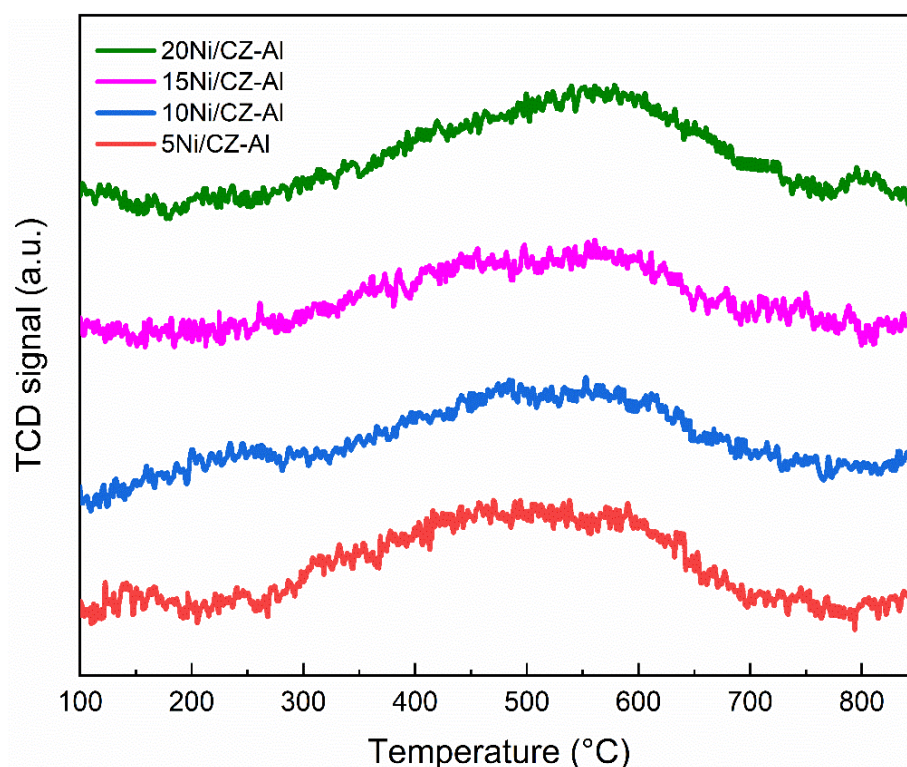


Figure 2.6. H₂-TPD profiles of the xNi/CZ-Al catalysts.

Raman spectra were used to confirm the existence of oxygen vacancies due to their great sensitivity to the Ce–O bond vibration and lattice defects [24] (**Fig. 2.4B**). For the CZ-Al support, a sharp peak at 465 cm⁻¹ can be assigned to the F_{2g} fluorite structure vibration. A

broad peak at 600 cm^{-1} was additionally detected after adding Ni, which corresponds to the defect band related to the oxygen vacancies in the ceria lattice (Ce–V) [25]. **Table 2.2** summarizes the relative intensity ratios of the peaks ($I_{\text{Ce-V/Ce-O}}$) for all the catalysts. Compared with that of the bare support, the $I_{\text{Ce-V/Ce-O}}$ ratios dramatically increased after 10 wt.% of Ni loading. This result confirmed that the oxygen vacancies in the CZ lattice were efficiently formed by the strong Ni–CZ interactions after 10 wt.% Ni loading. However, similar values for 10, 15, and 20Ni/CZ-Al imply that the Ni–CZ interaction saturated above 10 wt.% Ni loading.

The H₂-TPR experiments were performed to investigate the reduction behavior of the catalysts. In all samples, the hydrogen consumption increased with increasing Ni content from 0.61 mmol/g (CZ-Al) to 1.68 mmol/g (20Ni/CZ-Al) due to the increasing absolute Ni content (**Table 2.1**). **Fig. 2.4C** showed three main reduction peaks for the xNi/CZ-Al catalysts appearing around 375 °C, 475 °C, and 688 °C. The shoulder peak at the lowest temperature (355 °C–375 °C) could be assigned to the reduction peak of the isolated NiO [26]. Another peak around 677 °C–700 °C could be ascribed to the NiAl₂O₄ reduction [27]. The middle peak (466 °C–499 °C) was overlapped by the reduction peaks of NiO, which interacted with CZ and Al₂O₃ [28]. NiO over the CZ support can be reduced at a lower temperature than that over the Al₂O₃ support [29-31]. Interestingly, when the Ni loading amounts in the supports increased, the first and last reduction peaks shifted to a low temperature, indicating that the Ni addition improved the catalyst's reduction ability. In contrast, the overlapped peak in the middle range shifted from 466 °C to a higher temperature,

and its intensity was high for 15 and 20Ni/CZ-Al. This behavior can be associated with the selective interaction of Ni with CZ or Al₂O₃ along with the Ni contents. At the lowest Ni content (5Ni/CZ-Al), the added Ni species favored the NiAl₂O₄ formation, which was hardly reducible. When the Ni content was increased to 10 wt.% (10Ni/CZ-Al), the Ni species remaining after the formation of NiAl₂O₄ preferentially came into contact with the CZ solid solution, producing more oxygen vacancies in the CZ lattice. In **Fig. 2.4C**, the peaks at 375 °C and 475 °C are apparent; these peaks were related to the reduction steps of the isolated NiO and NiO interacting with the CZ phase. After the saturation of the Ni species selectively interacting with the CZ lattice, the over-saturated Ni species in 15 and 20Ni/CZ-Al were finally located on Al₂O₃, as evidenced by the dominance and shift of the middle range reduction peak (**Figs. 2.4C(d) and (e)**). The peak shifted to 499 °C, and its strong intensity indicated that the amount of the Ni species on Al₂O₃ selectively increased with the Ni loading content because Al₂O₃ reduces at a higher temperature than CeO₂ [32]. In conclusion, the H₂-TPR profiles showed that along with the added Ni contents, the Ni species tended to selectively interact with the support, and the formation of Ni phases on the supports follows the order of NiAl₂O₄, NiO on the CZ with the oxygen vacancy generation, and NiO on Al₂O₃. The NiAl₂O₄ formation at the initial Ni loading step can be attributed to the drop in the acidic sites for 5 and 10Ni/CZ-Al (**Table 2.2**). In addition, the trend in the oxygen vacancies from the Raman spectra is also in good agreement with the Ni-CZ interactions. The intensity ratios of the oxygen vacancies and Ce-O in the CZ lattice for 10, 15, and 20Ni/CZ-Al catalysts were much higher than CZ-Al and 5Ni/CZ-Al (**Table 2.2**).

Fig. 2.7 shows the XPS data of Ni 2p, O 1s, and Al 2p. The Ni 2p spectra exhibited the characteristic peaks of NiO at 854.3 and 856.6 eV, which were attributed to the Ni interacting with the supports (Ni-S) and NiAl₂O₄ (NiA), respectively, with two satellite peaks at 860.7 and 863.6 eV [33-35]. The proportions of the intensity for the Ni-S peak gradually increased as the Ni loading amounts increased (**Fig. 2.7D**), indicating that the NiAl₂O₄ formation at the initial Ni loading step weakened with increasing Ni contents.

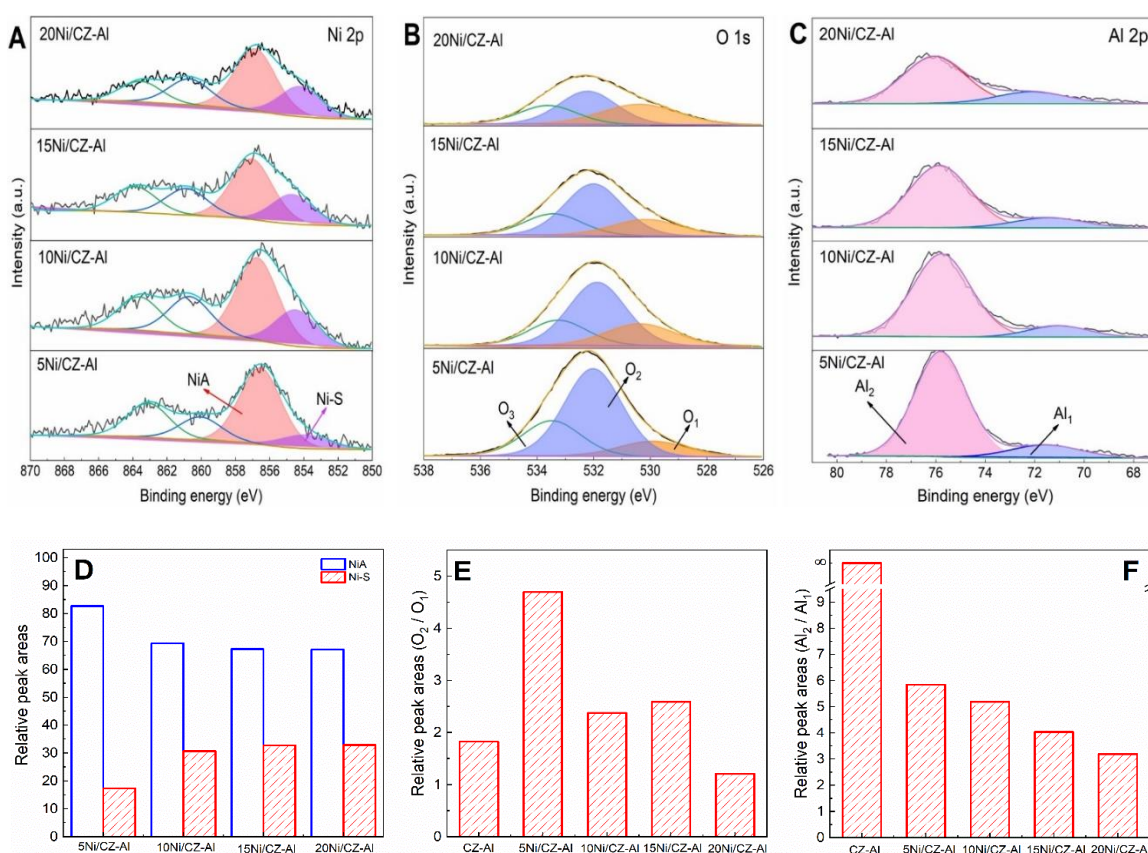


Figure 2.7. XPS data of (A) Ni 2p, (B) O 1s, and (C) Al 2p of the fresh catalysts, and relative peak areas of (D) NiA and Ni-S, (E) O₁ and O₂, and (F) Al₁ and Al₂ in each XPS.

To explain the Ni species locations on the supports along with the Ni contents, the XPS data of O 1s and Al 2p are shown in **Figs. 2.7B and 2.7C**. The O 1s spectra can be deconvoluted into three peaks (i.e., 530.1 (O₁), 532.3 (O₂), and 533.6 eV (O₃)) corresponding to the lattice oxygen in the CeZrO_x solid solution (O₁), the lattice oxygen in Al₂O₃ (O₂), and

the surface hydroxyl group (OH) in the catalysts (O_3) [25, 34, 36, 37]. We calculated the intensity ratios between O_1 and O_2 in the Ni-containing catalysts. **Fig. 2.7E** presents the results. The intensity ratios gradually decreased with the Ni contents, implying that the lattice oxygen amounts in Al_2O_3 at high Ni contents relatively decreased compared with those in CZ. This trend was due to the different coverage of the Ni species over the supports caused by the selective Ni interaction with different support types. The initial O_2/O_1 peak ratio for CZ-Al was 1.8, representing a relative ratio of Al_2O_3 to CZ on the CZ-Al surface (**Fig. 2.8A**). The value for 5Ni/CZ-Al increased to 4.7, indicating that the relative amount of Al_2O_3 to CZ over 5Ni/CZ-Al was increased by a factor of 2.6. In other words, the preferential Ni-CZ interaction induced the selective coverage of the added Ni species on the CZ support, resulting in decreasing O_1 intensity over 5Ni/CZ-Al. This decrease in the values for 10, 15, and 20Ni/CZ-Al was ascribed to the additional location of the excessive Ni species over Al_2O_3 because the coverage of the excessive Ni species on Al_2O_3 prevented the lattice oxygen (O_2) in Al_2O_3 from being detected. The same trend was observed in the XPS data of Al 2p. The Al 2p spectrum can be resolved into two peaks at 72.2 and 75.8 eV (**Fig. 2.7C**). The former (Al_1) is assigned to $NiAl_2O_4$ in the Ni 3p region [38], whereas the latter (Al_2) corresponds to Al_2O_3 [39]. Compared with the Al 2p spectrum of the bare support CZ-Al (**Fig. 2.8B**), the peak intensity ratio of Al_2 to Al_1 for 5Ni/CZ-Al suddenly decreased from ∞ to 5.8 due to the $NiAl_2O_4$ formation. The ratios for the Ni-containing catalysts then gradually decreased due to the selective coverage of the Ni species on Al_2O_3 (**Fig. 2.7F**). That is, the excessive Ni species at the high Ni content finally covered the Al_2O_3 surface after the

saturation of the prior Ni–CZ interaction. These findings in the XPS data indirectly revealed the selective Ni–support interactions over the xNi/CZ-Al catalysts. The formation of the NiAl₂O₄ phase and the prior Ni–CZ interaction occurred at the low-Ni-containing catalysts. On the contrary, at the high Ni loading amounts, the excessive Ni species were mainly located on the Al₂O₃ surface, reflecting the gradual decrease in the Al₂O₃ intensity caused by the surface Al₂O₃ coverage by the over-saturated Ni species.

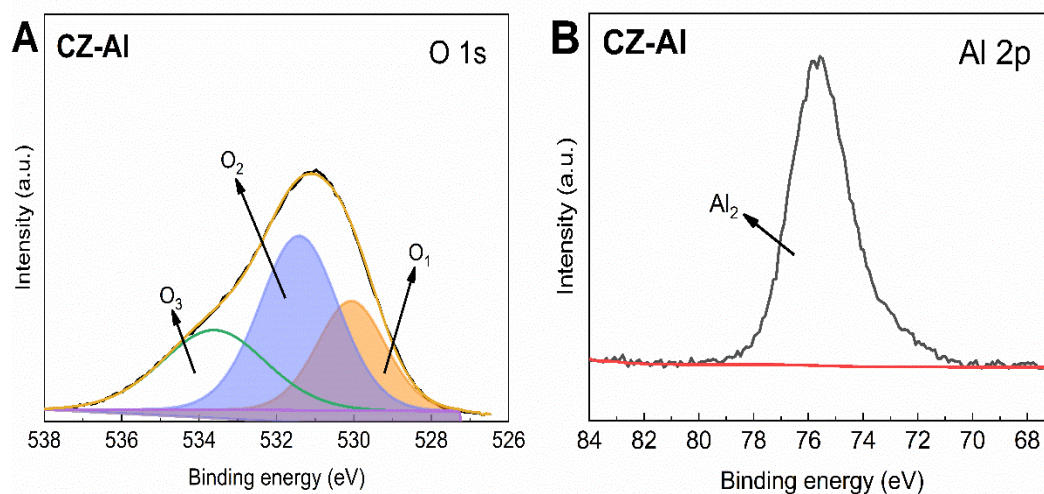
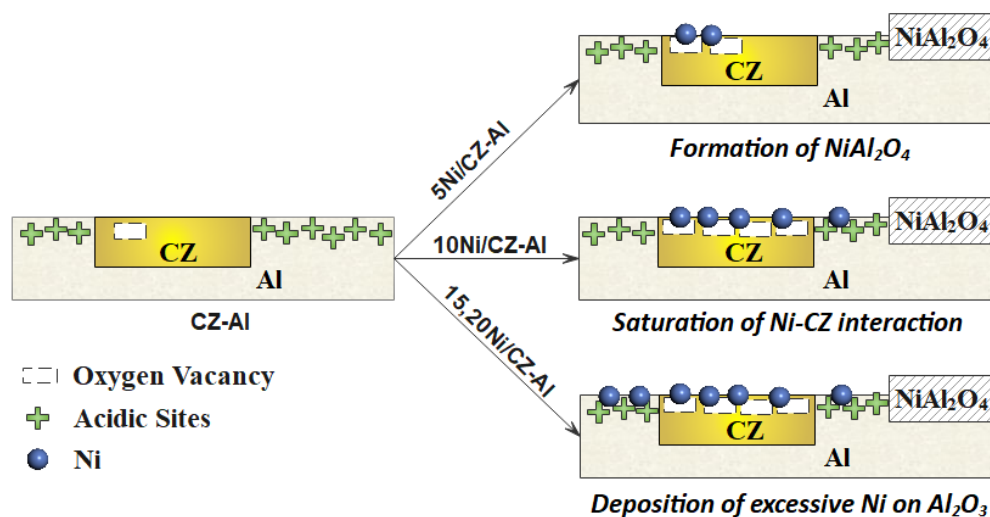


Figure 2.8. X-ray photoelectron spectroscopy (XPS) spectra of (A) O 1s and (B) Al 2p of the fresh catalysts.

Based on the diverse characterization data for the catalysts, we propose herein a schematic illustration of not only the selective interactions of the Ni species with the supports along with the Ni contents, but also the corresponding change in the three types of active sites (i.e., Ni metal, oxygen vacancy over CZ, and acidic sites over Al₂O₃) (**Scheme 2.1**). At the low Ni loading amount (5Ni/CZ-Al), the initial Ni species preferentially formed the NiAl₂O₄ phase, an inactive site for ESR, which subsequently resulted in a decrease of the catalyst

acidity. For 5Ni/CZ-Al, a part of the added Ni species selectively interacted with the CZ support and existed in the Ni metallic phase near the oxygen vacant sites in the CZ lattice. When the Ni content was increased up to 10 wt.% (10Ni/CZ-Al), the main interaction between Ni and the support was preferentially shifted to the CZ support to form Ni metal particles with more oxygen vacancies in the CZ lattice (saturated Ni interaction with CZ). For 10Ni/CZ-Al, a part of the added Ni species was located on the Al₂O₃ support as over-saturated Ni particles because of the saturation of the Ni–CZ interaction. The selective Ni–CZ interaction would be saturated below 10 wt.% of Ni with the full generation of the oxygen vacancy in the CZ lattice. In consensus, the presence of more oxygen vacancies in the CZ lattice is beneficial to the ESR process because it allows more steam to be activated on the catalyst surface, enhancing steam reforming and the water–gas shift reaction [40]. For 15Ni/CZ-Al and 20Ni/CZ-Al, the portions of the over-saturated Ni species located near the acidic sites over Al₂O₃ after the saturation of the selective Ni–CZ interaction increasingly became higher and covered the Al₂O₃ surface more and more without changing the catalyst acidity. Over the Ni/CZ-Al catalysts, the Ni locations on the supports were responsible for the reaction pathways. The Ni metallic sites surrounded by the acidic sites could be one of the main reasons for the coke formation, while the Ni sites nearby the oxygen vacant sites enhanced the steam reforming ability of the catalysts. Therefore, considering the change in the three active sites over the Ni/CZ-Al catalysts caused by the selective Ni–support interactions along with the Ni content, the reaction pathways for ESR would be controllable. Furthermore, it would be feasible to find the optimal Ni–support interactions showing the

best catalytic performance in ESR.



Scheme 2.1. Schematic of the priority of the Ni-support interaction based on the Ni loading amounts.

2.3.2. Reaction results of ethanol steam reforming over the $x\text{Ni}/\text{CZ-Al}$ catalysts

The ESR reaction test was mainly conducted at 550 °C not only to evaluate the steam reforming ability, but also to track the coking behavior over the catalysts considering that steam reforming was mild, and the coke formation was accelerated at the reaction temperature. Even though the ESR test was also conducted at 750 °C for comparison, the coke amounts generated over the catalysts in the 750 °C reaction tests were much less than those generated at 550 °C due to the gasification or combustion of the coke precursors (**Fig. 2.9**), which was consistent with previously reported results [19, 41].

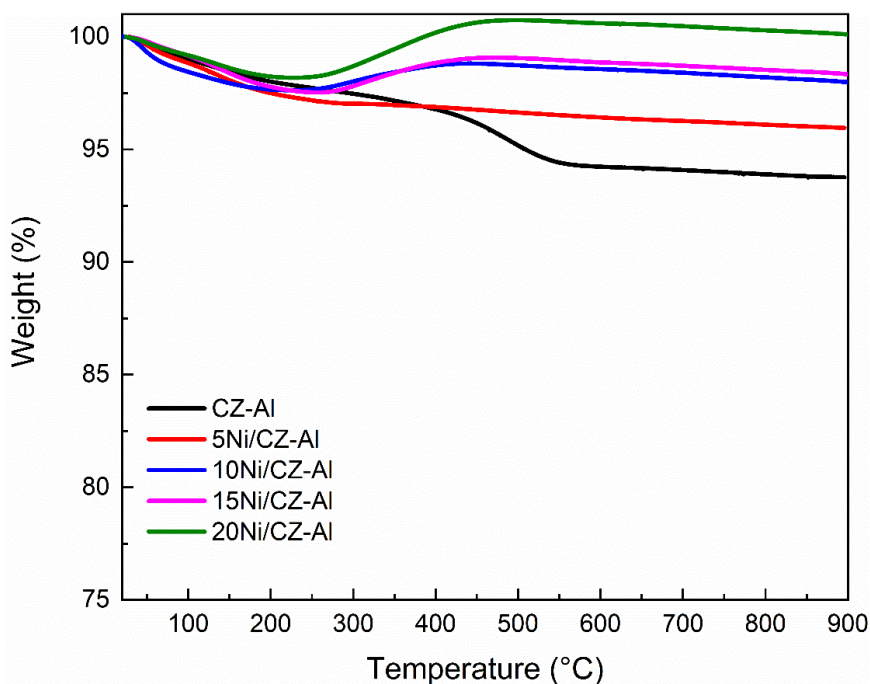


Figure 2.9. TGA profiles for the spent catalysts after 750 °C ESR reaction.

Hydrocarbon intermediates, such as methane, ethylene, and a trace of ethane, were detected with CO, CO₂, and H₂ in the gas phase during the reaction tests (**Table 2.3**).

Table 2.3. xNi/CZ-Al catalyst performance of the ESR reaction at 750 °C (reaction conditions: S/C = 3, GHSV = 10,619 h⁻¹).

Samples	C ₂ H ₅ OH conversion (%)	C-containing gas products selectivity (%)					H ₂ selectivity (%)	H ₂ production rate (μmol/g _{cat} .min)
		CO	CO ₂	CH ₄	C ₂ H ₄	C ₂ H ₆		
CZ-Al	100	27.2	7.5	30.8	32.4	2.1	30.8	774.1
5Ni/CZ-Al	100	42.8	27.4	25.9	2.5	1.4	57.50	1121.3
10Ni/CZ-Al	100	41.0	52.1	6.9	0	0	90.43	1900.9
15Ni/CZ-Al	100	45.1	46.0	8.9	0	0	86.80	1505.8
20Ni/CZ-Al	100	44.1	52.8	3.1	0	0	95.72	2108.3

The liquid products collected with a condenser were analyzed to measure the unreacted ethanol and acetaldehyde, a reaction intermediate that can be produced *via* ethanol dehydrogenation. However, the acetaldehyde concentration in the liquid product was negligible, whereas that of ethanol was used to calculate the ethanol conversion. **Fig. 2.10**

plots the 8 h on-stream results at 550 °C for all the catalysts.

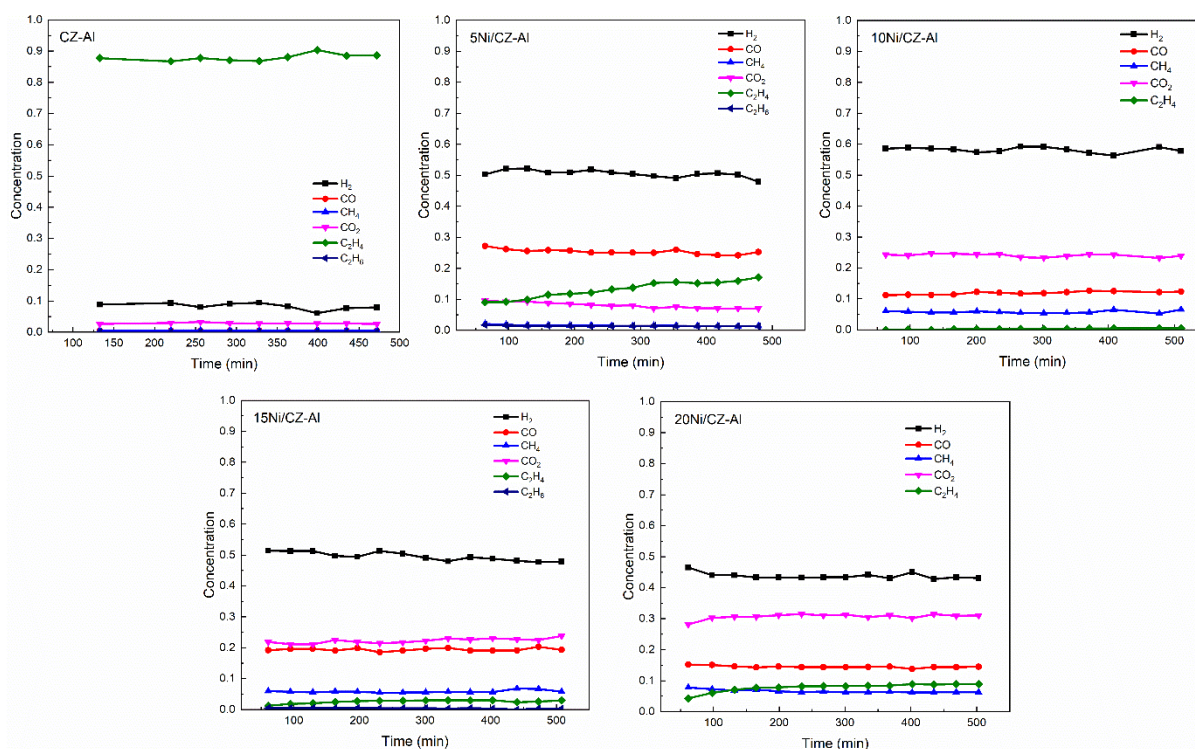


Figure 2.10. Gas production concentration over the xNi/CZ-Al catalyst in ESR obtained from 8 h TOS reaction.

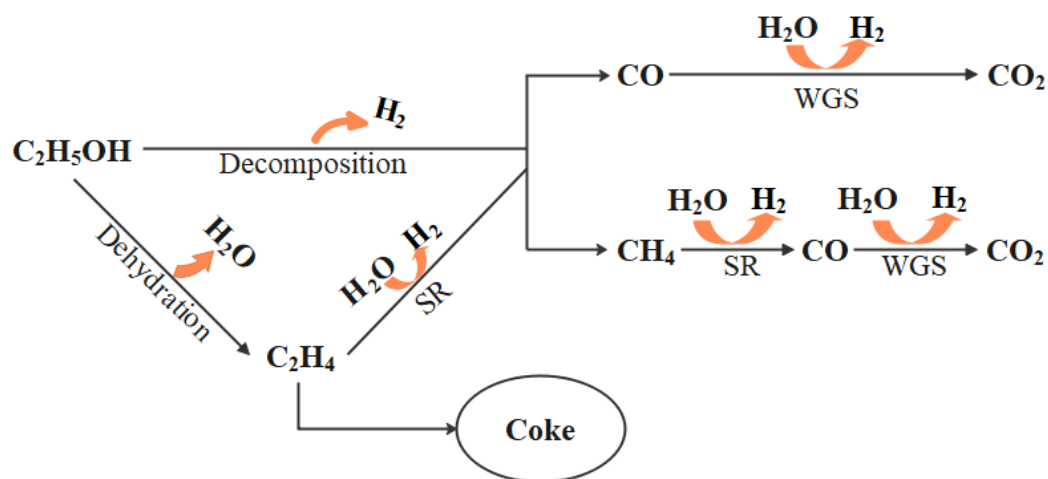
No deactivation was observed during the reaction tests. The ethanol conversion, selectivities of carbon-containing gas products, hydrogen selectivity, and hydrogen production rates were calculated based on the average values of the 8 h-on-stream reaction data. **Table 2.4** lists the calculated values. At 550 °C reaction, over 90% ethanol conversions for the Ni-containing catalysts were achieved, whereas 81.5% of ethanol conversion was obtained for CZ-Al. 5Ni/CZ-Al and 10Ni/CZ-Al specifically reached 100% ethanol conversion in spite of their lower Ni contents. The product distributions relied on the reforming ability over the active sites of the catalysts.

Table 2.4. xNi/CZ-Al catalyst performance of the ESR reaction in 550 °C (reaction conditions: S/C = 3, GHSV = 10619 h⁻¹).

Samples	C ₂ H ₅ OH conversion (%)	C-containing gas products selectivity (%)					H ₂ selectivity (%)	H ₂ production rate (μmol/g _{cat.} .min)	TOF (mmol H ₂ /mmol.min) ^a	Amount of coke (mg _c /g _{cat.} .h) ^b
		CO	CO ₂	CH ₄	C ₂ H ₄	C ₂ H ₆				
CZ-Al	81.5	0.2	1.6	0.3	97.9	0	4.5	87.3	n.a.	4.3
5Ni/CZ-Al	100	39.7	12.7	2.4	40.7	4.4	60.0	956.0	2.6	3.7
10Ni/CZ-Al	100	28.4	57.2	13.3	1.1	0	82.7	1863.0	5.5	5.0
15Ni/CZ-Al	93.6	36.1	41.7	11.1	9.6	1.5	74.0	1361.1	3.5	15.8
20Ni/CZ-Al	91.7	23.9	50.6	10.9	14.6	0	66.3	1110.6	1.9	19.1

(a) Turnover frequency (TOF) is defined as the mmole of hydrogen produced in 1 minute divided by the mmole of Ni metallic site.

(b) The values were obtained from the spent catalyst of the TGA data: g_c/g_{cat.} = gram of coke/gram of the spent catalysts.



Scheme 2.2. Reaction pathways occurring over the xNi/CZ-Al catalysts in ESR.

Scheme 2.2 briefly represents the typical reaction pathways in ESR and the corresponding gas products. In this scheme, unreformed intermediates, such as ethylene and

methane, are indirect indicators of the reforming ability. The low C-containing selectivity of the unreformed intermediates at high ethanol conversion represented a high reforming rate because it showed that the unreformed intermediates were converted from ethanol reform to H₂ and CO/CO₂. From the C-containing gas selectivities in **Table 2.4**, the summated C-containing gas selectivities for the unreformed intermediates (methane, ethylene, and ethane) were plotted with the CO/CO₂ selectivities in **Fig. 2.11**, where the total sum of selectivities for the C-containing gas products was 100%. As shown in the figure, compared to the CZ-Al support with the highest selectivity for unreformed intermediates (98%), the Ni-containing catalysts depicted a significant drop in the intermediate product selectivity. 10Ni/CZ-Al specifically showed the lowest selectivity of *ca.* 14% with 100% of ethanol conversion, demonstrating the highest reforming ability among the catalysts. Metallic Ni catalysts have been widely explored for the steam reforming of hydrocarbons due to the great capacity of the Ni metal phase to activate C–H and C–C bonds in the hydrocarbon molecules [42]. Accordingly, the reforming ability of the Ni catalysts tends to be proportional to the surface areas of the Ni metallic phases. Interestingly, in this study, 10Ni/CZ-Al showed a better reforming ability than 15Ni/CZ-Al and 20Ni/CZ-Al, although the Ni active sites of the latter catalysts were higher than that of 10Ni/CZ-Al.

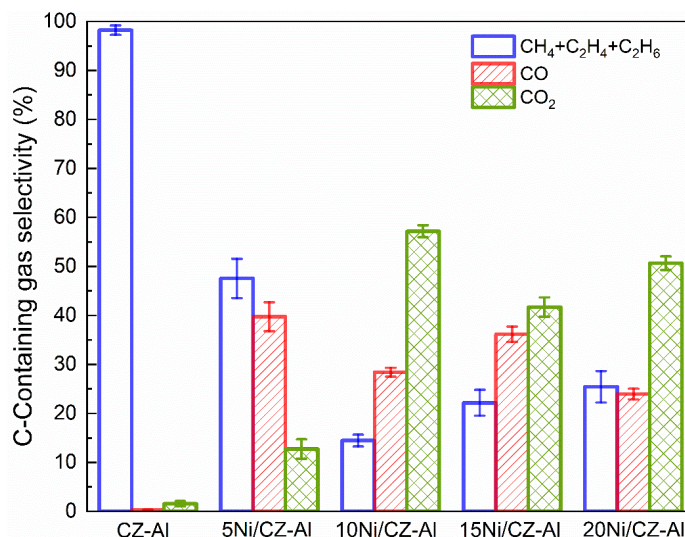


Figure 2.11. Carbon-containing gas selectivity of the catalysts (reaction conditions: S/C = 3, T = 550 °C, GHSV = 10619 h⁻¹).

The hydrogen production rates are a direct indicator of the reforming ability of catalysts. **Table 2.4** presents the hydrogen production rates based on the catalyst weights ($\mu\text{mol/gcat} \cdot \text{min}$). From the values, the hydrogen production rates based on the Ni active sites ($\mu\text{mol/Ni active site} \cdot \text{min}$) were calculated using the Ni active sites in **Table 2.2**. **Fig. 2.12A** shows both hydrogen production rates. The H₂ production rates took on a volcano-shaped pattern with the highest rate for 10Ni/CZ-Al, indicating that 10Ni/CZ-Al had the highest reforming ability. As mentioned earlier, higher Ni active sites can produce more hydrogen by the steam-reforming pathway. However, interestingly, in this study, 10Ni/CZ-Al with less Ni active sites showed the best catalytic reforming performance in terms of the H₂ production rate. That is, the reforming ability of 15 and 20 Ni/CZ-Al was diminished, even though they had more Ni active sites with the increasing Ni contents. Without the Ni species in the catalysts (CZ-Al), the reforming ability of the catalyst almost disappeared, resulting in

a low hydrogen selectivity at 4.5% (**Table 2.4**). In addition, C₂H₄ is a main unreformed intermediate produced by ethanol dehydration that occurred over the acidic sites of Al₂O₃ (**Scheme 2.2**), which was in a good agreement with the previous reports [16, 43-45]. In this study, the C₂H₄ selectivity for CZ-Al was 97.9%, whereas those for the Ni-containing catalysts rapidly dropped because the Ni metallic sites can reform C₂H₄ into H₂ and CO/CO₂ via reaction with steam (**Scheme 2.2**). In **Table 2.4**, the C₂H₄ selectivity for 10Ni/CZ-Al was the lowest at 1.1%, indicating that the reforming ability of 15 and 20Ni/CZ-Al was worse than that of 10Ni/CZ-Al, showing an opposite trend in the H₂ selectivity along with the Ni contents. The H₂ selectivity for 10Ni/CZ-Al was the highest at 82.7%. **Fig. 2.12B** clearly shows the opposite behavior of the C₂H₄ and H₂ selectivities along with the Ni contents.

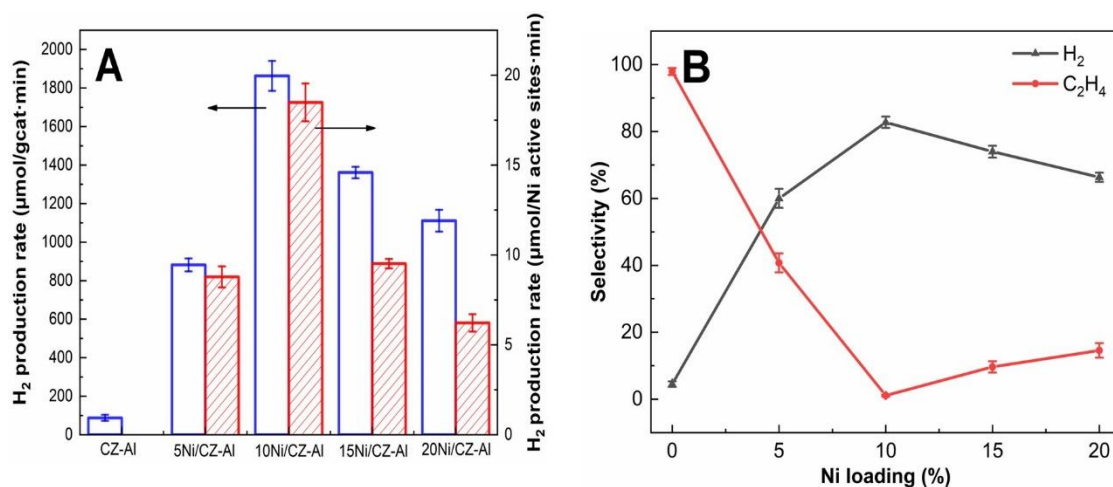


Figure 2.12. (A) H₂ production rate per gram of catalyst and per Ni active site at 550 °C. (B)

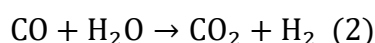
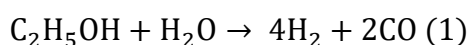
Selectivity of H₂ and C₂H₄ (reaction conditions: S/C = 3, GHSV = 10619 h⁻¹).

The diminished reforming activity of 15 and 20Ni/CZ-Al can be explained by the fact that the added Ni species were over-saturated for the CZ support such as that the excessive Ni

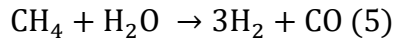
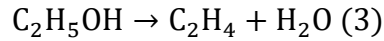
species were mainly located on Al_2O_3 , as proven by H_2 -TPR and XPS. At 550 °C, C_2H_4 was produced on the acidic sites over Al_2O_3 via ethanol dehydration and subsequently reformed into H_2 and CO/CO_2 on the Ni metallic sites. The Ni addition into the CZ-Al support not only introduced the Ni metallic sites over the catalysts but also decreased the catalyst acidity via the NiAl_2O_4 formation. In terms of the catalyst acidity, the acidities for 10, 15, and 20 Ni/CZ-Al were similar, from which we can assume that similar amounts of C_2H_4 would be produced as an unreformed intermediate on the acidic sites of the three catalysts during the reaction tests. Accordingly, the different values in the C_2H_4 and H_2 selectivities for the three catalysts implied the different reforming ability of the Ni metallic sites over the three catalysts. The essential difference in the Ni sites between 10Ni/CZ-Al and 15 and 20Ni/CZ-Al was not in the numbers of the Ni active sites, but in the locations of the Ni metallic sites over the supports. As explained in **Scheme 2.1**, for 10Ni/CZ-Al, the added Ni species mainly interacted with the CZ support, and most of the Ni metallic sites were located over the CZ support where the oxygen vacancy for steam activation was fully developed (saturated Ni–CZ interaction). In contrast, when 15% and 20% Ni were added onto the CZ-Al support, the Ni–CZ interaction was saturated, and the over-saturated (or excessive) Ni species was mainly deposited as the Ni metallic phase on the Al_2O_3 support without the chemical interaction between Ni and Al_2O_3 (little change in acidity compared to the NiAl_2O_4 formation). The Ni metallic active sites over Al_2O_3 (Ni_{Al}) played a different role in the ESR test from the Ni active sites over CZ (Ni_{CZ}). The Ni_{Al} sites were mainly responsible for the reaction pathway to polymerize C_2H_4 to coke at 550 °C, as evidenced by the coke amounts over the catalysts.

Table 2.4 presents the coke amounts formed during the reaction. The coke amounts over 15 and 20Ni/CZ-Al were 15.8 mg_c/g_{cat}·h and 19.1 mg_c/g_{cat}·h, respectively, showing a much greater value than those for the remaining catalysts (3.7–5.0 mg_c/g_{cat}·h). We will discuss the coke formation over the Ni_{Al} sites on the basis of the characterization data of the spent catalysts in the next section.

Meanwhile, the steam reforming occurring on the Ni_{CZ} sites was responsible for both H₂ production and C₂H₄ consumption. 10Ni/CZ-Al had optimal Ni_{CZ} active sites by the saturated Ni–CZ interaction; thus, the catalyst showed the most excellent catalytic performance, that is, the highest H₂ production rate and selectivity and the lowest C₂H₄ selectivity. In addition to the Ni active sites, the oxygen vacancy over the CZ support also played an important role in the reforming process because steam was activated on the oxygen vacant sites over CZ. As a whole, H₂ was produced from both the steam reforming (Eq. (1)) and the water–gas shift reaction (Eq. (2)), where activated steam was involved.



However, as mentioned earlier, ethanol parallelly converted into C₂H₄ and H₂O via ethanol dehydration on the acidic sites over Al₂O₃ (Eq. (3)), and C₂H₄ reformed into H₂ and CO/CO₂ following the reaction pathways (Eqs. (4) and (5)) in **Scheme 2.2**. In detail, the steam activated on the oxygen vacant sites reacted with C₂H₄, or CH₄ activated on the Ni_{CZ} sites whose numbers were saturated below 10% of the Ni loading. The over-saturated Ni species was mainly located over Al₂O₃ for 15 and 20Ni/CZ-Al.



As determined by Raman (**Fig. 2.4B**), the generation of the oxygen vacant sites by the Ni–CZ interaction was saturated below 10% Ni content. For 10Ni/CZ-Al, the oxygen vacant sites for the steam activation and the Ni_{CZ} sites for C₂H₄ and CH₄ activation were fully developed by the saturated Ni–CZ interaction, making 10Ni/CZ-Al show the best reforming ability with the highest H₂ production rate. However, the reason why 10Ni/CZ-Al was the optimal catalyst for ESR in this study was also related to the coke formation over the active sites. Therefore, the coke formed over the catalysts must be characterized, and the coking behavior related to the catalytic performance must be discussed.

2.3.3. Coking behavior over the xNi/CZ-Al catalysts

The amounts of carbon deposited over the spent catalysts after the 8 h ESR tests were measured using the TGA experiment up to 900 °C in air. **Fig. 2.13A** plots the typical weight loss profiles of the spent catalysts. The weight loss was mainly caused by the oxidation of the carbon species deposited on the spent catalysts during the 8 h ESR test at 550 °C. The TGA profiles can be divided into three regions to interpret the phenomena related to the weight losses. Below 200 °C, the weight loss was attributed to moisture removal and volatile impurity [46]. From 200 °C to 450 °C, the weight % increased for the Ni-containing catalysts, and the increasing rates in the weight % were proportional to the Ni contents. The Ni metallic

sites over xNi/CZ-Al were transformed into the NiO phase in air flow, resulting in the catalyst weight increase [47]. The weight loss by the coke combustion occurred from 450 °C to 600 °C, where the weight % for 15 and 20Ni/CZ-Al sharply dropped. The weight loss by the coke combustion was closely connected with the Ni species amounts in the catalysts because the increasing rates of the weight % in 200 °C–450 °C were inversely proportional to the dropping degree in the weight % in 450 °C–600 °C by the coke combustion. **Table 2.4** summarizes the coke amounts over all the spent catalysts quantitatively determined by the TGA measurements. 5Ni/CZ-Al showed the lowest weight loss because the highly dispersed Ni particles and the formation of the NiAl₂O₄ phase [48] exhibited good resistance against the coke formation [49]. **Table 2.4** also shows that 15 and 20Ni/CZ-Al have much higher coking rates, resulting in greater coke amounts of 15.8 and 19.1 mg_c/g_{cat}·h, respectively.

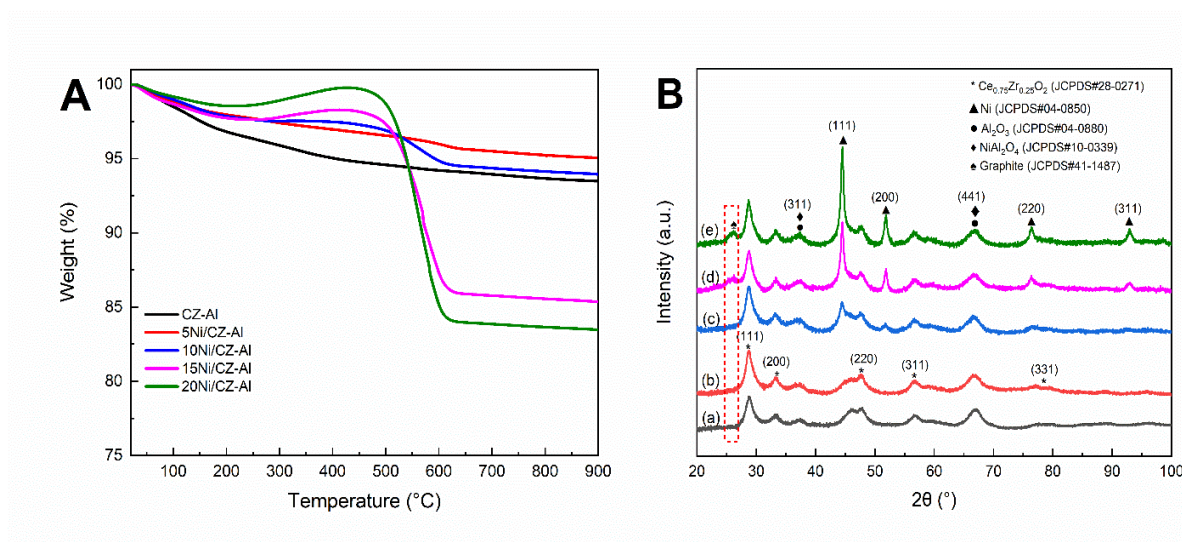


Figure 2.13. (A) TGA profiles for the spent catalysts after 550 °C ESR reaction. (B) XRD patterns of spent xNi/CZ-Al catalysts (a) CZ-Al, (b) 5Ni/CZ-Al, (c) 10Ni/CZ-Al, (d) 15Ni/CZ-Al, and (e) 20Ni/CZ-Al.

The coking behavior was also qualitatively observed by the XRD patterns of the spent

catalysts. **Fig. 2.13B** shows the XRD patterns of the spent catalysts. The assignment of the characteristic XRD peaks in **Fig. 2.13B** was almost the same as those for the fresh catalysts, except for a new peak appearing at $2\theta = 26.1^\circ$ for the spent 15 and 20Ni/CZ-Al catalysts. The XRD peak detected at 26.1° can be assigned to a pregraphitic phase [50] ($2\theta = 26.1^\circ$); thus, the apparent appearance of the peak only for the spent 15 and 20Ni/CZ-Al catalysts reflected a significant carbon deposition on these two catalysts during the ESR tests, which was consistent with the TGA data in this study. The Ni crystallite sizes in the spent catalysts were calculated using the Scherrer equation to check the change in the Ni particle sizes before and after the ESR tests. No change in the Ni crystallite sizes was observed because the estimated Ni particle sizes ranged from 3.1 nm to 10.0 nm.

Fig. 2.14 illustrates the TEM images of the catalysts used in the ESR test for 8 h. While filamentous coke was not detected on CZ-Al, the Ni-containing catalysts clearly exhibited them on the images, indicating that filamentous coke was well developed on the Ni metallic sites. In addition, even at high Ni contents (15 and 20Ni/CZ-Al), the type of coke generated during the reaction was still filamentous (**Figs. 2.14D and E**) while the coke amounts rapidly increased with the Ni contents (**Table 2.4**). The Raman spectra of the spent catalysts were monitored to further observe the coking behavior over the Ni-containing catalysts (**Fig. 2.14F**). In **Fig. 2.14F**, the Raman bands can be divided into three main assignments: G band around 1600 cm^{-1} for the ordered or graphitic aromatic structure; D band at 1350 cm^{-1} for the disordered aromatic structure; and shoulder bands around 1300 cm^{-1} associated with the aliphatic C–H bonds. The Raman spectrum for CZ-Al was distinguishable from those for the

Ni-containing catalysts, confirming that the coke deposited over CZ-Al was different from that over the Ni-containing catalysts. This result was consistent with the TEM data. The relative intensity ratios of the G band to D proportionally decreased as more Ni species were added. **Table 2.1** presents the calculated G/D ratios. The similar behavior in the Raman measurement had been observed in a previous study, which interpreted that coke evolved from an amorphous to a nanocrystalline structure [51]. This was in good accordance with the XRD data herein. On the basis of the observations on the coking behavior from the TGA, XRD, TEM, and Raman measurements, the main coke types formed over the catalysts in the ESR tests were categorized as follows: oligomer coke over CZ-Al; filamentous coke over 5 and 10Ni/CZ-Al; and nanocrystalline pregraphitic coke over 15 and 20Ni/CZ-Al.

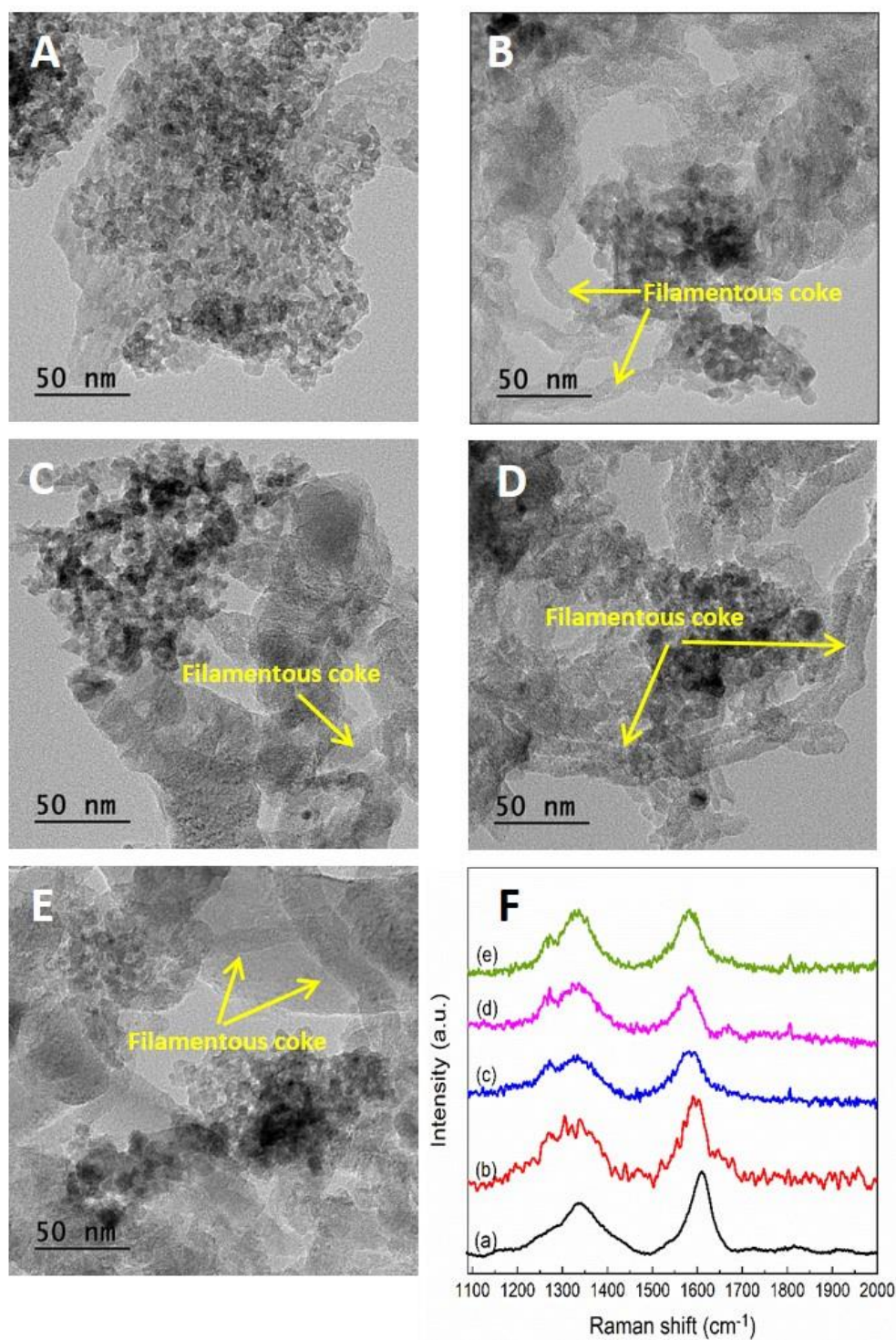
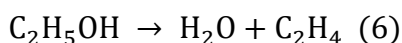


Figure 2.14. TEM images of the spent catalysts (A) CZ-Al, (B) 5Ni/CZ-Al, (C) 10Ni/CZ-Al, (D) 15Ni/CZ-Al, and (E) 20Ni/CZ-Al. (F) Raman spectra of the spent catalysts (a) CZ-Al, (b) 5Ni/CZ-Al, (c) 10Ni/CZ-Al, (d) 15Ni/CZ-Al, and (e) 20Ni/CZ-Al after 8h 550 °C ESR reaction.

According to previous studies on the evolution of the coke formation, the reaction temperature is the most important factor influencing the coke types [52]. The ESR test at 550 °C can evolve the coke types from oligomers and filamentous coke to graphitic coke via coke precursors. Without the Ni species, C₂H₄ is a coke precursor to be converted into oligomers at a limited amount (4.3 mg_c/g_{cat}·h, **Table 2.4**). At low Ni contents, the filamentous coke was mainly formed from CH₄ and CO via the CH₄ decomposition and the Boudouard reaction route. The high Ni loading for 15 and 20Ni/CZ-Al accelerated the formation of the nanocrystalline pregraphitic coke via the graphitization of the restructured filamentous coke. In this case, the over-saturated Ni species near the acidic sites of Al₂O₃ played an important role in the accelerated formation of the nanocrystalline pregraphitic coke. The main gas product for CZ-Al was C₂H₄ with 97.9% C-containing selectivity (**Table 2.4**). Ethylene was produced on the acidic sites of Al₂O₃ via ethanol dehydration (Eq. (6)). The ethylene gas product then acted as i) the coke precursor to form oligomers on the acidic sites (CZ-Al), ii) the unreformed intermediate for the H₂ production over the saturated Ni active sites over the CZ support (5 and 10Ni/CZ-Al), or iii) the coke precursor to the nanocrystalline pregraphitic coke on the over-saturated Ni active sites near the acidic sites (15 and 20Ni/CZ-Al).



To further confirm the role of the Ni site on the CZ support, a 10Ni/Al₂O₃ catalyst was additionally prepared by following the same procedure except for the CZ impregnation. The physicochemical properties of 10Ni/Al₂O₃ are shown in **Table 2.5** and **Fig. 2.15**.

Table 2.5. Physicochemical properties of 10Ni/Al₂O₃ and 10Ni/CZ-Al catalysts.

Sample	BET Surface area (m ² /g)	Pore size (nm)	Pore volume (cm ³ /g)	Ni size (nm) ^{a, b}	Acidic site (mmol _{NH3} /g _{cat}) ^c
10Ni/Al ₂ O ₃	207.5	3.83	0.29	3.2/3.0	0.406
10Ni/CZ-Al ^d	137.7	4.90	0.26	5.6/2.9	0.297

(a) The values were obtained by the application of the Scherrer equation for the characteristic XRD peaks of each crystallite.

(b) The values were obtained from the FFT calculation in the TEM images.

(c) The values were obtained from NH₃-TPD.

(d) The values for this catalyst were also listed in **Table 2.1** and **Table 2.2** and shown here for comparison.

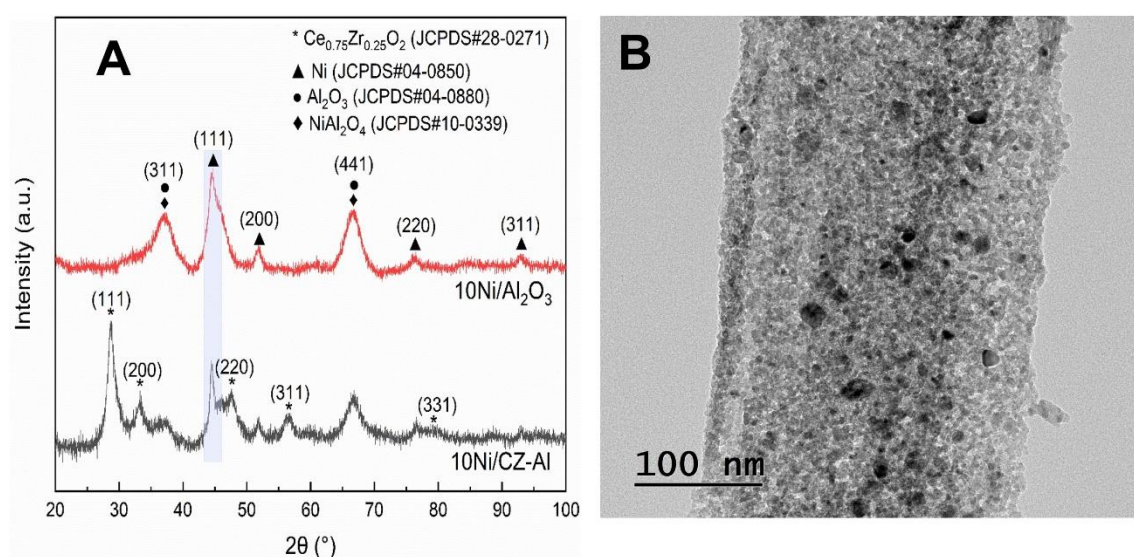


Figure 2.15. (A) XRD patterns of the reduced 10Ni/CZ-Al and 10Ni/Al₂O₃ catalysts and (B) TEM images of the reduced 10Ni/Al₂O₃ catalyst.

Compared with 10Ni/CZ-Al, the 10Ni/Al₂O₃ catalyst possessed a smaller Ni nanoparticle size (3.2 nm) and higher acidity (0.406 mmol_{NH3}/g_{cat}), indicating that the highly dispersed Ni nanoparticles over the Al₂O₃ support having more acidic sites could accelerate ethanol dehydration on Al₂O₃ (Eq. (6)) and successive reforming of ethylene on the Ni sites (Eq. (4)). The reaction results are summarized in **Table 2.6**. Surprisingly, the combined C-containing selectivity of CO and CO₂ for 10Ni/Al₂O₃ was higher than 90% and the corresponding

hydrogen production rate was 1824.8 $\mu\text{mol}/\text{g}_{\text{cat}}$ during the test period of 8 h, demonstrating high reforming ability of 10Ni/Al₂O₃ with an interesting result of the high conversion of unreformed intermediates. More interestingly, 10Ni/Al₂O₃ also produced 27.8 $\text{mg}/\text{g}_{\text{cat.h}}$ of coke, 5.6 times more than that for 10Ni/CZ-Al (5.0 $\text{mg}/\text{g}_{\text{cat.h}}$ of coke), clearly illustrating the severe coking behavior over 10Ni/Al₂O₃.

Table 2.6. 10Ni/Al₂O₃ and 10Ni/CZ-Al catalyst performance of the ESR reaction in 550 °C (reaction conditions: S/C = 3, GHSV = 10619 h⁻¹).

Samples	C ₂ H ₅ OH conversion (%)	C-containing gas products selectivity (%)					H ₂ selectivity (%)	H ₂ production rate ($\mu\text{mol}/\text{g}_{\text{cat.}}\text{min}$)	Amount of coke ($\text{mg}/\text{g}_{\text{cat.h}}$) ^a
		CO	CO ₂	CH ₄	C ₂ H ₄	C ₂ H ₆			
10Ni/Al ₂ O ₃	100	30.1	60.0	8.6	0.2	1.1	86.2	1824.8	27.8
10Ni/CZ-Al ^b	100	28.4	57.2	13.3	1.1	0	82.7	1863.0	5.0

(a) The values were obtained from the spent catalyst of the TGA data: $\text{g}/\text{g}_{\text{cat.}}$ = gram of coke/gram of the spent catalysts.

(b) The values for this catalyst were also listed in **Table 2.4** and shown in here for comparison.

The quantitative coke amounts were calculated from the TGA profiles (**Fig. 2.16A**). The additional measurements of the spent 10Ni/Al₂O₃ catalyst also confirmed the abundant coke formation; the XRD pattern of the spent 10Ni/Al₂O₃ catalysts apparently showed the strongest characteristic XRD peak for pregraphitic coke (**Fig. 2.16B**) and the TEM image (**Fig. 2.16C**) exhibited that the carbon nanotube filaments were well developed over the spent 10Ni/Al₂O₃ catalyst.

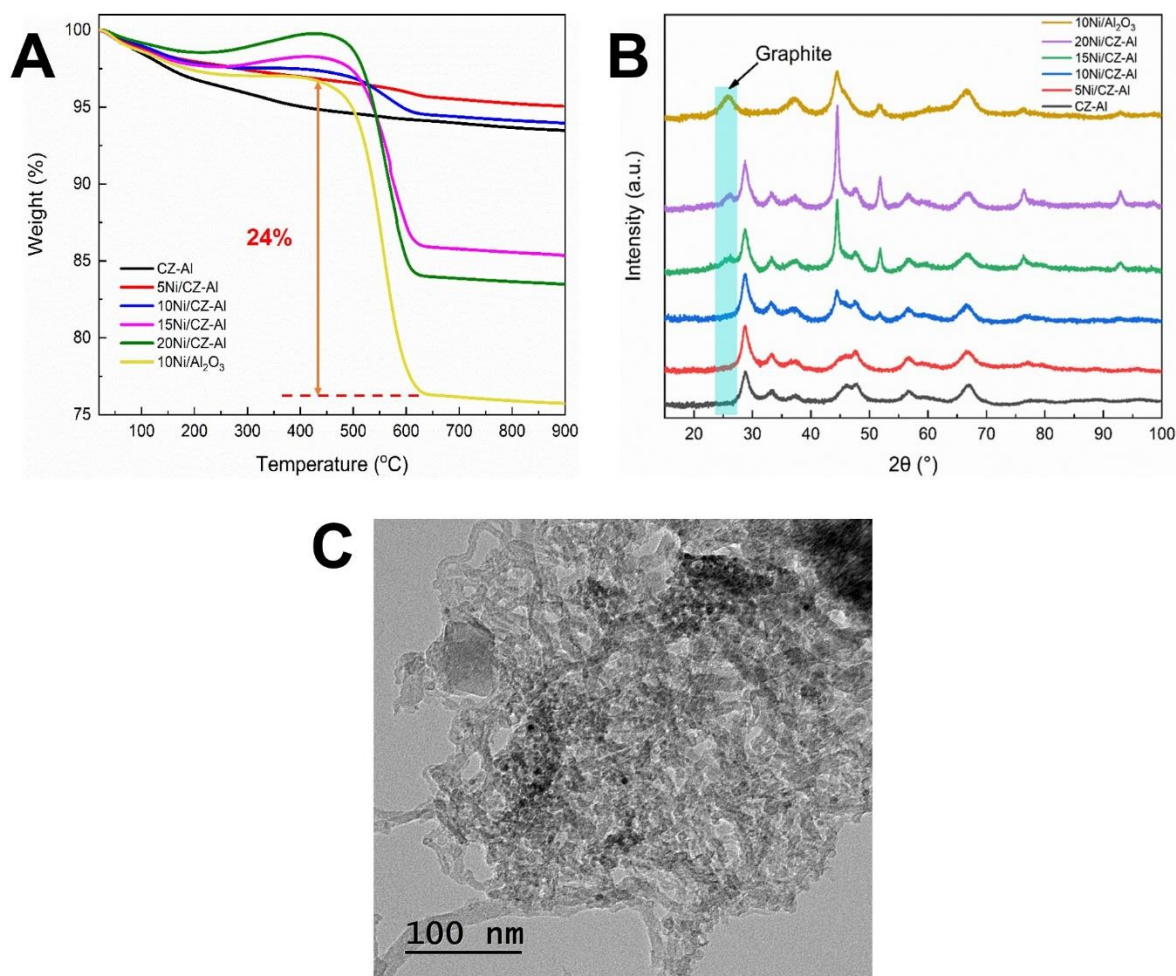
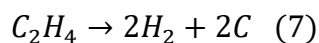


Figure 2.16. (A) TGA profiles for the spent catalysts. (B) XRD patterns of the spent catalysts. (C)

TEM images of the spent 10Ni/Al₂O₃ catalyst after the 550 °C ESR reaction.

This contradictory reaction behavior over 10Ni/Al₂O₃ — the high reforming ability and the severe coke formation can be explained by the high Ni dispersion and abundant acidic sites over 10Ni/Al₂O₃. The acidic sites over 10Ni/Al₂O₃ can generate a large amount of ethylene via ethanol dehydration (Eq. (6)) [53]. Then, the ethylene intermediate reacts on the interface Ni–Al₂O₃ yielding H₂ and pregraphitic coke such as carbon nanotubes (Eq. (7)), whereas the Ni sites catalyze the ethylene steam reforming (Eq. (4)). The high Ni dispersion of 10Ni/Al₂O₃ also enhanced the steam reforming of methane (Eq. (5)), resulting in the lower

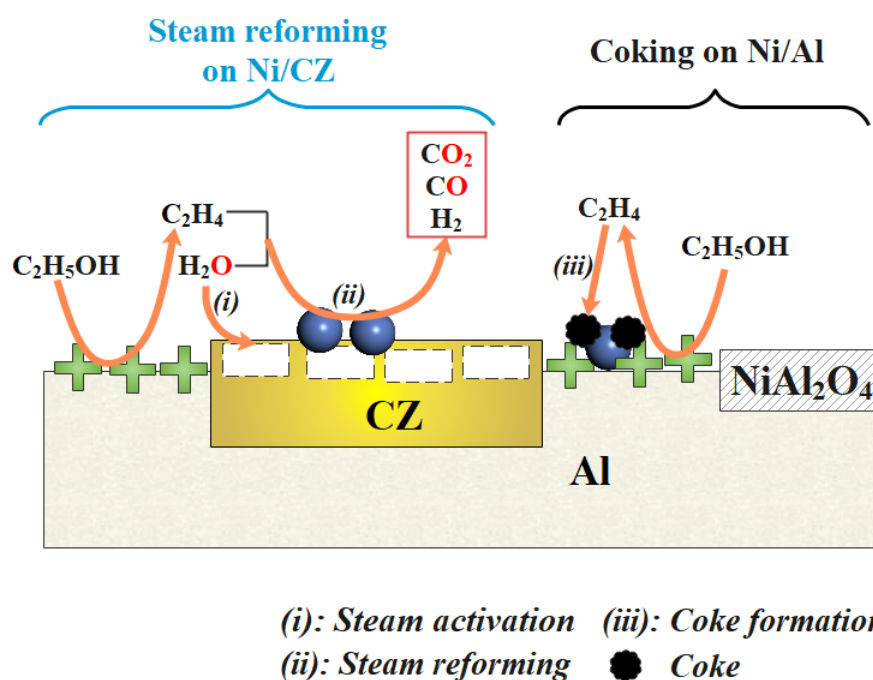
C-containing selectivity of CH₄ and higher H₂ selectivity for 10Ni/Al₂O₃ than those for 10Ni/CZ-Al (**Table 2.6**).



The fact that the 10Ni/CZ-Al catalyst possessed much less coke than 10Ni/Al₂O₃ indicates the effective inhibition over 10Ni/CZ-Al against coking. The impregnation of the CeZrO_x into the Al₂O₃ support induces the difference in the Ni-support interaction. For 10Ni/CZ-Al, the Ni sites are mainly located on the CZ support due to the selective Ni-CZ interaction, suppressing the ethylene decomposition (Eq. (7)) occurring on Ni sites over Al₂O₃, which is beneficial for inhibiting the coke formation.

In summary, **Scheme 2.3** illustrates the reaction pathways related to steam reforming and coking of ethylene in ESR that occurred on the Ni active sites over the CZ support and Al₂O₃, respectively. First, ethanol was converted into ethylene and steam *via* ethanol dehydration on the acidic sites in ESR. For steam reforming, the oxygen vacant sites over the CZ support activated the adsorbed H₂O and provided active species for ethylene reforming. Consequently, on the Ni active sites over the CZ support, H₂ and CO/CO₂ were produced via the reforming process of ethylene combined with steam activation on the oxygen vacant sites over the CZ (Steam Reforming in **Scheme 2.3**). Ethanol and the unreformed intermediates, including ethylene, were reformed by the reaction with the activated steam to produce a mixture of H₂ and CO/CO₂ on the Ni active sites over CZ. However, in the over-saturated Ni-containing catalysts, ethylene produced on the Al₂O₃ acidic sites was converted into pregraphitic coke on the over-saturated Ni active sites near the acidic sites of Al₂O₃, which

was prior to the ethylene migration to the Ni active sites on CZ for the reforming process. Consequently, the selective locations of the added Ni species over the CZ-Al support depending on the Ni loading amount were responsible for the reforming ability and the coke formation over the catalysts.



Scheme 2.3. Steam reforming and coke generation combined steam activation over Ni active sites.

2.4. Conclusions

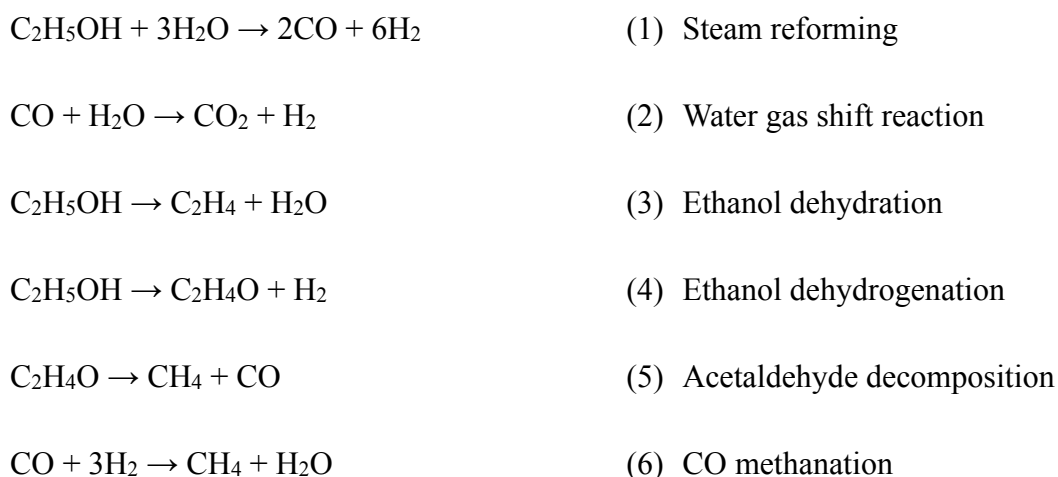
In this study, we investigated the selective Ni–support interactions over Ni/CeZrO_x–Al₂O₃ catalysts along with different Ni loading contents and their influences on the reaction routes in ESR at 550 °C. At low Ni contents (<5 Ni wt.%), the added Ni species preferred the initial formation of NiAl₂O₄, an inactive phase in ESR. For the catalyst containing 10 wt.% Ni, the Ni species mainly interacted with the CeZrO_x support, generating more oxygen vacancies over the CeZrO_x lattice. The oxygen vacant sites and the nearby Ni_{CZ} sites

accelerated the steam reforming combined with steam activation, resulting in the highest hydrogen production rate. However, the over-saturated Ni species (Ni_{Al}) at the high Ni contents (15 and 20 Ni wt.%) was mainly located over the Al_2O_3 support after the Ni– CeZrO_x interaction was fully developed. The Ni_{Al} sites near the acidic sites over Al_2O_3 enhanced the coking behavior from ethylene generated by the ethanol dehydration at 550 °C, resulting in a high coke amount in the spent catalysts. Consequently, the efficient reaction pathways affecting the ESR performance can be controlled by the optimal Ni–support interactions at different Ni loading contents.

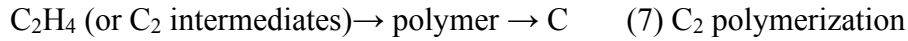
Chapter 3. Optimizing the metal-support interactions by changing CZ/Al ratio over Ni/CeZrO_x-Al₂O₃ catalysts to minimize coking in ethanol steam reforming via efficient gasification routes.

3.1. Introduction

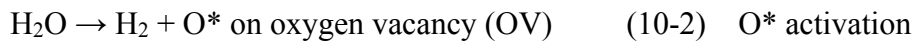
According to a recent report on Ni/CeO₂-ZrO₂-Al₂O₃ catalyst [54], the excessive Ni sites on Al₂O₃ over the 20 wt.% Ni-loaded catalyst enhanced coking routes in ESR, resulting in a high coke amount over the Ni/CeO₂-ZrO₂-Al₂O₃ catalyst. It was also reported that the interaction between Ni and Ce_xZr_{1-x}O₂ influenced the formation of oxygen vacancies and the corresponding catalytic behavior over Ni/Ce_xZr_{1-x}O₂ catalysts for ESR [55]. Recently, several reaction mechanisms for ESR have been proposed based on the final chemicals produced during the catalytic tests [14, 56]. Based on the products analyzed in the studies, simplified reaction routes can be proposed as follows:



In addition to the products-related reaction routes, there are other reaction routes taking place in ESR, which contribute to the carbon conversion, resulting in the formation of coke (C):



Specifically, the acidic sites on Al_2O_3 can polymerize C_2 intermediates to amorphous coke, while the methane decomposition produces a coke precursor (C^*) on the Ni surface, leading to filamentous coke formation [2]. However, C^* on the Ni surface can be eliminated by gasification via the reaction with active oxygen (O^*) generated on oxygen vacancy over $\text{Ni/CeO}_2\text{-ZrO}_2\text{-Al}_2\text{O}_3$ catalysts:



In the coke precursor gasification, the main active sites over $\text{Ni/CeO}_2\text{-ZrO}_2\text{-Al}_2\text{O}_3$ catalysts involve the activation of C^* and O^* . Therefore, it is necessary to control the active sites over the catalysts via the optimized metal-support interactions to maximize the coke precursor gasification, which can provide a solution to the problem in ESR. To the best of our knowledge, there has been no report to describe in detail the coke precursor gasification on the active sites optimized by the metal-support interactions over $\text{Ni/CeO}_2\text{-ZrO}_2\text{-Al}_2\text{O}_3$ catalysts and the corresponding catalytic behavior in ESR.

In this study, we investigated the optimization of active sites distribution via the metal-support interactions over $\text{Ni/Ce}_x\text{Zr}_{1-x}\text{O}_2\text{-Al}_2\text{O}_3$ (CZA) catalysts and the corresponding

catalytic behavior in ESR. Specifically, we examined the coke precursor gasification on the active sites, including the transfer of O*. Different Ni contents (5, 10, 15, and 20 wt%) were impregnated into two CZA supports: 20CZA (20 wt% of CZ and 80 wt% of Al) and 40CZA (40 wt% of CZ and 60 wt% of Al). The properties related to active sites were characterized through different tools, and the ESR tests were conducted at 350 °C and 550 °C. The spent catalysts were further analyzed by thermogravimetric analysis (TGA), Raman spectra, X-ray diffraction (XRD), and Transmission electron microscopy (TEM) to understand coke nature and decoking processes. Based on the obtained results, we proposed that the gasification rate of C* over 20Ni/40CZA was maximized via efficient O* transfer from OV on CZ to C* on the Ni surface.

3.2. Experimental

3.2.1. Catalyst preparation

We used two types of support materials: 20CZA and 40CZA. The preparation of 20CZA and 40CZA involved the solvent hydrothermal method, with respective compositions of CeO₂: ZrO₂: Al₂O₃ = 10:10:80 and 20:20:60 (w/w/w). Precursors were cerium nitrate Ce(NO₃)₃·6H₂O (99%; Sigma–Aldrich, Gyeonggi, South Korea), ZrO(NO₃)₂·xH₂O (99%; Sigma–Aldrich, Gyeonggi, South Korea), and Al(NO₃)₃·9H₂O (JUNSEI, Tokyo, Japan). Otherwise, urea was used as the precipitator, and triblock copolymer Pluronic P123 (PEG–PPG–PEG; Sigma–Aldrich, Gyeonggi, South Korea) was incorporated to facilitate the formation of the porous structure. The Ce(NO₃)₃·6H₂O, ZrO(NO₃)₂·xH₂O, and

$\text{Al}(\text{NO}_3)_3 \cdot 9\text{H}_2\text{O}$ salts were fully dissolved in deionized water using a magnetic stir rotor. Additionally, 2.6 g of P123 was dissolved in 75 ml ethanol. The salt solution and P123 were mixed and transferred to a 200-mL Teflon-lined stainless-steel autoclave. The mixture was then dried in an oven at 80 °C for 5 h and 120 °C for 12 h. After natural cooling to room temperature, the resultant products were filtered and washed with deionized water to obtain the precipitate, which was dried at 70 °C for 24 h and calcined in the atmospheric air at 600 °C for 6 h in the next step.

$x\text{Ni}/20\text{CZA}$ and $x\text{Ni}/40\text{CZA}$ ($x= 5,10,15,20$ wt.%) catalysts were synthesized via the incipient wetness impregnation method using an aqueous solution of $\text{Ni}(\text{NO}_3)_2 \cdot 6\text{H}_2\text{O}$ (Sigma–Aldrich, Gyeonggi, South Korea) to reach 5,10,15,20 wt.% Ni on each support. The catalysts were dried at room temperature for 24 h, then at 100 °C for 12 h in an oven, and calcined at 600 °C for 6 h in a furnace. **Figure 3.1** shows the scheme of the catalyst preparation. The atomic ratio of Ce to Zr was maintained at 1.0 in all the catalysts. The Ni-based catalysts were reduced in a flow of hydrogen at 600 °C for 2 h before conducting catalytic characterization tests excepting the H_2 –TPR experiments.

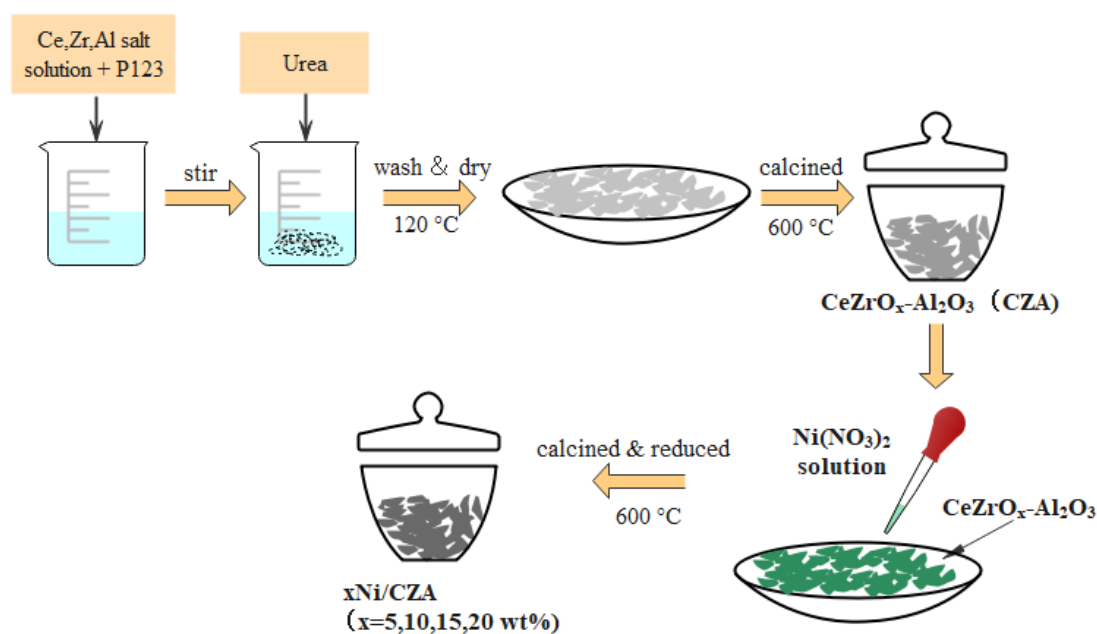


Figure 3.1. The scheme of the catalyst preparation.

3.2.2. Catalyst characterization

The Brunauer–Emmett–Teller (BET) surface area of the catalysts was determined by recording nitrogen adsorption/desorption curves on an ASAP 2020 apparatus (Micromeritics, Norcross, GA, USA) at $-196\text{ }^{\circ}\text{C}$. Before the analysis, the samples were degassed for 24 h at $200\text{ }^{\circ}\text{C}$. Acidic sites were quantified through the temperature-programmed desorption of NH_3 (NH_3 -TPD) using a MicrotracBEL BELCAT-M instrument (MicrotracBEL Corp., Osaka, Japan) with a thermal conductivity detector (TCD). The NH_3 -TPD results were recorded in the temperature range of $50\text{ }^{\circ}\text{C}$ to $900\text{ }^{\circ}\text{C}$. Hydrogen temperature-programmed reduction (H_2 -TPR) and hydrogen TPD (H_2 -TPD) experiments were conducted using a quartz flow reactor installed on a multipurpose analytical system (BELCAT-M, MicrotracBEL Corp., Osaka,

Japan) with TCD. For H₂-TPR, pure N₂ and a mixture of gases (5% H₂ in N₂) were employed as the carrier and reducing gases, respectively. The measurement was performed from 50 °C to 900 °C at a ramp rate of 2 °C/min. H₂-TPD was conducted to verify the dispersion of Ni active sites on the catalyst. Before adsorption measurements, the samples were in-situ reduced with 5% H₂/N₂ at 600 °C, followed by adsorption at 50 °C. Then, the desorption was programmed at a heating rate of 1.5 °C/min from 50 °C to 900 °C under flowing N₂.

The crystal structure was identified using XRD with a Rigaku RAD-3C diffractometer (Rigaku Corp., Tokyo, Japan) and Cu K_α radiation ($\lambda = 1.5418 \text{ \AA}$) at a scanning rate of 2 °C/min for the scattering angle (2θ). The Scherrer equation was used to calculate the crystallite sizes. The morphologies and Ni particle size of the fresh and spent catalysts were examined using high-resolution TEM (HR-TEM) with a JEOL JEM-2100F instrument (JEOL Ltd., Tokyo, Japan). The Ni contents of the samples were measured using an inductively coupled plasma-optical emission spectrometer (ICP-OES; 700-ES Varian, Mulgrave, Australia). Raman spectra were acquired using a DXR Raman microscope (Thermo Fisher Scientific, Waltham, MA, USA) with a 532-nm excitation source.

X-ray photoelectron spectroscopy (XPS) data were obtained using the Thermo K-Alpha XPS instrument equipped with an aluminum K_α X-ray source (Thermo Fisher Scientific, Waltham, MA, USA). The charging effects were calibrated by adjusting the binding energy of the C 1s peak from carbon contamination to 284.8 eV. TGA of the spent catalysts was conducted using a TGA Q50 apparatus (TA Instruments, New Castle, DE, USA). The experiments were performed under flowing air (40 mL/min) and N₂ (60 mL/min) at a heating

rate of 10 °C/min, with a final temperature of 900 °C. The amount of carbon deposition was calculated based on the mass loss profiles observed during the TGA test.

3.2.3. Ethanol steam reforming reaction test

The ESR experiment was conducted in a continuous flow fixed-bed quartz reactor (i.d. = 9 mm) at atmospheric pressure. A mixture of 0.3 g catalysts and glass wool was placed in the middle of a quartz tube. Pure He at a flow rate of 30 mL/min was used as the carrier gas. Before the reduction step, the system was purged. All the calcined catalysts were then in-situ reduced under flowing H₂ (6 mL/min) and He (30 mL/min) at a temperature of 600 °C for 2 h. Subsequently, the sample was cooled to the desired reaction temperature in the stream of He. Water and ethanol were mixed in a fixed steam to carbon molar ratio (S/C) of 3. Once the reaction temperature was reached, the liquid mixture, as the reactant, was continuously injected into the reactor using a high-performance liquid chromatography pump (PCS Pump SP-22-12S, FLOM/JAPAN, 0.01–2.00 mL/min, Tokyo). The inlet lines of the reactor were heated with a heating belt to ensure sufficient vaporization of the reactants. During the reaction, He was also supplied at a flow rate of 70 mL/min as a carrier gas. The gas hourly space velocity (GHSV) for all the reaction tests was set at 10,619 h⁻¹. Before the gas-phase product analysis, the outlet stream was passed through a condenser to separate condensable vapors using a dry-ice condenser. During the reaction test, the gas products were injected into a chromatograph (Acme 6000 GC, YL Instrument Co., Ltd., Dongan-gu, South Korea) every 30 min using an online auto injection system and analyzed by a TCD connected to a

Carboxen column. Calibration curves were established using the standard gas mixture, with He employed as the carrier gas. The liquid products collected with a condenser were analyzed using a chromatograph equipped with a DB-WAX column and a flame ionization detector. The ethanol conversion, hydrogen selectivity and production rate, and C-containing product selectivity were calculated as follows:

$$\text{Ethanol conversion (\%)} = \frac{n_{\text{EtOH}_{in}} - n_{\text{EtOH}_{out}}}{n_{\text{EtOH}_{in}}} \times 100,$$

$$\text{H}_2 \text{ selectivity (\%)} = \frac{n_{\text{H}_2}}{n_{\text{H}_2} + 2n_{\text{CH}_4} + 2n_{\text{C}_2\text{H}_4} + 3n_{\text{C}_2\text{H}_6}},$$

$$\text{H}_2 \text{ production rate } (\mu\text{mol}/(\text{g}_{\text{cat.}} \cdot \text{min})) = \frac{n_{\text{H}_2} \text{ per min.}}{\text{mass of catalysts}},$$

$$\text{C - containing product selectivity} = \frac{j \times n_i}{\sum j \times n_i},$$

where n_i denotes the moles of product i , and j represents the number of carbon atoms in the C-containing product.

3.3. Results

3.3.1 Effect of different CZ/Al ratios on physicochemical properties of the $x\text{Ni}/y\text{CZA}$ catalysts

Figures 3.2a and **b** show that all samples exhibited type-IV (IUPAC) curves, indicating the presence of mesoporous materials with observed hysteresis loops [57]. **Figures 3.2c** and **d** show the pore size distribution calculated from the desorption branches of the N_2 isotherms using the BJH method, revealing that the average pore size of these mesoporous materials ranges from 3.8 to 6.5 nm, as presented in **Table 3.1**.

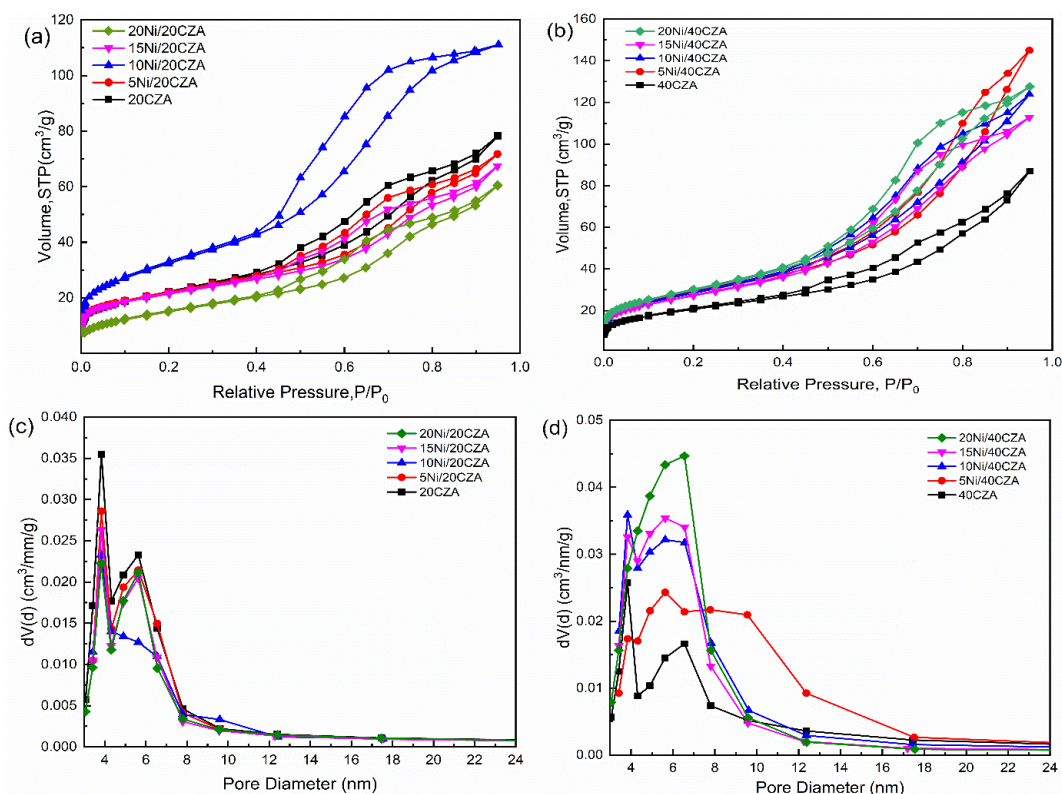


Figure 3.2. N₂ adsorption/desorption isotherms (T=77K) obtained over (a) xNi/20CZA, (b) xNi/40CZA, and BJH pore size distribution of (c) xNi/20CZA and (d) xNi/40CZA catalysts.

The specific surface areas (S_{BET}), pore sizes, and pore volumes are summarized in **Table 3.1**. The S_{BET} values of xNi/20CZA followed a volcanic distribution, obtaining the highest specific surface area of 117.1 m²/g for 10Ni/20CZA. As the Ni content increased further, the S_{BET} value decreased to 74.7 and 56.0 m²/g for 15Ni/20CZA and 20Ni/20CZA, respectively, whereas the pore volumes decreased from 0.18 cm³/g (10Ni/20CZA) to 0.09 cm³/g (15,20Ni/20CZA). This result could be attributed to large Ni species on the catalyst's surface leading to smaller surface areas [58] and the obstruction of pores due to the loading of large Ni species into the pore channels [59]. In contrast, the S_{BET} value increased after adding Ni into 40CZA support and remained high around 100 m²/g at 10, 15, and 20 wt.% Ni content,

indicating that the Ni-support interaction increased the S_{BET} value.

Table 3.1. Physicochemical properties of the xNi/yCZA catalysts.

Sample	S_{BET} (m^2/g)	Pore size (nm)	Pore volum e (cm^3/g)	Acidic site concentra tion ($\text{mmol}_{\text{NH}_3}/\text{g}_{\text{cat}}$) ^a	Ni (wt%) ^b	Ni size (nm) ^{c/d}	CeO ₂ size (nm) ^c	H ₂ consumpti on (mmol/g) ^e	Ni size of spent catalysts (nm) ^f
20CZA	78.1	3.83	0.12	1.515	n.a.	n.a.	13.5	0.40	n.a.
5Ni/20CZA	77.0	3.83	0.10	1.704	4.37	7.3/2.5	12.7	0.89	12.9
10Ni/20CZA	117.1	3.83	0.18	2.983	8.31	5.9/1.4	14.7	1.10	9.6
15Ni/20CZA	74.7	3.83	0.09	1.614	13.25	16.5/28.3	27.9	1.72	41.4
20Ni/20CZA	56.0	3.82	0.09	1.192	18.81	12.0/26.7	22.8	2.14	45.9
40CZA	73.8	3.83	0.13	1.068	n.a.	n.a.	26.2	0.53	n.a.
5Ni/40CZA	102.8	5.63	0.22	1.071	4.28	4.7/7.5	27.0	0.95	6.1
10Ni/40CZA	102.8	3.83	0.19	1.234	9.12	5.3/8.8	27.0	1.32	7.4
15Ni/40CZA	97.4	5.63	0.18	0.967	14.25	6.5/7.9	23.8	1.89	10.9
20Ni/40CZA	107.7	6.55	0.20	1.021	19.33	6.9/5.3	25.3	2.16	18.8

^a The values were obtained from the NH₃-TPD profiles.

^b The values were obtained from the ICP-OES results.

^c The values were obtained by the application of the Scherrer equation for characteristic XRD peaks of each crystallite.

^d The values were obtained from the FFT calculation in the TEM images.

^e The values were obtained from the H₂-TPR profiles.

^f The values are obtained by the application of the Scherrer equation for characteristic XRD peaks of spent catalysts after ESR at 550°C.

The NH₃-TPD experiments were conducted on the xNi/yCZA catalysts. The results are presented in **Table 3.1** and **Fig. 3.3**. All the catalysts showed two main desorption peaks at approximately 200 °C and 750 °C, corresponding to desorptions of ammonia weakly and strongly adsorbed on the acidic sites of the catalysts, respectively. The total acidic sites

reached the highest value of 2.983 mmol_{NH₃}/g_{cat} on 10Ni/20CZA among the xNi/20CZA catalysts and then reduced to 1.614 and 1.192 mmol_{NH₃}/g_{cat} for 15Ni/20CZA and 20Ni/20CZA, respectively. However, despite increasing the Ni loading amount, the total acidic sites almost remained the same over xNi/40CZA catalysts. The trend in the NH₃-TPD data is consistent with that in the BET surface areas (**Table 3.1**). The Ni contents (wt%) of the reduced catalysts were determined using ICP-OES. As presented in **Table 3.1**, the Ni contents of xNi/40CZA catalysts closely matched the expected values, indicating the successful incorporation of Ni into the catalyst structures. In contrast, the Ni contents in the xNi/20CZA catalysts were slightly lower than expected.

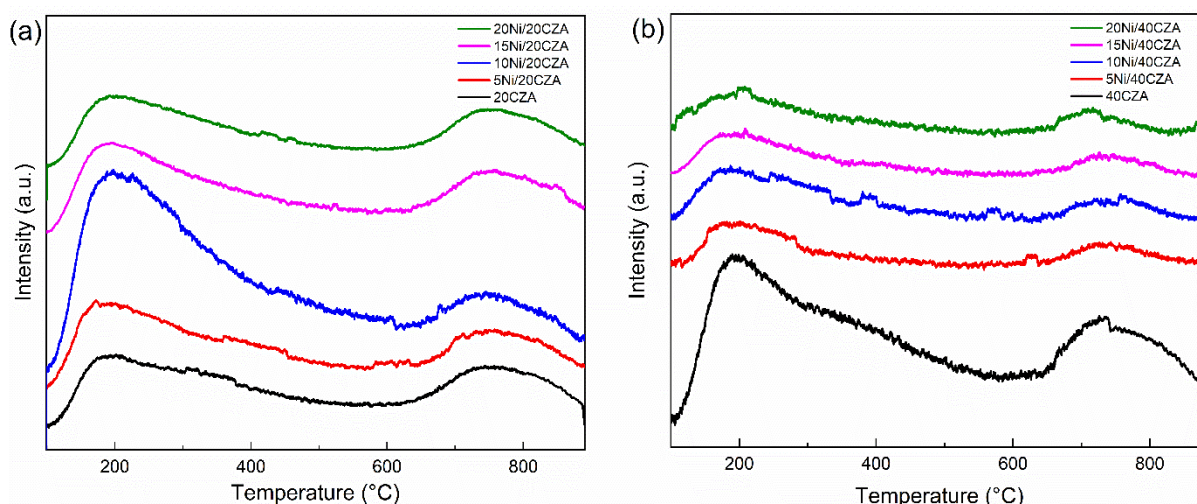


Figure 3.3. NH₃-TPD profiles of (a) xNi/20CZA and (b) xNi/40CZA catalysts.

Figures 3.4a and **b** show the wide-angle XRD patterns of the calcined materials. All the samples exhibited typical diffraction peaks for NiO, which appeared at $2\theta = 37.25^\circ$, 43.28° , 62.88° , 75.41° , and 79.41° , corresponding to (111), (200), (220), (311), and (222) planes of NiO with Fm3m (225) space group (JCPDS#47-1049), respectively. The characteristic XRD peaks for the CZ phase were observed at $2\theta = 28.58^\circ$, 33.18° , 47.58° , 56.56° , 59.52° , 69.68° ,

76.98°, 79.52°, 88.82°, and 95.70°, corresponding to (111), (200), (220), (311), (222), (400), (331), (420), (422), and (511) lattice planes of the CZ solid solution with Fm3m (225) space group (JCPDS#28-0271), respectively. For the xNi/20CZA catalysts with low Ni loading, the diffraction peaks associated with the NiO phase were weak and broad, indicating the formation of small and dispersed NiO particles. However, as the Ni loading increased to 15 and 20% (15 and 20Ni/20CZA), the intensity of the NiO peaks significantly increased, suggesting the formation of large isolated NiO particles due to limited interaction with the support. The intensity of the CZ (111) peak for xNi/20CZA was not as strong as that for xNi/40CZA due to the presence of a weak CZ crystalline structure, which subsequently caused weak interaction with NiO, resulting in isolated NiO phase at the high Ni contents. Meanwhile, for xNi/40CZA, three weak diffraction peaks associated with the NiO phase were observed at $2\theta = 37.25^\circ$, 43.28° , and 62.88° , indicating the formation of well-dispersed NiO crystallites on the support, even at high Ni loading of 15 and 20 wt.%. Moreover, the diffraction peak of CZ (111) for xNi/40CZA was considerably sharper, indicating a strong crystalline structure [60]. The diffraction peak of CZ (111) was also larger and sharper with increasing the Ni contents in the xNi/40CZA catalysts (**Fig. 3.4b**). This suggests that the 40CZA support with a strong CZ solid solution structure led to small NiO nanoparticles since the added Ni species maintained intense interaction with CZ and prevented the NiO nanoparticles from aggregation by anchoring them on the CZ surface. **Figures 3.4c and d** show the relative peak intensities of the CZ (111) and Ni (111) phases, respectively. The intensities significantly decreased to 0.34 and 0.19 for 15 and 20Ni/20CZA catalysts,

respectively, indicating the formation of large Ni particles isolated from the support. However, for xNi/40CZA, the peak intensity remained high (>12), even at the high Ni content, suggesting a uniform dispersion of small Ni nanoparticles that strongly interact with the support over xNi/40CZA.

Figures 3.4e and **f** display the XRD patterns of the reduced catalysts. The appearance of typical XRD peaks at $2\theta = 44.51^\circ$, 51.85° , 76.37° , and 92.94° corresponding to Ni (111), Ni (200), Ni (220), and Ni (311) planes with Fm3m (225) space group (JCPDS#04-0850), respectively, demonstrated a complete transformation of NiO to metallic Ni after reduction treatments. The xNi/40CZA catalyst contained a highly dispersed metallic Ni phase in the support, confirming small Ni nanoparticles, even after the reduction via weak and broad XRD characteristic peaks for metallic Ni. Meanwhile, the 15 and 20Ni/20CZA catalysts exhibited a particularly strong XRD peak intensity of metallic Ni, indicating the formation of large metallic Ni clusters. The crystallite sizes of metallic Ni over the catalysts were calculated using the Scherrer equation, and the results were provided in **Table 3.1**. The crystallite sizes of metallic Ni increased from 5.9 nm for 10Ni/20CZA to 16.5 and 12.0 nm for 15 and 20Ni/20CZA, respectively. In contrast, the Ni crystallite sizes in xNi/40CZA ranged from 4.7 to 6.9 nm (**Table 3.1**). Interestingly, the CZ (111) peak shifted to a higher diffraction angle from its original angle ($2\theta = 28.58^\circ$) at the high Ni content (**Fig. 3.4h**), while there was no shift in the peak position of CZ (111) for the xNi/20CZA catalysts (**Fig. 3.4g**). To further clarify this, the diffraction peak of CZ (111) between 25° and 32° of each sample was enlarged and plotted in **Figs. 3.4g** and **h** for xNi/20CZA and xNi/40CZA, respectively. The 2θ

value for 40CZA is 28.58° , gradually shifting to a higher region of 28.68° with increasing Ni contents. The positive shift could be due to the insertion of Ni into the CZ lattice structure through substitutional exchange with Ce cations during the reduction process. The lower ionic radius of Ni cations compared to Ce cations led to a lattice contraction, compensating for the lattice expansion associated with the formation of oxygen vacancies [61]. During calcination, large NiO particles were formed in 20Ni/20CZA, whereas small NiO nanoparticles were uniformly dispersed on the surface of 20Ni/40CZA. Then, NiO was transformed into metallic Ni in all the catalysts after reduction. For the 20Ni/20CZA catalyst, large isolated Ni clusters were formed over 20CZA due to the limited Ni–CZ interaction. However, for the 20Ni/40CZA catalyst, the highly dispersed NiO nanoparticles were reduced to metallic Ni nanoparticles during the reduction process. Additionally, part of the Ni species was embedded into the CZ lattice structure due to a strong interaction with the CZ support, forming a contracted Ni–O–Ce bonding.

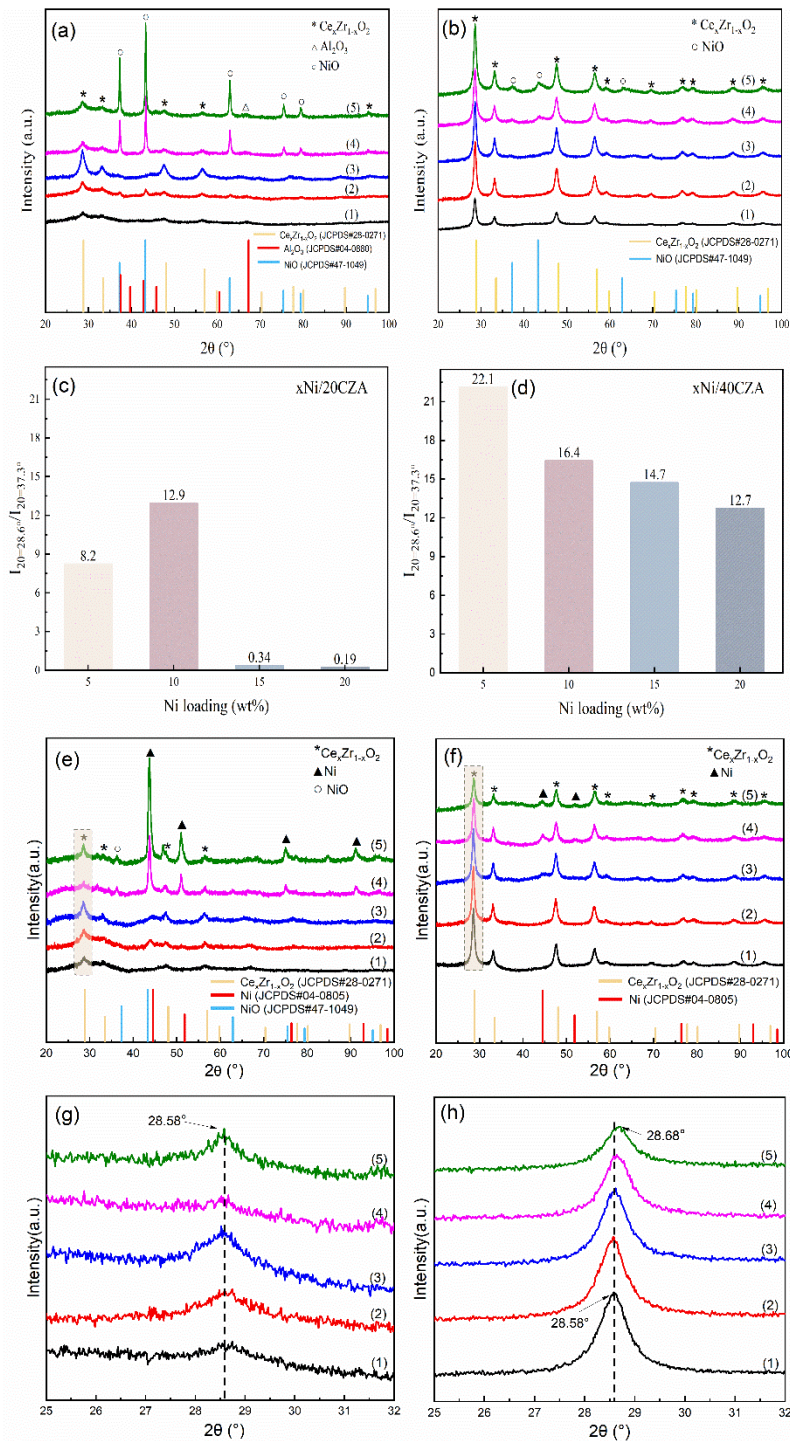


Figure 3.4. (a) XRD patterns of calcined samples of xNi/20CZA. (1) 20CZA, (2) 5Ni/20CZA, (3) 10Ni/20CZA, (4) 15Ni/20CZA, (5) 20Ni/20CZA; (b) XRD patterns of calcined samples of xNi/40CZA. (1) 40CZA, (2) 5Ni/40CZA, (3) 10Ni/40CZA, (4) 15Ni/40CZA, (5) 20Ni/40CZA; (c) relative peak intensity of CeO₂ at 28.6° to NiO at 37.3° for xNi/20CZA; (d) relative peak intensity of CeO₂ at 28.6° to NiO at 37.3° for xNi/40CZA; (e) XRD patterns of reduced samples of xNi/20CZA. (1) 20CZA, (2) 5Ni/20CZA, (3) 10Ni/20CZA, (4) 15Ni/20CZA, (5) 20Ni/20CZA; (f) XRD patterns of reduced samples of xNi/40CZA. (1) 40CZA, (2) 5Ni/40CZA, (3) 10Ni/40CZA, (4) 15Ni/40CZA, (5) 20Ni/40CZA; (g) enlarge area indicated in Fig.3.4 (e); and (h) enlarge area indicated in Fig.3.4 (f).

Figure 3.5 shows the distribution of the HR-TEM images of the reduced samples and corresponding Ni particle sizes. **Table 3.1** presents the average Ni particle sizes determined from the HR-TEM images. A statistical analysis of multiple images revealed a significant increase in the Ni particle sizes from 1.4 nm for 10Ni/20CZA to 28.3 nm and 26.7 nm for 15Ni/20CZA and 20Ni/20CZA, respectively. In contrast, the xNi/40CZA catalysts exhibited a uniform distribution of the small Ni nanoparticles, ranging from 5.3 to 8.8 nm. These findings indicate that the xNi/40CZA catalysts with a well-defined CZ crystalline structure facilitated a uniform and improved dispersion of Ni onto the 40CZA framework, thereby preventing Ni from aggregation. These results are consistent with the findings from the XRD analyses.

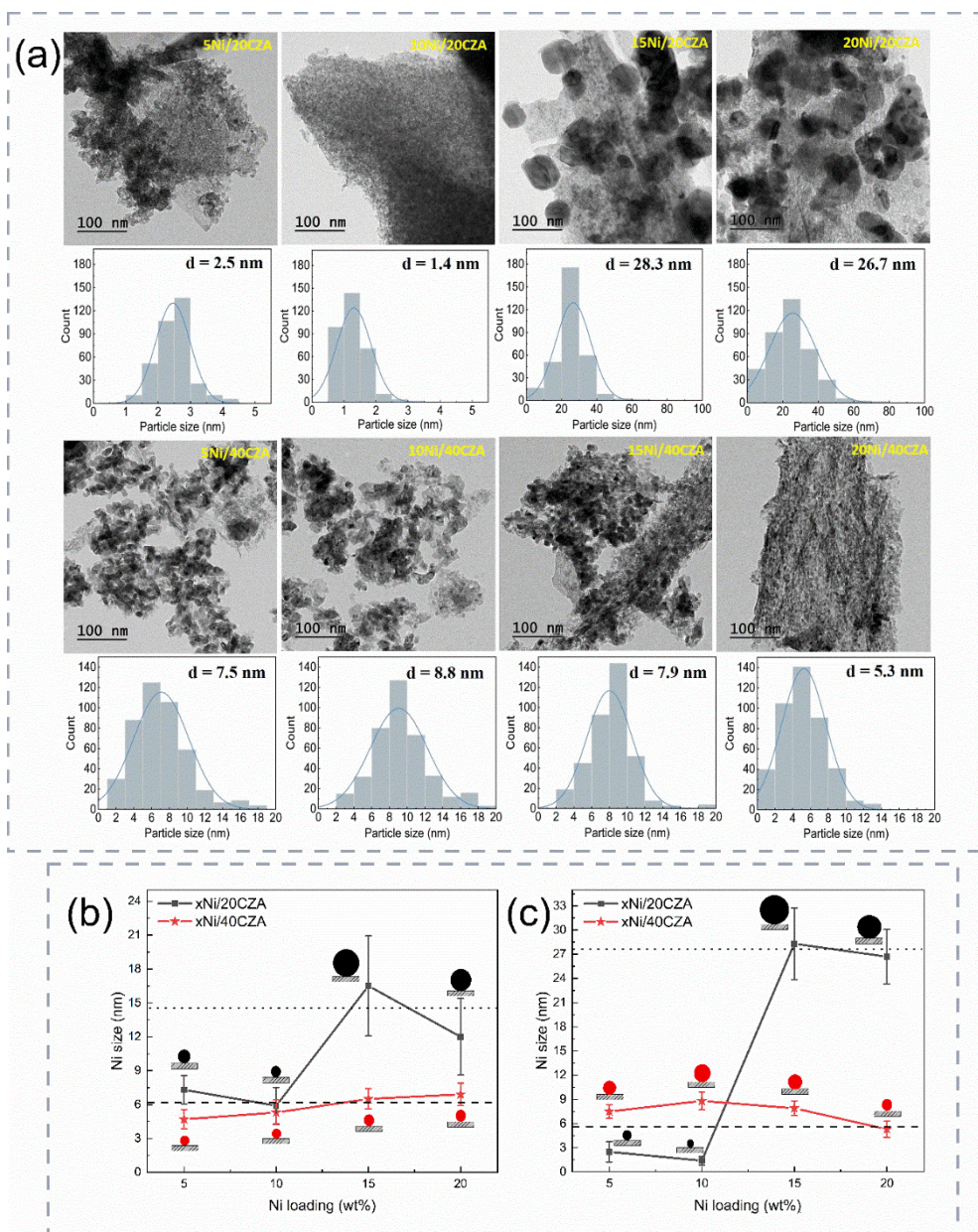


Figure 3.5. (a) HR-TEM images and Ni particle size distribution of reduced xNi/yCZA catalysts; (b,c) relationship between Ni particle size (calculated from XRD and TEM) and Ni loading of reduced xNi/yCZA catalysts (the average Ni particle size of 5, 10Ni/20CZA, and xNi/40CZA is shown in dash line, and the average Ni particle size of 15 and 20Ni/20CZA is shown in dot line).

The H₂-TPR technique was employed to characterize the surface Ni species, oxygen vacancy (OV) concentration, and metal-support interactions on the xNi/yCZA catalysts [62]. The profiles were presented in **Fig. 3.6**, displaying four main reduction peaks at 560 °C (α

peak), 660 °C (β peak), 740 °C (γ peak), and 354 °C (δ peak). The α peak corresponded to the reduction of Ni species with a strong interaction with Al_2O_3 [63]. The β peak presented a strong interaction between Ni and CZ, forming the Ni–O–Ce solid solution [64]. The γ peak corresponded to the reduction of NiAl_2O_4 to metallic Ni [65], whereas the δ peak corresponded to the reduction of isolated NiO particles [66].

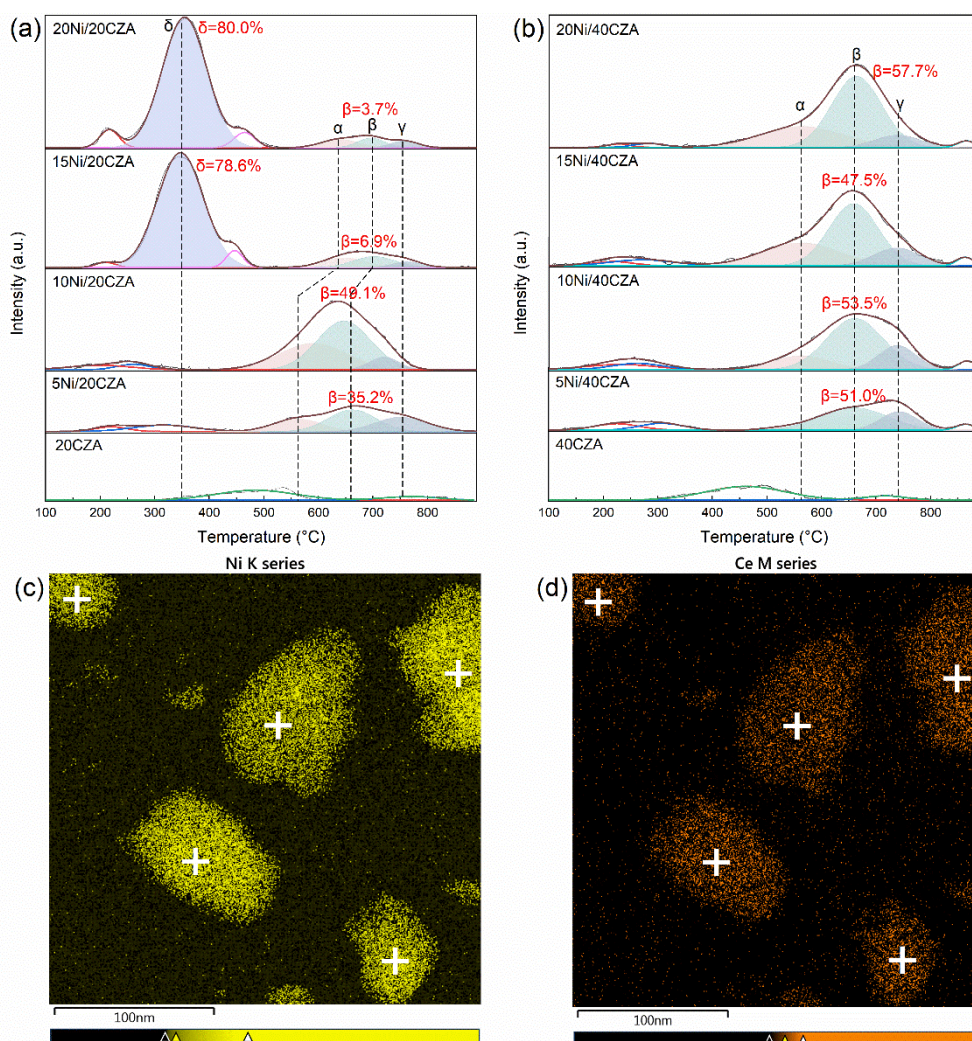


Figure 3.6. H_2 -TPR profiles of (a) xNi/20CZA, (b) xNi/40CZA catalysts, and (c,d) the EDS mapping images of Ni and Ce for 20Ni/20CZA.

Table 3.2 summarizes the quantitative analysis results, including deconvoluted peak areas and OV concentration. It was clear that an increase in the Ni content for 15 and 20Ni/20CZA

decreased the proportion of β peaks and increased the intensities of δ peaks. The reduction peak corresponding to isolated NiO (δ peak) tended to dominate and occupied 78.6% and 80.0% of the total peak area for 15 and 20Ni/20CZA, respectively. Furthermore, α and β peaks of 15 and 20Ni/20CZA shifted to a higher temperature than those of 10Ni/20CZA. These findings suggest that for the xNi/20CZA catalysts, excessive Ni species had limited interactions with the 20CZA support and might contribute to the formation of large Ni clusters; thus, reducing the support reducibility. In contrast, for the xNi/40CZA catalysts, the β peak area dominated and accounted for more than half of the total area, ranging from 47.5% to 57.7%. From the hydrogen consumption amounts presented in **Table 3.1**, it was possible to estimate the OV concentration based on the H₂-TPR results [67] (**Table 3.2**). As shown in **Table 3.2**, when the Ni content increased to 15 and 20%, the OV concentrations (V_0) significantly dropped from 7.82% for 10Ni/20CZA to 0.42% and 0.16% for 15Ni/20CZA and 20Ni/20CZA, respectively. However, for the xNi/40CZA catalysts, despite the high Ni content, the OV concentrations remained high at 7.19% and 8.18% for 15Ni/40CZA and 20Ni/40CZA, respectively. These results indicate that for xNi/40CZA, the addition of Ni to the CZ support enhanced the OV concentration through the strong Ni-CZ interaction, even with a high Ni content. However, for 15 and 20Ni/20CZA, the presence of large Ni clusters indicates the weak interaction between Ni and CZ support, decreasing the CZ reducibility and subsequently decreasing OV concentrations.

Table 3.2. Peak area percentage deconvolved from H₂-TPR and the concentration of the oxygen vacancy (V_o) of xNi/yCZA catalysts.

Sample	H ₂ -TPR peak area percentage (%)				V_o (%) ^a
	α	β	γ	δ	
5Ni/20CZA	20.63	35.23	25.67	n.a.	6.14
10Ni/20CZA	34.28	49.12	7.37	n.a.	7.82
15Ni/20CZA	6.17	6.89	2.63	78.56	0.42
20Ni/20CZA	4.40	3.73	2.66	79.96	0.16
5Ni/40CZA	2.26	51.04	22.70	n.a.	6.72
10Ni/40CZA	14.88	53.54	16.73	n.a.	7.35
15Ni/40CZA	28.36	47.54	12.94	n.a.	7.19
20Ni/40CZA	27.95	57.67	9.22	n.a.	8.18

^a The values were estimated by $V_o = 1 - \frac{3[Ce^{3+}] + 4[Ce^{4+}]}{4}$; the concentration $[Ce^{3+}]$ and $[Ce^{4+}]$ were estimated from the H₂-TPR.

The TPR data can give the information on the Ni location over the supports. In **Table 3.2**, the area percentages of peaks α and β were directly proportional to the relative amounts of Ni located on Al₂O₃ and CZ, respectively. For example, for the xNi/40CZA catalysts, the β peak area percentages ranged in 47.54–57.67%, demonstrating that the Ni species were mainly located on the CZ support even at the 20 wt% Ni loading. On the contrary, even though the area percentages of peaks α and β for 10Ni/20CZA were 34.28 and 49.12%, respectively, their percentages for 20Ni/20CZA dropped up to 4.40 and 3.73%, creating a large portion of peak δ (79.96%) representing isolated Ni clusters. The EDS mapping images of Ni and Ce in **Figs. 3.6c and 3.6d** apparently show that the locations of Ni and Ce over 20Ni/20CZA were similar, indicating that the large isolated Ni clusters were positioned over the CZ support without the creation of oxygen vacancies. The EDS mapping images of all the elements for 20Ni/20CZA are plotted in **Fig. 3.7**.

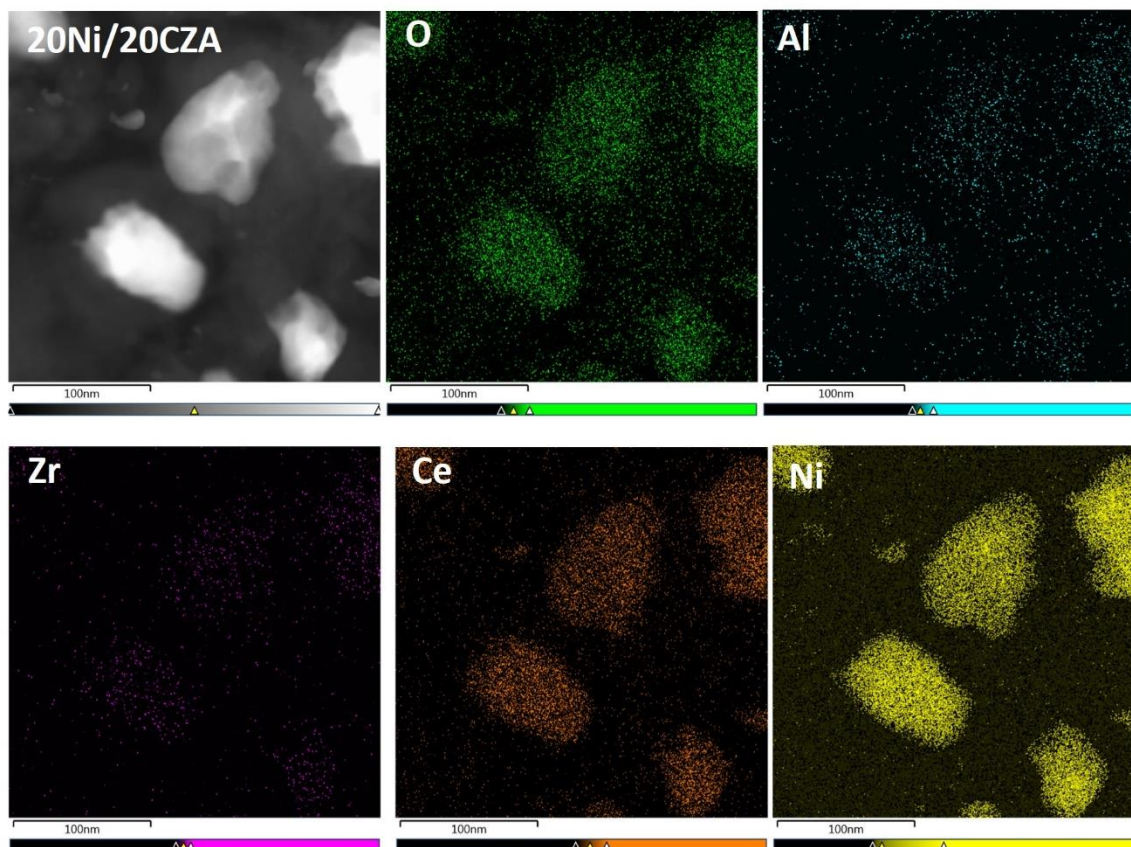


Figure 3.7. EDS mapping images of all the elements for 20Ni/20CZA.

The ESR reaction activity is mainly influenced by the quantity of Ni metallic sites and the concentration of oxygen vacancies. In the subsequent characterization, we primarily conducted quantitative analyses of the content of these two active sites in the catalysts. The Ni dispersion and active sites were determined through the H₂-TPD measurements (**Fig. 3.8**), and the results are presented in **Table 3.3**.

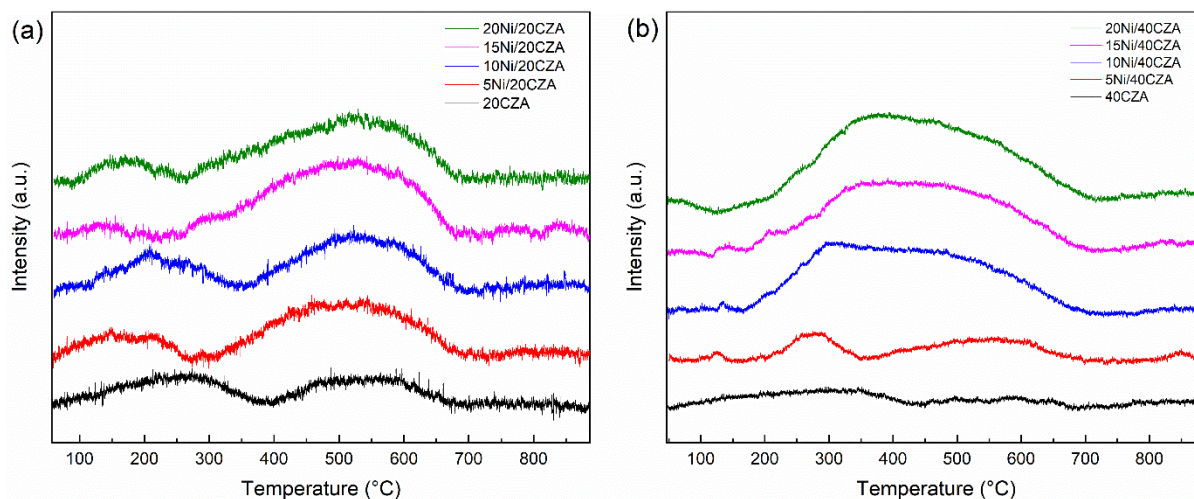


Figure 3.8. H₂-TPD profiles of (a) xNi/20CZA and (b) xNi/40CZA catalysts.

5Ni/40CZA exhibited the highest Ni dispersion of 35.45%. As the Ni loading increased to 10, 15, and 20 wt.%, the Ni dispersion for xNi/40CZA slightly decreased to 28.99%, 19.72, and 13.85%, respectively. However, the values significantly decreased from 30.28% to 13.97%, 7.63%, and 7.63% for the xNi/20CZA catalysts, respectively. This could be attributed to the increase in the Ni nanoparticle size from 5.9 to 16.5 nm with the elevated Ni content for the xNi/20CZA catalysts. Consequently, the corresponding Ni dispersion significantly decreased, decreasing the Ni active sites. In contrast, for the xNi/40CZA catalysts, the smaller Ni crystallites increased the Ni dispersion on the support surface. These findings are consistent with the results obtained from the XRD and HR-TEM analyses.

Table 3.3. Ni metallic site, Ni dispersion, relative intensity ratio of the peaks ($I_{\text{Ce-V/Ce-O}}$ and $O_{\text{ads.}}/(O_{\text{latt.}} + O_{\text{ads.}})$) related to the oxygen vacancy, and $\text{Ce}^{3+}\%$ obtained from XPS of the catalysts.

Catalyst	Ni metallic site (mmol _{H₂} /g _{cat}) ^a	Ni dispersion (%) ^a	$I_{\text{Ce-V/Ce-O}}$ ^b	$O_{\text{ads.}}/(O_{\text{latt.}} + O_{\text{ads.}})$ ^c	$\text{Ce}^{3+}\%$ ^d
20CZA	n.a.	n.a.	0.00	0.16	0
5Ni/20CZA	0.129	30.28	0.01	0.19	0
10Ni/20CZA	0.119	13.97	0.33	0.24	6.46
15Ni/20CZA	0.141	7.63	0.23	0.17	3.71
20Ni/20CZA	0.130	7.63	0.24	0.18	5.24
40CZA	n.a.	n.a.	0.06	0.12	0
5Ni/40CZA	0.151	35.45	0.07	0.17	3.80
10Ni/40CZA	0.247	28.99	0.12	0.21	5.32
15Ni/40CZA	0.252	19.72	0.24	0.29	9.12
20Ni/40CZA	0.236	13.85	0.35	0.32	8.33

^a The values were estimated based on the H₂-TPD measurement.

^b The values were obtained by calculating the ratio of the peak intensity in the reduced catalysts of Raman: $I_{\text{Ce-V/Ce-O}} = \text{Intensity (Ce-V)}/\text{Intensity (Ce-O)}$.

^c The values were obtained by calculating the ratio of peak areas in XPS O 1s spectra: $O_{\text{ads.}}/(O_{\text{latt.}} + O_{\text{ads.}}) = \text{area (adsorbed O)}/\text{area (CZ-O}_{\text{latt.}}) + \text{area (Al-O}_{\text{latt.}}) + \text{(adsorbed O)}$.

^d The values were obtained by calculating the ratio of peak areas in XPS Ce 3d spectra.

The occurrence of surface oxygen vacancies and structural properties of ceria nanomaterials were analyzed by the Raman spectra [68] (**Figs. 3.9a and b**). The characteristic peak detected at 465 cm⁻¹ was assigned to the F_{2g} fluorite structure vibration (Ce-O). As shown in **Figs. 3.9a and b**, the F_{2g} peaks of xNi/40CZA catalysts exhibited sharper characteristics than xNi/20CZA, potentially indicating a stronger crystalline CZ structure of xNi/40CZA [69]. The broad peak at 600 cm⁻¹ corresponded to the defect band associated with oxygen vacancies in the ceria lattice (Ce-V) [25, 70]. For quantitative comparison, the relative intensity ratios of the peaks ($I_{\text{Ce-V/Ce-O}}$) corresponding to the OV concentration for all the catalysts were calculated and presented in **Table 3.3**. It is worth noting that for the

xNi/40CZA catalysts, the relative peak intensity ($I_{\text{Ce-V/Ce-O}}$) steadily increased with increasing Ni loading contents and reached the highest value of 0.35 for 20Ni/40CZA due to the creation of more oxygen vacancies. This finding further confirms that the incorporation of Ni into the CZ lattice, which would more likely occur in the 15 and 20Ni/40CZA catalysts, resulted in uniform dispersion of Ni and increased oxygen vacancies. However, the values decreased from 0.33 for 10Ni/20CZA to 0.23 and 0.24 for 15 and 20Ni/20CZA, respectively, indicating that the Ni–CZ interaction was limited due to a relatively less amount of CZ to Ni, resulting in the presence of isolated large Ni clusters.

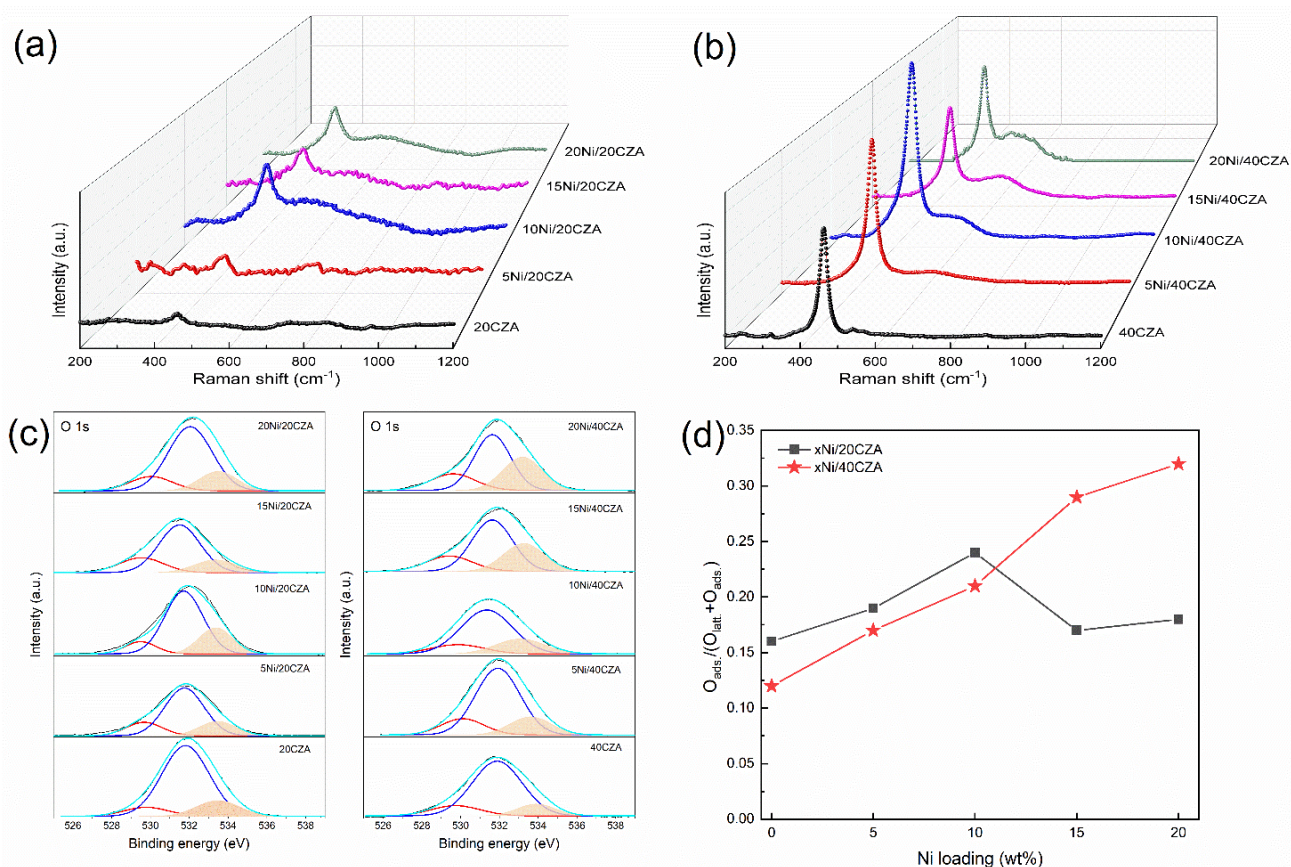


Figure 3.9. Raman spectra of reduced (a) xNi/20CZA and (b) xNi/40CZA catalysts; (c) XPS data of O 1s for reduced xNi/yCZA; (d) $O_{\text{ads.}}/(O_{\text{latt.}} + O_{\text{ads.}})$ ratio (based on XPS of O 1s) as a function of Ni loading amount.

The formation of oxygen vacancies was further confirmed through the analysis of O 1s and Ce 3d XPS data (**Figs. 3.9c, d, and Fig. 3.10**). The O 1s spectra can be deconvoluted into three peaks (i.e., 530.1, 531.6, and 533.1 eV), corresponding to lattice oxygens in the CZ solid solution (CZ–O_{latt.}), and in Al₂O₃ (Al–O_{latt.}), and oxygen adsorbed over OV sites (O_{ads.}) [25, 71-73]. We calculated the relative peak ratios related to OV (O_{ads.}) and presented the results in **Fig. 3.9d** and **Table 3.3**. Notably, the proportion of the O_{ads.} peak for 15 and 20Ni/20CZA catalysts decreased abruptly from 0.24 to 0.17 and 0.18, respectively. In contrast, the O_{ads.} peak area ratio continued to increase in xNi/40CZA. This trend could be attributed to the stronger Ni–CZ interaction forming more oxygen vacancies, resulting in a higher O_{ads.} peak ratio. Ce 3d spectra also supported this finding. **Figure 3.10** depicted the Ce 3d spectra, which revealed the presence of nine peaks corresponding to Ce⁴⁺ and Ce³⁺ components. The fraction of Ce³⁺ was calculated for each catalyst (**Table 3.3**). The results showed that the percentages of Ce³⁺ in xNi/40CZA increased with the Ni contents, reaching 9.12 and 8.33 for 15 and 20Ni/40CZA, respectively. Meanwhile, the percentages of Ce³⁺ in xNi/20CZA, especially for 15 and 20Ni/20CZA catalysts, were significantly lower, measuring 3.71% and 5.24%, respectively (**Table 3.3**).

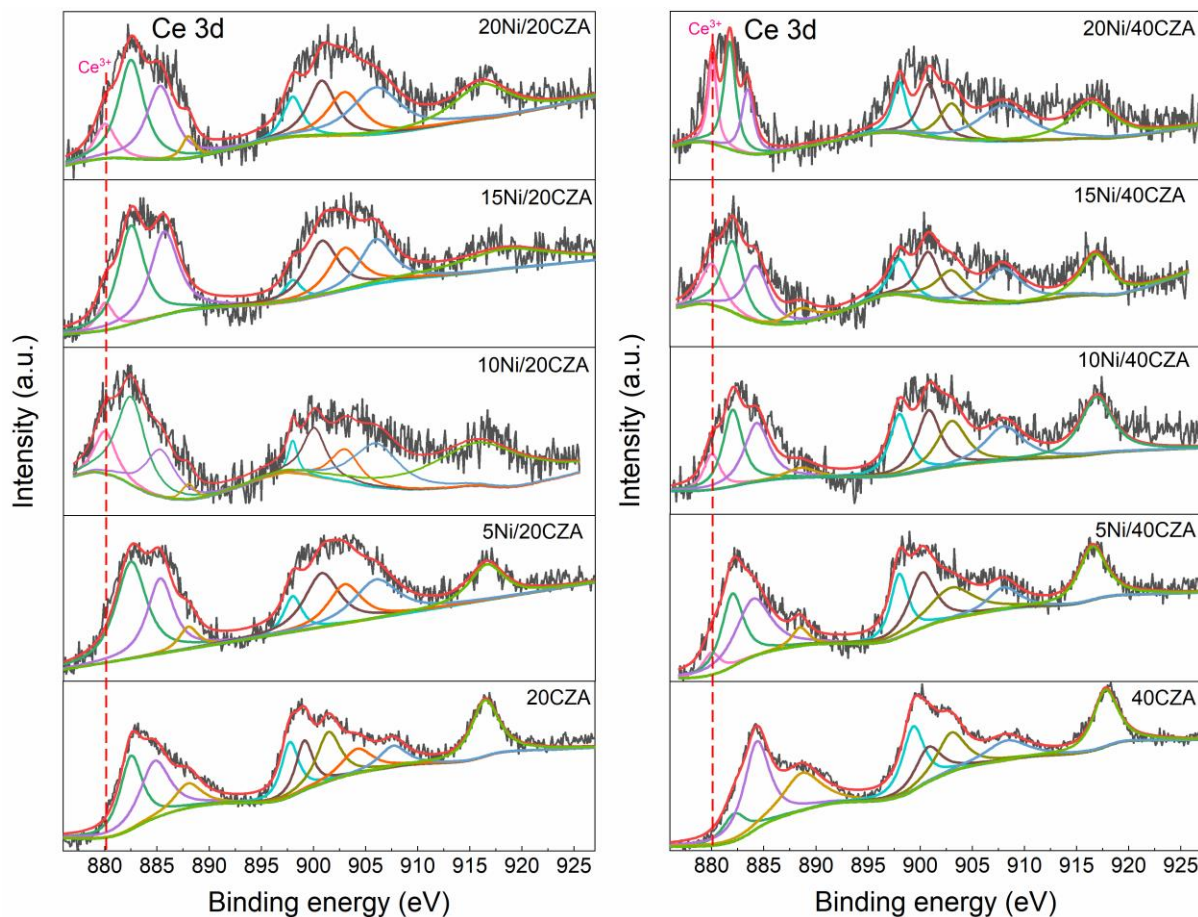
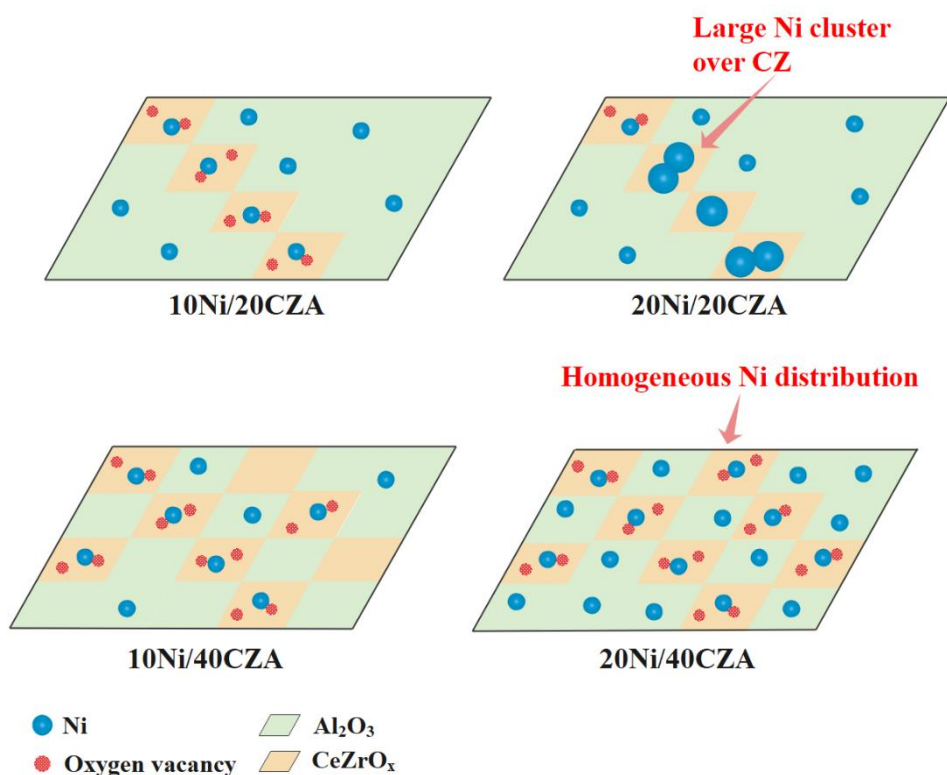


Figure 3.10. XPS data of Ce 3d for reduced xNi/yCZA catalysts.

Based on the characterization data obtained from various techniques for catalytic properties, we illustrate active sites, such as Ni nanoparticles and oxygen vacancies, over the xNi/yCZA catalysts to conceptualize the active sites distribution via optimal metal-support interaction in **Scheme 3.1**. For 10 wt% Ni-containing catalysts (10Ni/20CZA and 10Ni/40CZA), the Ni content was an appropriate amount to make interactions with the CZ support even over 20CZA. This would enable the efficient Ni–CZ interaction to generate the oxygen vacancies over CZ with a uniform and high Ni dispersion over Al₂O₃ and CZ. However, when the Ni content increased to 20 wt%, the metal-support interaction behaved differently depending on the CZ portion over the support. For 20Ni/20CZA, since the Ni

mole number was higher than the CZ portion, the overdosed Ni species were transformed into isolated large Ni clusters due to the limited Ni–CZ interaction. The isolated Ni clusters were mainly positioned over the CZ support, resulting in a decrease in the oxygen vacancies in 20Ni/20CZA. In contrast, for the 20Ni/40CZA catalyst, the CZ portion over the support was still sufficient to facilitate the optimal Ni–CZ interaction, even with an increased Ni content of 20 wt%. This led to a uniform distribution of highly dispersed Ni nanoparticles and the generation of abundant oxygen vacancies over the CZ support.



Scheme 3.1. Schematic illustration of active sites over 10Ni/20CZA, 20Ni/20CZA, 10Ni/40CZA, and 20Ni/40CZA.

3.3.2 Catalytic performance of ethanol steam reforming

The ESR test was conducted at 350 °C and 550 °C for 8 h. During the reaction tests,

hydrocarbon intermediates, such as CH₄, ethylene, and trace amounts of ethane, were detected in the gas phase along with CO, CO₂, and H₂ (Table 3.4).

Table 3.4. ESR reaction results over xNi/yCZA catalysts at 350 °C.

Samples	C ₂ H ₅ OH conversion (%)	C-containing gas products selectivity (%)				C ₂ H ₄ O	C ₃ H ₆ O	H ₂ selectivity (%)	H ₂ production rate (μmol/g _{cat} ·min)	Amount of coke (mgc/gcat.h)
		CO	CO ₂	CH ₄	C ₂ H ₄					
20CZA	25.98	/	/	/	/	/	/	/	/	/
5Ni/20CZA	58.78	11.46	57.05	9.41	0	19.35	2.73	46.41	127.95 (16)	10.46
10Ni/20CZA	77.11	31.59	29.86	25.07	0	12.76	0.72	44.80	316.31 (82)	30.53
15Ni/20CZA	66.13	20.26	39.45	18.14	0	19.74	2.41	60.10	234.09 (19)	15.63
20Ni/20CZA	74.91	34.01	30.01	26.69	0	8.65	0.64	46.61	286.29 (38)	27.17
40CZA	23.09	/	/	/	/	/	/	/	/	/
5Ni/40CZA	59.90	6.12	70.09	4.32	0	17.00	2.47	47.79	116.57 (14)	4.81
10Ni/40CZA	82.46	40.10	22.29	31.06	0	6.36	0.19	45.83	420.18 (39)	25.47
15Ni/40CZA	90.37	35.65	25.57	33.32	0	5.39	0.08	36.26	417.62 (32)	29.20
20Ni/40CZA	92.41	17.00	40.18	39.87	0	2.92	0.04	45.22	591.33 (29)	21.84

Liquid products collected with a condenser were analyzed to measure the unreacted ethanol, acetone, and acetaldehyde. **Figures 3.11** and **3.12** show the 8 h-on-stream results at 350 °C and 550 °C for all catalysts.

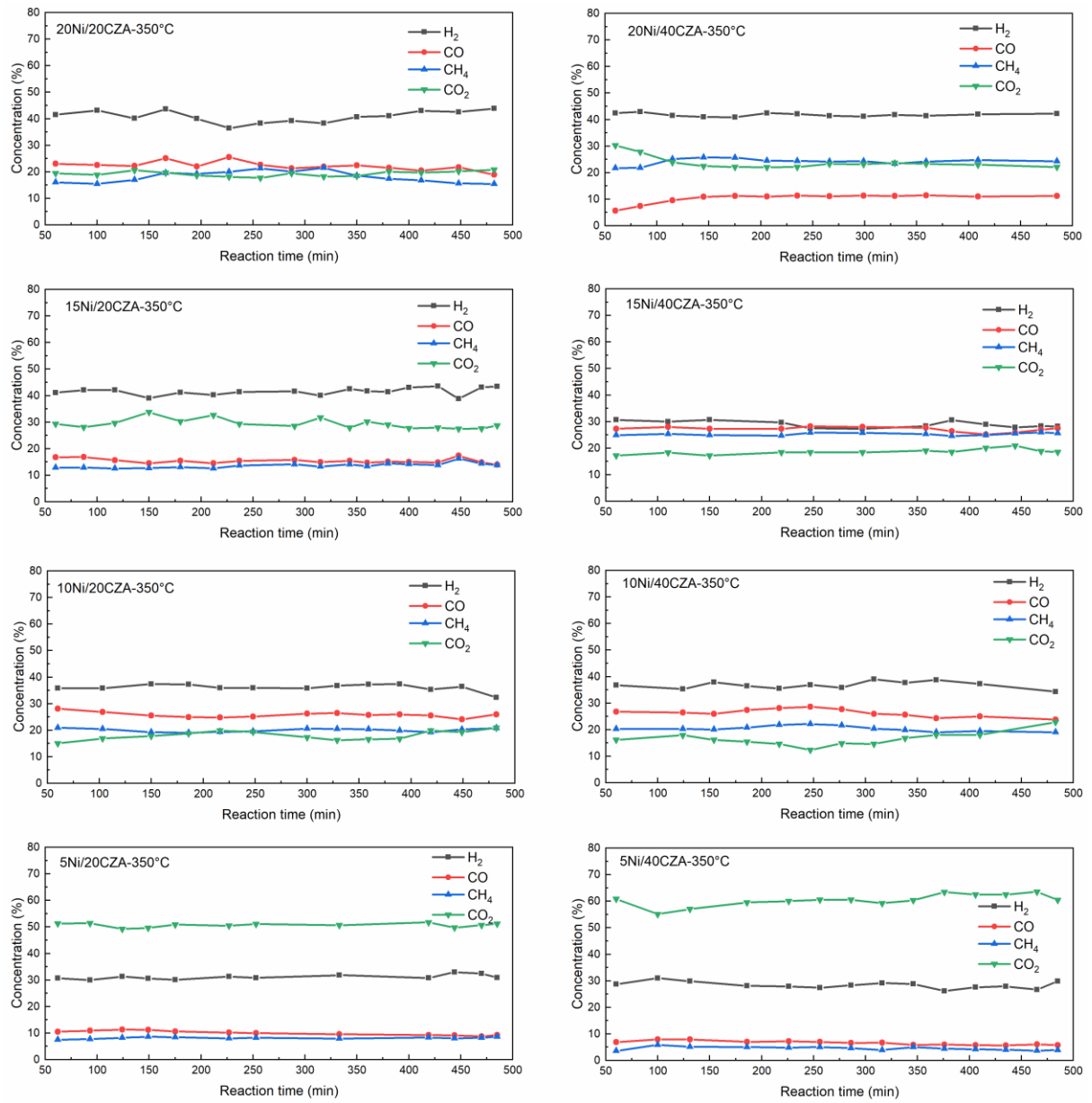


Figure 3.11. 8 h time on stream of gas concentrations in ESR at 350 °C for xNi/yCZA catalysts.

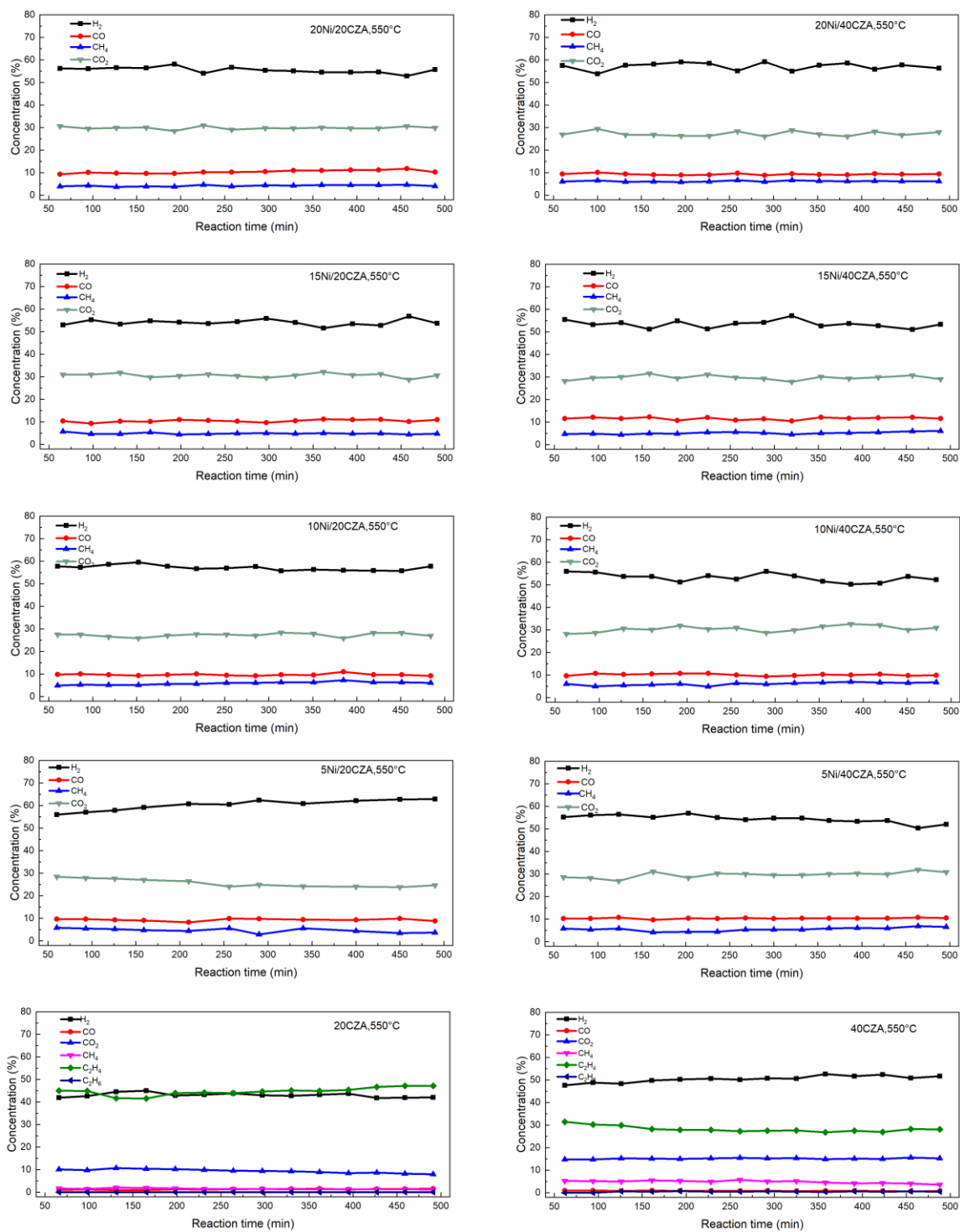


Figure 3.12. 8 h time on stream of gas concentrations in ESR at 550 °C for xNi/yCZA catalysts.

The concentrations of gas products remained stable during the 8-h reaction, and no significant catalyst deactivation was observed. Thus, calculations were performed to acquire the average values of the 8-h on-stream reaction data to determine ethanol conversion,

selectivity of carbon-containing gas products, selectivity of liquid products, H₂ selectivity, and H₂ production rates. The calculated values are presented in **Tables 3.4** and **3.5**.

Table 3.5. ESR reaction results over xNi/yCZA catalysts at 550 °C.

Samples	C ₂ H ₅ OH conversion (%)	C-containing gas products selectivity (%)					C ₂ H ₄ O	C ₃ H ₆ O	H ₂ selectivity (%)	H ₂ production rate (μmol/g _{cat.} ·min)	Amount of coke (mgc/gcat.h)
		CO	CO ₂	CH ₄	C ₂ H ₄	C ₂ H ₆					
20CZA	99.8	2.3	16.2	2.6	77.5	0	1.4	0	31.8	286.4(11)	4.3
5Ni/20CZA	100	22.6	66.6	10.8	0	0	0	0	88.6	804.3(26)	26.2
10Ni/20CZA	100	22.4	64.0	13.6	0	0	0	0	82.9	996.3(26)	23.8
15Ni/20CZA	100	22.6	66.3	10.6	0	0	0.5	0	84.7	867.0 (25)	46.7
20Ni/20CZA	100	23.8	66.6	9.7	0	0	0	0	86.3	955.3(26)	51.4
40CZA	99.9	1.7	30.6	9.7	57.1	0.9	0	0	42.7	457.4(10)	2.4
5Ni/40CZA	100	22.6	65.0	12.3	0	0	0	0	82.8	880.1(13)	20.1
10Ni/40CZA	100	21.5	65.1	13.4	0	0	0	0	81.1	966.6(10)	9.8
15Ni/40CZA	100	24.8	63.8	11.4	0	0	0	0	83.6	887.4 (6)	2.3
20Ni/40CZA	100	21.8	63.7	14.6	0	0	0	0	82.5	1,047.9(15)	8.9

At the reaction temperature of 350 °C, the bare support catalysts, 20CZA and 40CZA, exhibited low activity, with ethanol conversions of 25.98% and 23.09%, respectively. The gas concentrations produced solely over the supports were too low to be detected by gas chromatography. Moreover, the xNi/20CZA catalysts achieved ethanol conversions below 80%, specifically 58.78%, 77.11%, 66.13%, and 74.91% for 5Ni/20CZA, 10Ni/20CZA, 15Ni/20CZA, and 20Ni/20CZA, respectively. In contrast, the xNi/40CZA catalysts exhibited higher ethanol conversion with increasing Ni loading, ranging from 59.90% for 5Ni/40CZA to 92.41% for 20Ni/40CZA catalyst. Notably, the selectivity of liquid products generated by xNi/40CZA decreased to 2.96% with increasing Ni contents, whereas more liquid products were produced in xNi/20CZA (**Table 3.4** and **Figs. 3.13b, c**). This suggests the greater

reforming ability of the xNi/40CZA catalysts, with more Ni metallic active sites, as confirmed by H₂-TPD analysis (Table 3.3). This enhanced reactivity could be attributed to the superior capability of the Ni metal phase to activate C–H and C–C bonds in hydrocarbon molecules [42]. Figure 3.13a demonstrates that the H₂ production rates of xNi/40CZA were higher than those of xNi/20CZA, further substantiating that xNi/40CZA had the better reforming ability of ESR reaction at 350 °C.

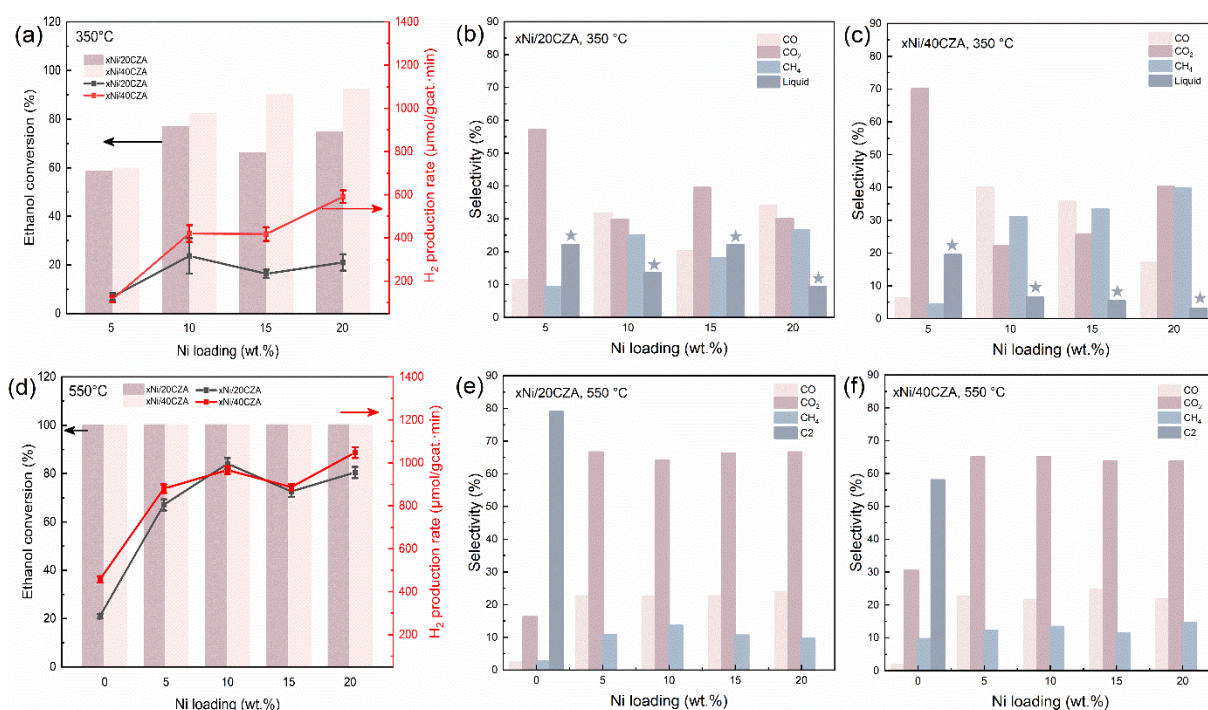


Figure 3.13. (a) The ethanol conversion and average H₂ production rate run at 350 °C, (b,c) the carbon-containing products selectivity over xNi/yCZA catalysts run at 350 °, (d) The ethanol conversion and average H₂ production rate run at 550 °C, and (e,f) the carbon-containing products selectivity over xNi/yCZA catalysts run at 550 °C (Reaction conditions: S/C = 3, GHSV = 10,619 h⁻¹).

Furthermore, the ESR test was also conducted at 550 °C. Figure 3.13d shows that all Ni-containing catalysts achieved 100% ethanol conversion with minimal liquid production, whereas the selectivity of carbon-containing gases in these catalysts remained relatively unchanged (Figs. 3.13e, f). This suggests that the ESR reaction at 550 °C approached a state

of thermodynamic equilibrium. Based on the reaction results, the catalytic performance of xNi/40CZA catalysts was nearly the same as that of xNi/20CZA catalysts, despite having more Ni active sites and sufficient oxygen vacancies. However, the catalyst deactivation resulting from coke formation and CH₄ production as a by-product in ESR is a significant concern for Ni-based catalysts. Thus, we characterized the spent catalysts and investigated the relationship between coke deposition and coke precursor gasification controlled by tuning the Ni-support interaction to minimize the coke formation over the catalysts. Consequently, we observed a significant difference in the coking behavior over xNi/20CZA and xNi/40CZA catalysts at 550 °C.

3.3 Coke precursor gasification and the mobility of O* species over the xNi/yCZA catalysts

Figures 3.14a and b display the XRD patterns of the spent catalysts finishing an 8 h ESR reaction at 550 °C. The characteristic XRD peaks observed in **Fig. 3.14** closely resemble those of the fresh catalysts, except for the emergence of a new peak at $2\theta = 26.1^\circ$ for the spent 15 and 20Ni/20CZA catalysts. The XRD peak detected at 26.1° corresponded to the characteristic peak of carbon nanotubes (CNTs)-typed coke, which could be deconvoluted into two peaks (**Fig. 3.14c**), described as the asymmetric intertube (24.9°) and symmetric intratube (26.0°) structures [74]. Consequently, the exclusive presence of the CNTs peak in the spent 15 and 20Ni/20CZA catalysts indicates a significant carbon deposition on these two catalysts during the ESR tests at 550 °C. Meanwhile, the Ni crystallite size of the catalysts

used for an 8-h ESR reaction at 550 °C was analyzed using the XRD data to investigate the potential occurrence of Ni sintering. The calculated Ni crystallite sizes are presented in **Table 3.1**, indicating a significant increase in the Ni crystallite sizes during the ESR tests for all catalysts. The Ni crystallite sizes for the spent xNi/40CZA catalysts remained below 20 nm, whereas those for the spent 15 and 20Ni/20CZA catalysts exceeded 40 nm. This observation suggests that the strong Ni–CZ interaction for xNi/40CZA inhibited the Ni sintering during the reaction.

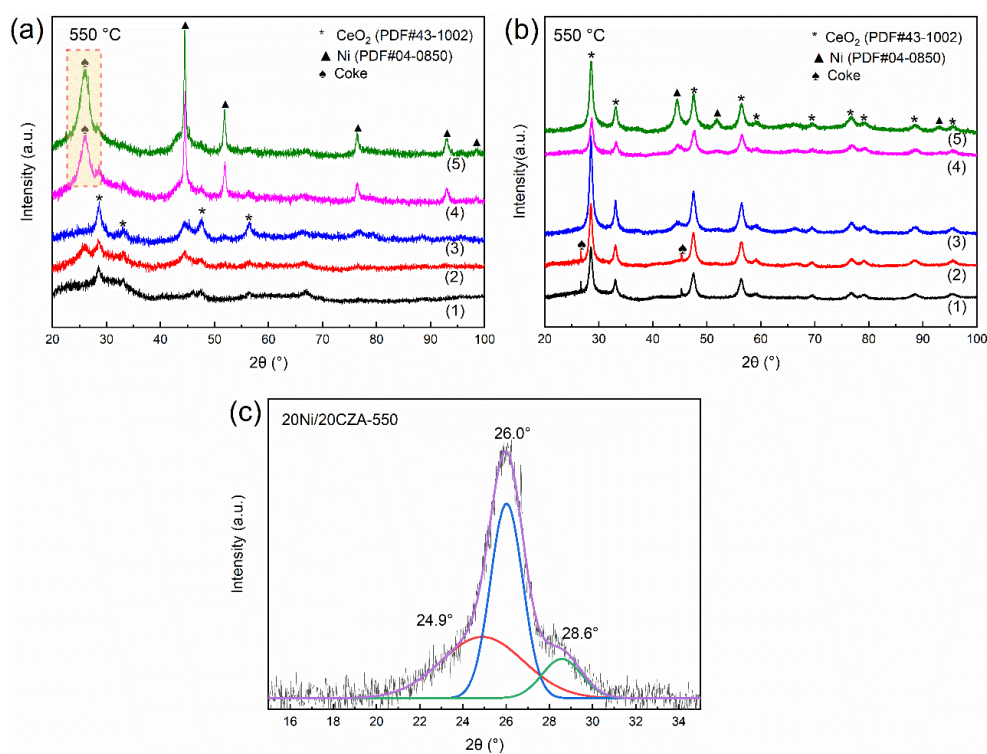


Figure 3.14. XRD patterns of (a) the spent xNi/20CZA catalysts (1) 20CZA, (2) 5Ni/20CZA, (3) 10Ni/20CZA, (4) 15Ni/20CZA, (5) 20Ni/20CZA; (b) the spent xNi/40CZA (1) 40CZA, (2) 5Ni/40CZA, (3) 10Ni/40CZA, (4) 15Ni/40CZA, (5) 20Ni/40CZA after the 8 h reaction at 550 °C, and (c) enlarged XRD pattern of spent 20Ni/20CZA and the deconvoluted peaks.

The amounts of carbon deposited over the spent catalysts after the 8 h ESR tests at 550 °C were quantified by the TGA measurement, and the results are presented in **Table 3.5**. **Figure 3.15** shows the TGA/DTG profiles of the spent catalysts. The weight loss observed in **Figs.**

3.15a and **b** resulted from the oxidation of carbon species deposited on the spent catalysts. Generally, the spent xNi/20CZA catalysts exhibited significantly higher carbon deposition than the spent xNi/40CZA catalysts. The weight losses for spent 5Ni/20CZA and 10Ni/20CZA were around 21%, which sharply increased to 41% for spent 15Ni/20CZA and 20Ni/20CZA catalysts, indicating a substantial coke formation. In contrast, the spent xNi/40CZA catalysts displayed a relatively low weight loss, particularly the spent 15Ni/40CZA and 20Ni/40CZA catalysts, with a weight loss of 7%. **Figure 3.15e** illustrates the trend diagram depicting the change in the coke amounts with increasing Ni contents for spent xNi/20CZA and xNi/40CZA catalysts. Interestingly, the spent xNi/20CZA and xNi/40CZA catalysts exhibited opposite trends in the amount of coke formation with the Ni contents. Specifically, there was a sudden increase in the coke amount for the spent 15Ni/20CZA and 20Ni/20CZA catalysts. In contrast, the coke amount decreased for 15Ni/40CZA and 20Ni/40CZA catalysts. This observation indicates that the gasification of carbon species over spent 20Ni/40CZA was dominant during ESR, whereas the coke formation was accelerated for the spent 20Ni/20CZA catalyst. **Figure 3.15f** exhibits the coke amounts based on the Ni amounts, demonstrating that the coke precursor, C*, over 20Ni/40CZA was readily gasified, compared with 20Ni/20CZA. Meanwhile, the combustion temperature of the coke was over 500 °C for all the spent catalysts, indicating the formation of a filamentous coke (**Figs. 3.15c,d**).

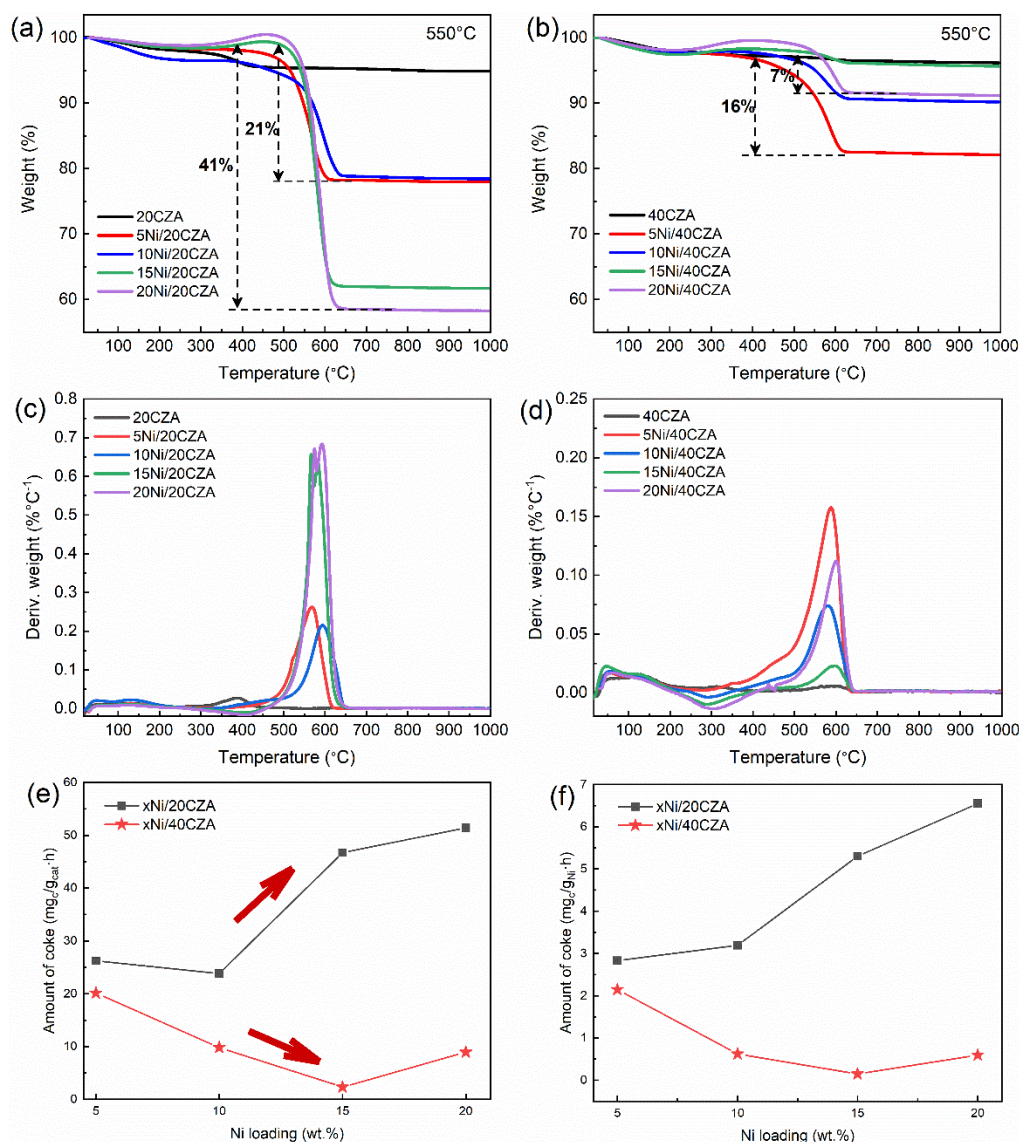


Figure 3.15. TGA/DTG profiles of spent catalysts (a, c) xNi/20CZA; (b, d) xNi/40CZA after 8 h ESR reaction at 550 °C, and (e,f) amount of coke after 8 h ESR reaction at 550 °C calculated by TGA results as a function of Ni loading amount.

Figure 3.16 shows the TEM images of the catalysts used in the ESR test at 550 °C. Although CNTs were not detected on the spent 10 and 20Ni/40CZA catalysts, a clear development of CNTs was observed on the spent 10 and 20Ni/20CZA catalysts. Interestingly, the diameters of CNTs on the spent 10Ni/20CZA catalyst were small, approximately below 15 nm, whereas those on the spent 20Ni/20CZA catalyst were greater than 35 nm. This

observation demonstrated a correlation between the diameter size of CNTs generated during the ESR test and the Ni particle sizes. In literature, the coke in ESR was formed i) the ethylene (or C₂ intermediates) polymerization (eq. 7), ii) the CH₄ decomposition (eq. 8), and iii) the Boudouard reaction (eq. 9) [14, 75]. Specifically, at 550 °C, the C* decomposed on the Ni surface from CH₄ could grow CNTs-typed coke, depending on the reaction conditions and catalytic properties. During the ESR reaction, C* on the Ni surface can proceed via two competing reaction routes: coking to CNTs or gasification to CO via the reaction with O*. For 10Ni/20CZA and 20Ni/20CZA, it was evident that the coke formation primarily occurred with the coke amount of 51.4 mgc/gcat.h for 20Ni/20CZA (**Table 3.5**). The primary coke type observed on the xNi/20CZA catalyst was CNTs with varying diameter sizes. In particular, the large Ni clusters (26.7 nm) in the spent 20Ni/20CZA catalyst resulted in coarse CNTs (diameter > 35 nm), whereas small Ni nanoparticles in the spent 10Ni/20CZA catalyst produced fine-scale CNTs (diameter < 15 nm). These findings were confirmed through the XRD and HR-TEM measurements [76]. Meanwhile, the C* gasification on the Ni surface for the xNi/40CZA catalysts was dominant instead of the coke formation. The coke amounts for 15 and 20Ni/40CZA catalysts were only 2.3 and 8.9 mgc/gcat.h, respectively (**Table 3.5**), and the TEM image for spent 20Ni/40CZA was clean without coke (**Fig. 3.16**). The different coking behavior between 20Ni/20CZA and 20Ni/40CZA could be attributed to the relative rates of coking and gasification pathways, including activation and transfer of O* over the catalysts.

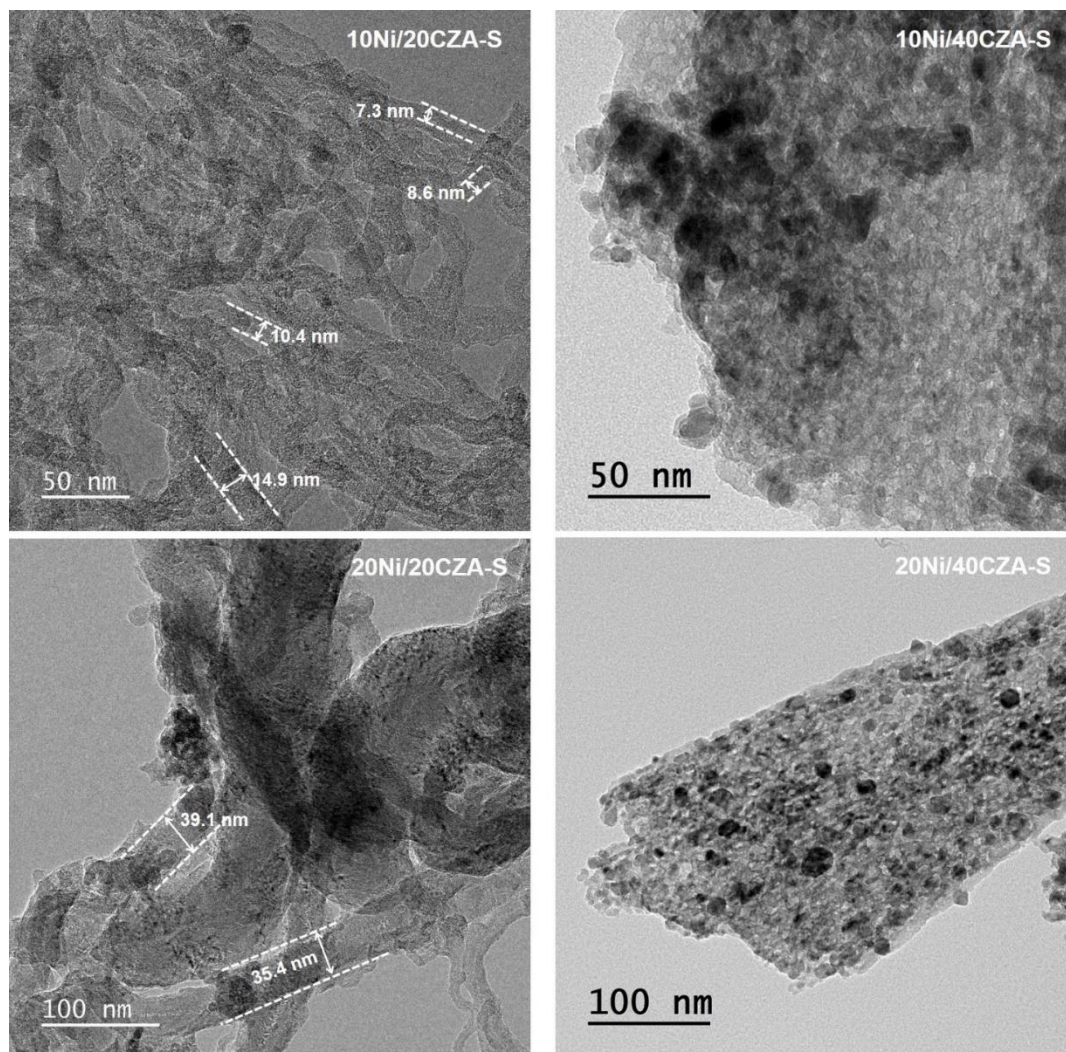
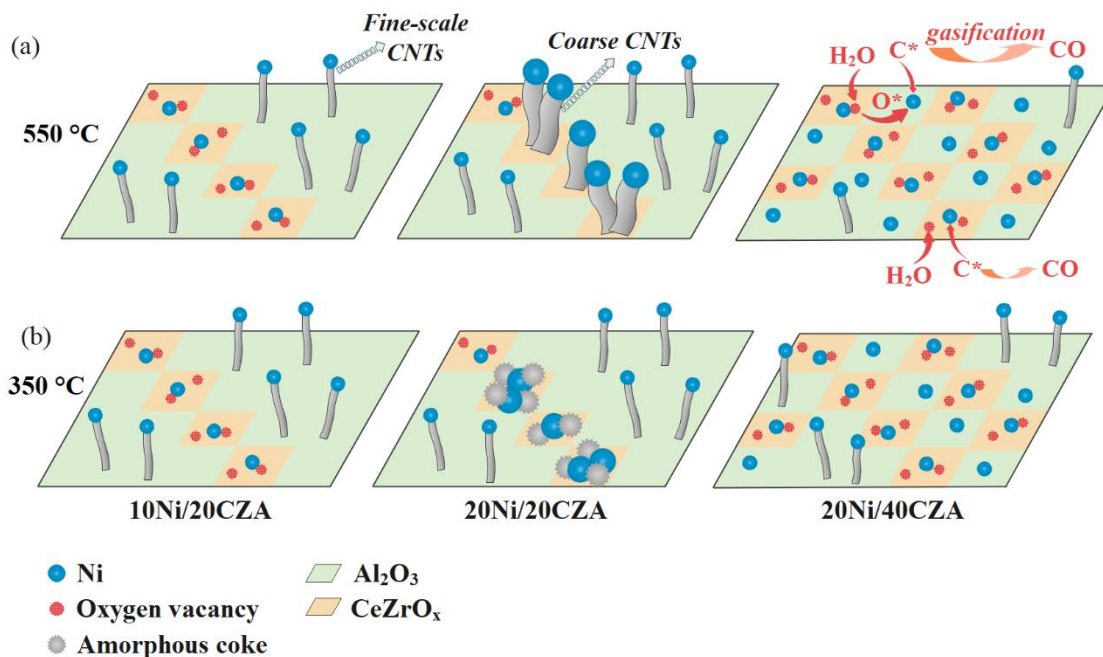


Figure 3.16. TEM images of spent $x\text{Ni}/y\text{CZA}$ catalysts used in the ESR at $550\text{ }^{\circ}\text{C}$.

Scheme 3.2a illustrates the coke formation over 10 and 20Ni/20CZA and C^* gasification over 20Ni/40CZA at $550\text{ }^{\circ}\text{C}$. The growing mechanism of CNTs involves the generation of C^* on the Ni surface, the C^* diffusion through Ni crystallites, and the nucleation and growth of CNTs [14], which mainly occurs on the Ni particle sites deposited over Al_2O_3 [51, 56]. Correspondingly, Ni on Al_2O_3 over 10Ni/20CZA produced the fine-scaled CNTs. That is, the limited Ni–CZ interaction over 10Ni/20CZA resulted in a more portion of Ni located on Al_2O_3 where the fine-scaled CNTs coke was grown. Specifically, the 20Ni/20CZA catalyst

contained large isolated Ni clusters on the CZ surface where coarse CNTs (diameter > 35 nm) were well grown, whereas fine-scale CNTs were developed over 10Ni/20CZA due to small Ni nanoparticles on Al₂O₃. On the large isolated Ni clusters with a lack of neighboring oxygen vacancies, the generation and delivery of O* to C* on Ni was not sufficiently fast compared with the formation rate of C*, resulting in the production of the coarse CNTs. In contrast, the highly dispersed Ni nanoparticles with a neighboring oxygen vacancies on CZ hardly produced the coke since C* on the Ni surface could be readily gasified via the reaction with O* delivered from the oxygen vacancies where O* was activated from steam. For the 20Ni/40CZA catalyst, the C* gasification is more competitive than the coke formation due to the unique properties of catalytic active sites, such as abundant oxygen vacancies and highly dispersed Ni nanoparticles, resulting in a low amount of coke over 20Ni/40CZA. We believe that, for 20Ni/40CZA, the abundant O* generated on CZ was efficiently and fast delivered to C* on Ni which was uniformly distributed over 40CZA, so that the C* gasification remained dominant on Ni over 40CZA. In other words, the sufficient delivery of O* onto C* on Ni over 40CZA accelerated the C* gasification. However, even for 20Ni/40CZA, there were Ni nanoparticles sitting on Al₂O₃ where CNTs-typed coke could be produced due to a lack of O*.



Scheme 3.2. Schematic illustration on coke formation and gasification over the xNi/yCZA catalysts at (a) 550 °C and (b) 350 °C.

The results obtained from the TGA/DTG profiles of the spent catalysts run at 350 °C were presented in **Table 3.4** and **Fig. 3.17**. Compared to the coke amounts observed at 550 °C, the spent xNi/40CZA catalyst exhibited higher coke amounts, which were similar to those for the spent xNi/20CZA catalyst. **Figure 3.17e** shows that the coke amounts generated by xNi/20CZA and xNi/40CZA remained similar under the reaction conditions of 350 °C.

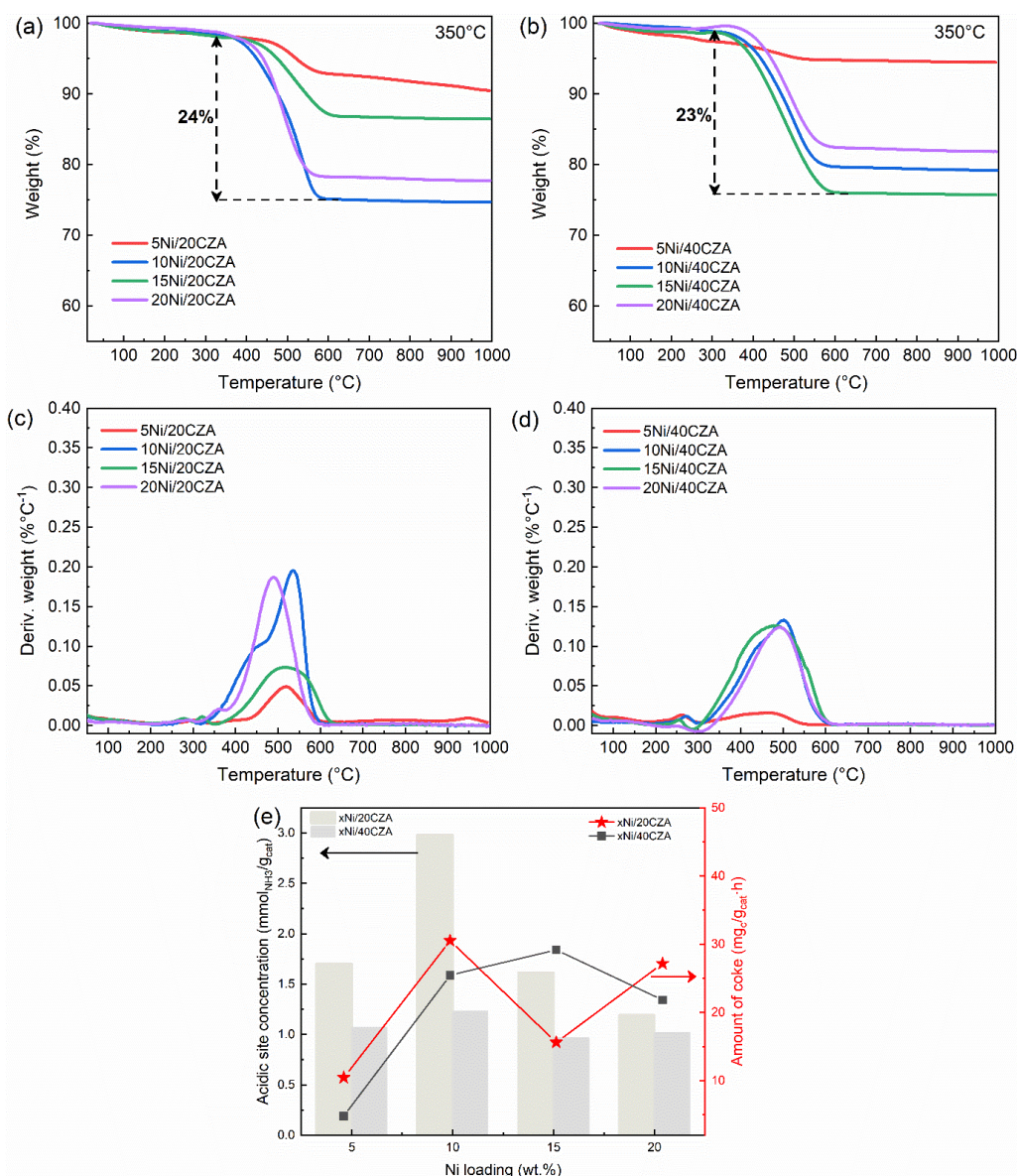


Figure 3.17. TGA/DTG profiles of spent catalysts (a, c) xNi/20CZA; (b, d) xNi/40CZA after 8 h ESR reaction at 350 °C, and (e) acidic site concentration of the catalysts and amount of coke after 8 h ESR reaction at 350 °C calculated by TGA results as a function of Ni loading amount.

Figures 3.17c and d show a broad temperature range of coke combustion for all the spent catalysts. The peak below 500 °C was assigned as a combustion of amorphous coke created by the C₂ polymerization on acidic sites over Al₂O₃. In addition, the peak over 500 °C was also ascribed to the filamentous coke. **Figure 3.17e** clearly exhibits the acidic sites on the catalysts played an important role in the formation of amorphous coke. Furthermore, the HR–

TEM analysis for the spent catalysts run at 350 °C (**Fig. 3.18**) revealed that for spent 20Ni/20CZA, a significant quantity of amorphous carbon, which was also identified by the coke combustion peak around 480 °C in the DTG profiles (**Fig. 3.17c**), was formed around the Ni nanoparticles, while CNTs-typed coke was formed for 10Ni/20CZA, 10Ni/40CZA, and 20Ni/40CZA. Surprisingly, the highly dispersed Ni and abundant oxygen vacancies in 20Ni/40CZA did not lead to a reduction in carbon content in the spent 20Ni/40CZA catalyst at 350 °C. This result is strongly related to the temperature dependent–coking behavior. At 350 °C, the Ni sites and oxygen vacancies over the xNi/yCZA catalysts were not essential to the coking behavior in ESR because the C2 polymerization on the acidic sites was dominant with a great production of amorphous coke and a small portion of filamentous coke (**Scheme 3.2b**).

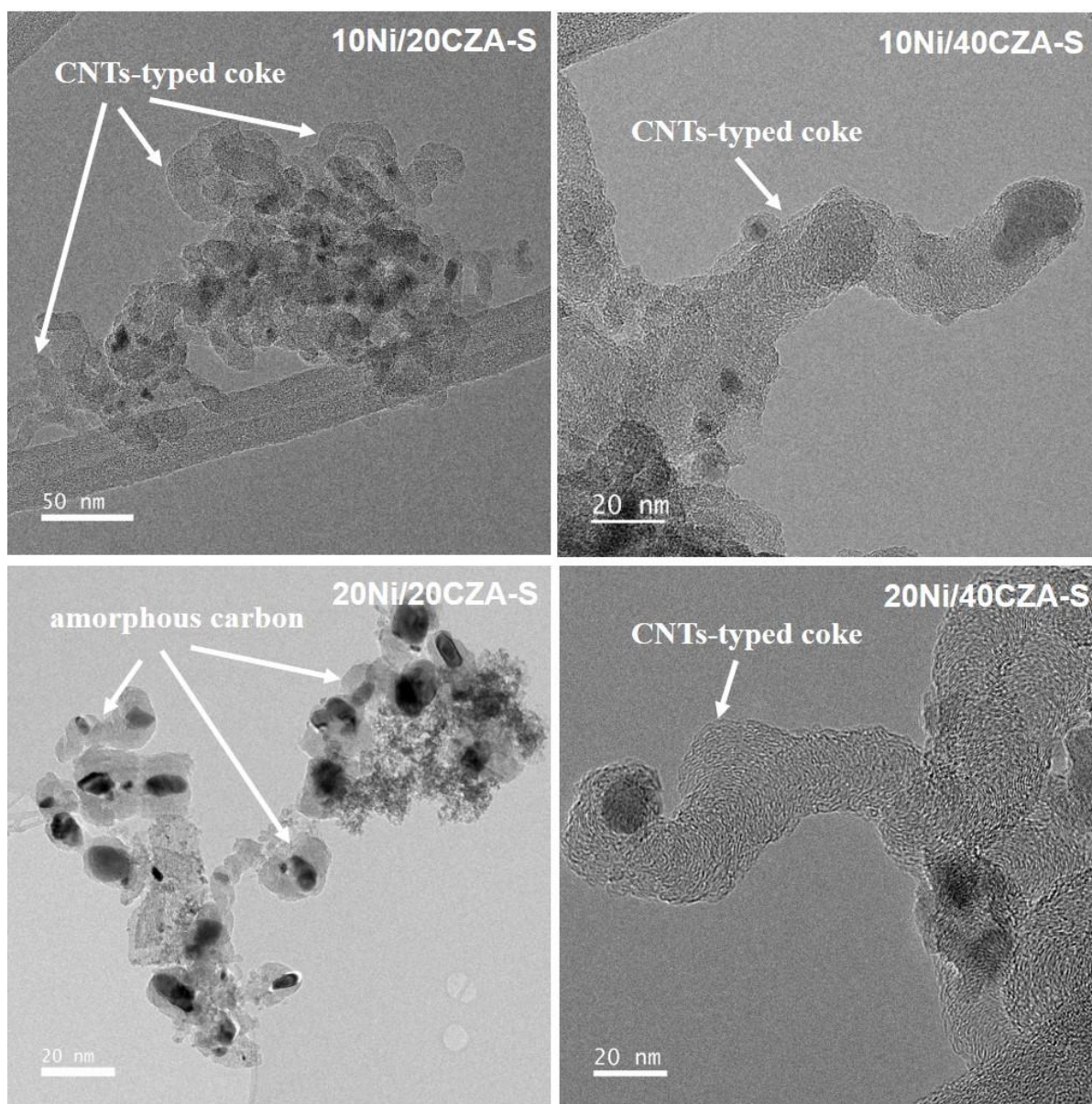


Figure 3.18. TEM images of the spent xNi/yCZA catalysts in ESR at 350 °C.

3.4. Conclusions

In this study, we synthesized Ni/CZA catalysts with different Ni loading contents and varied proportions of CZ to Al in the supports to investigate the optimization of metal-support interactions for ESR. We observed that 20Ni/20CZA contained large isolated Ni clusters over CZ with a lack of oxygen vacancies due to the limited Ni–CZ interaction over 20Ni/20CZA.

In contrast, the crystalline CZ structure in 40CZA induced a strong interaction with the Ni species, even at 20 wt% of Ni, resulting in highly dispersed Ni nanoparticles and abundant oxygen vacancies over 20Ni/40CZA. Accordingly, the optimized catalytic properties on active sites over 20Ni/40CZA produced the highest H₂ production rate and minimized the coke amount in ESR. Specifically, the excellent coking resistance of 20Ni/40CZA at 550 °C was ascribed to the generation of O* on abundant oxygen vacancies and the efficient delivery of O* from oxygen vacancies to C* on Ni over CZ, which resulted in faster gasification of C* than coking to CNTs.

PART III – ENHANCING ETHANOL STEAM REFORMING PERFORMANCE AND COKE GASIFICATION BY CATALYST SYNTHESIS METHOD OPTIMIZATION

Chapter 4. Metal–support interactions over Ni/CeO₂–ZrO₂ catalysts for ethanol steam reforming and their effects on the coke gasification.

4.1. Introduction

In steam reforming, Ni-supported catalysts are widely used because of their good ability for C–C bonding cleavage and acceptable cost for practical applications [10]. Even though various metal oxides have been employed as a support for Ni-supported catalysts in H₂ production, CeO₂–ZrO₂ is used as an additive or a support because of its high oxygen mobility, which plays an important role in steam reforming and decoking [77, 78]. Consequently, Ni/CeO₂–ZrO₂ (Ni/CZ) catalysts have been considered as a popular catalyst for steam reforming [54-56]. Even though enhancing the H₂ yield is the main direction for developing novel catalysts for ESR, the minimization of catalyst deactivation by the coke formation via the optimization of active sites over the catalysts is an existing issue in ESR research [14]. In our previous study, excessive Ni sites on Al₂O₃ using 20 wt.% Ni-loaded catalyst were suggested to enhance the coking routes during ESR, resulting in a high coke amount [54]. In addition, it was reported that the interaction between Ni and Ce_xZr_{1-x}O₂ influences the formation of oxygen vacancies and the corresponding catalytic behavior of Ni/Ce_xZr_{1-x}O₂ catalysts for ESR [55].

Recently, Anil et al. reviewed ESR for H₂ production using Ni/Al₂O₃- and Ni/CeO₂-based

catalysts [56]. They discussed the basic reaction mechanisms of ESR using Ni/Al₂O₃ and Ni/CeO₂ catalysts, which include coke generation and gasification. Coke is generated on an Ni surface via CH₄ decomposition during ESR. Ni active sites covered with accumulated coke can deactivate the catalyst. Meanwhile, coke is eliminated via coke gasification routes, where active oxygen (O*) reacts with the coke precursor (C*) through the Ni/CZ catalysts. During coke gasification, the main active sites, such as Ni and oxygen vacancies, over the Ni/CZ catalysts are involved in the activation of C* and O*, respectively. Therefore, these active sites obtained using the catalysts should be controlled via optimized metal–support interactions to maximize coke gasification, thereby addressing current issues of ESR. To the best of our knowledge, active sites optimized by the metal–support interactions due to Ni/CZ catalysts and their influence on the coking behavior and catalytic performance in ESR are yet to be studied.

In this work, we prepared Ni/CZ catalysts to investigate the metal–support interactions over the Ni/CZ catalysts and the corresponding coking behavior in ESR. Different Ni contents (5, 10, and 15 wt.%) were loaded onto the CZ support through two methods, namely one-pot (OP) and successive impregnation (IM) methods. Catalytic properties related to the active sites were characterized by different methods. ESR tests were conducted at 550°C. The spent catalysts were analyzed by thermogravimetric analysis (TGA) and X-ray diffraction (XRD) to understand the properties and processes of the coke. Based on the obtained results, the Ni/CZ catalysts prepared by the OP method had a higher Ni dispersion with abundant oxygen vacancies due to the strong Ni–CeO₂–ZrO₂ interaction, resulting in the efficient coke

gasification on the Ni surface.

4.2. Experimental

4.2.1. Catalyst preparation

Ni/CZ catalysts were synthesized by two catalyst preparation methods (OP and IM methods) using an aqueous solution of Ce and Zr precursors. $\text{Ce}(\text{NO}_3)_3 \cdot 6\text{H}_2\text{O}$ (99%; Sigma-Aldrich Korea, Gyeonggi, South Korea), $\text{ZrO}(\text{NO}_3)_2 \cdot x\text{H}_2\text{O}$ (99%; Sigma-Aldrich Korea, Gyeonggi, South Korea), and $\text{Ni}(\text{NO}_3)_2 \cdot 6\text{H}_2\text{O}$ (Sigma-Aldrich Korea, Gyeonggi, South Korea) were used as the precursors.

For the OP method, $\text{Ce}(\text{NO}_3)_3 \cdot 6\text{H}_2\text{O}$ and $\text{ZrO}(\text{NO}_3)_2 \cdot x\text{H}_2\text{O}$ salts were dissolved in a mixture of deionized water and pure ethanol. A solution of 2.6 g Pluronic P123 (PEG-PPG-PEG; Sigma-Aldrich Korea, Gyeonggi, South Korea) in pure ethanol was prepared. The dissolved $\text{Ni}(\text{NO}_3)_2 \cdot 6\text{H}_2\text{O}$ solution was added to the aforementioned Ce–Zr mixture and P123 solution to achieve Ni loadings of 5, 10, and 15 wt.% on the support. The salt solution with 13.5 g urea was mixed and transferred into a 200 mL Teflon-lined stainless-steel autoclave. The autoclave was then dried in an oven at 80°C for 5 h followed by drying at 120°C for 12 h. After naturally cooling to room temperature, the products were filtered, and washed with deionized water to obtain the precipitate, which was further dried at 70°C for 24 h. Subsequently, calcination was conducted in air at 600°C for 6 h, resulting in the formation of xNi/CZ–OP catalysts (x = 5, 10, 15 wt.%). Urea was used as the precipitator, and triblock copolymer Pluronic P123 was used for the porous structure.

For the IM method, $\text{Ce}(\text{NO}_3)_3 \cdot 6\text{H}_2\text{O}$ and $\text{ZrO}(\text{NO}_3)_2 \cdot x\text{H}_2\text{O}$ salts were completely

dissolved in deionized water under magnetic stirring. Subsequently, 2.6 g P123 was dissolved in pure ethanol. The salt solution, P123, and 13.5 g urea were mixed and transferred into a 200 mL Teflon-lined stainless-steel autoclave. Subsequently, calcination was performed, followed by the OP calcination step to obtain the calcined CeO₂–ZrO₂ support. xNi/CZ catalysts were synthesized by impregnating the aqueous solution using Ni(NO₃)₂·6H₂O to achieve Ni contents of 5, 10, and 15 wt.% on the support. The catalysts were then dried at room temperature for 24 h, followed by drying in an oven at 100°C for 12 h. The final step involved calcination in a furnace at 600°C for 6 h, yielding xNi/CZ–IM catalysts (x = 5, 10, and 15 wt.%). In all the catalysts, the Ce-to-Zr atomic ratio was maintained at 1.0. The Ni-based catalysts were reduced under an H₂ flow of 600°C for 2 h before the catalytic characterization tests, except for the H₂ temperature-programmed reduction (TPR) experiments.

4.2.2. Catalyst characterization

The Brunauer–Emmett–Teller (BET) surface area of the catalysts was determined using nitrogen adsorption/desorption curves recorded on an ASAP 2020 apparatus (Micromeritics, Norcross, GA, USA) at –196°C. Before the analysis, the samples were degassed at 200°C for 24 h in vacuum. H₂-TPR was performed in a multipurpose analytical system (BELCAT-M, MicrotracBEL Corp., Osaka, Japan) using a thermal conductivity detector. N₂ and mixture gases (5% H₂ in N₂) were used as the carrier and reducing gases, respectively. The temperature was increased from 50°C to 900°C at the ramping rate of 2°C/min. H₂

temperature-programmed desorption (H₂-TPD) experiments were conducted in a quartz flow reactor installed on the same system (BELCAT-M, MicrotracBEL Corp., Osaka, Japan). Before the adsorption measurements, the samples were reduced in situ under He with 5% H₂ at 600°C. After cooling the samples to 50°C, 5 vol.% H₂/N₂ (70 mL/min) was then pulsed on the catalyst until no further H₂ was consumed. The desorption was conducted at the temperature of 50°C to 900°C with the temperature increase of 1.5°C/min under N₂ flow.

The XRD patterns for the fresh and spent catalysts were obtained using a Rigaku RAD-3C diffractometer (Rigaku Corp., Tokyo, Japan) with Cu K_{α1} radiation ($\lambda = 1.5418 \text{ \AA}$) at a scattering angle (2θ) scan rate of 2°/min at 35 kV and 20 mA. The Scherrer equation was employed to calculate the crystallite sizes. High-resolution transmission electron microscopy (HRTEM) images were obtained using a JEOL JEM-2100F instrument (JEOL Ltd., Tokyo, Japan) to investigate the morphologies of the fresh and spent catalysts. Raman spectra were obtained with a DXR Raman microscope (Thermo Fisher Scientific, Waltham, MA, USA) using a 532-nm excitation source.

X-ray photoelectron spectroscopy (XPS) was conducted using the Thermo K-Alpha XPS with an aluminum K α X-ray source (Thermo Fisher Scientific, Waltham, MA, USA). The samples were collected using an X-ray spot size of 400 μm , pass energy of 80 eV, and energy step size of 0.1 eV. The charging effects were corrected by adjusting the binding energy of the C 1s peak from carbon contamination to 284.8 eV. The TGA of the spent catalysts was performed using a TGA Q50 apparatus (TA Instruments, New Castle, DE, USA). The experiments were performed under an air flow of 40 mL/min and N₂ flow of 60 mL/min at a

heating rate of 10°C/min and final temperature of 900°C. The amount of carbon deposition was calculated based on the mass loss profiles in the TGA test.

4.2.3. ESR reaction test

ESR was performed in a continuous flow fixed-bed quartz reactor under atmospheric pressure. First, 0.3 g catalyst was mixed with glass wool and placed in the middle of a quartz tube. Pure He (30 mL/min) was used as the carrier gas. The system was purged before the reduction step. All the calcined catalysts were reduced in situ under an H₂ flow of 6 mL/min and He flow of 30 mL/min at 600°C for 2 h before the reaction test. Water and ethanol were mixed at a fixed molar ratio of 6 (H₂O/C₂H₅OH = 6). Subsequently, the liquid mixture used as the reactant was continuously injected into the reactor using a high-performance liquid chromatography pump (PCS Pump SP-22-12S, FLOM/JAPAN, 0.01–2.00 mL/min, Tokyo, Japan). He was supplied into the reactor at 70 mL/min as the carrier gas during the reaction. The gas hourly space velocity (GHSV) was set to 10619 h⁻¹ for all the reaction tests. The inlet lines of the reactor were heated with a heating belt for a sufficient reactant vaporization. Before the gas phase product analysis, condensable vapors were trapped using a dry-ice condenser. During the reaction test, gas products were injected into a chromatographer (Acme 6000 GC, YL Instrument Co., Ltd., Anyang, South Korea) every 30 min using an online auto injection system and analyzed by a TCD connected with a Carboxen column. The liquid products collected from the condenser were analyzed by a chromatograph with a DB-WAX column and flame ionization detector. The ethanol conversion, H₂ selectivity, production rate,

and C-containing product selectivity were calculated as follows:

$$\text{Ethanol conversion (\%)} = \frac{n_{\text{EtOH}_{in}} - n_{\text{EtOH}_{out}}}{n_{\text{EtOH}_{in}}} \times 100,$$

$$\text{H}_2 \text{ selectivity (\%)} = \frac{n_{\text{H}_2}}{n_{\text{H}_2} + 2n_{\text{CH}_4} + 2n_{\text{C}_2\text{H}_4} + 3n_{\text{C}_2\text{H}_6}},$$

$$\text{H}_2 \text{ production rate } (\mu\text{mol}/(\text{g}_{\text{cat.}} \cdot \text{min})) = \frac{n_{\text{H}_2} \text{ per min.}}{\text{mass of catalysts}},$$

$$\text{C-containing product selectivity} = \frac{j \times n_i}{\sum j \times n_i},$$

where n_i is the number of moles in product i , and j is the number of carbon atoms in the C-containing product.

4.3. Results and discussion

4.3.1 Physicochemical properties of the Ni/CZ catalysts

The physicochemical properties of the $x\text{Ni}/\text{CZ}$ catalysts were investigated to understand the origin of their distinct ESR performances. As depicted in **Figs. 4.1 a** and **b**, all the samples exhibited type-IV (IUPAC) curves with hysteresis loops, indicating the mesoporous structure of the prepared catalysts [57].

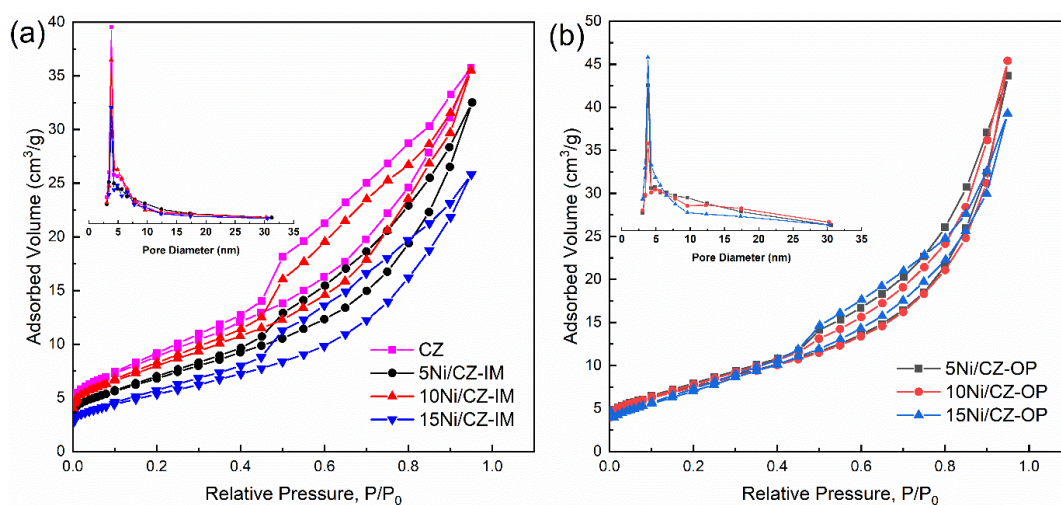


Figure 4.1. N_2 adsorption/desorption isotherms ($T=77\text{K}$) obtained over (a) $x\text{Ni}/\text{CZ-IM}$, and (b) $x\text{Ni}/\text{CZ-OP}$, and BJH pore size distribution of catalysts (insets).

The specific surface areas, mesopore volumes, and average pore sizes are compiled in **Table 4.1**. The specific surface areas of the catalysts are in the range of 24–36 m²/g without notable variations. **Fig. 4.1** illustrates the pore diameter distribution, revealing the relatively narrow and centered distribution in the range of 5–15 nm for xNi/CZ–IM, whereas that broader pore size distribution for xNi/CZ–OP. Smaller pore volumes are observed in the xNi/CZ–IM catalysts than that in the xNi/CZ–OP catalysts, which could be attributed to the obstruction of pores due to the large Ni species loaded into the pore channels [59].

Table 4.1. Physicochemical properties of the xNi/CZ catalysts.

Sample	BET Surface area (m ² /g)	Pore size (nm)	Pore volume (cm ³ /g)	CZ size (nm) ^(a)	Ni size (nm) ^(a)	Ni dispersion (%) ^(b)	Ni active site (mmol) ^(b)
CZ	36.45	3.8	0.054	41.6	n.a.	n.a.	n.a.
5Ni/CZ–IM	27.67	3.8	0.050	36.0	45.9	23.48	6.00
10Ni/CZ–IM	34.47	3.8	0.055	36.8	60.6	15.38	7.86
15Ni/CZ–IM	24.15	3.8	0.040	36.0	67.9	8.14	6.24
5NiCZ-OP	31.07	3.8	0.067	25.3	n.d. ^(c)	34.74	8.88
10NiCZ-OP	28.31	3.8	0.069	24.6	11.0	25.82	13.20
15NiCZ-OP	32.37	3.8	0.061	16.2	20.2	19.02	14.58

^a The values are obtained by the application of the Scherrer equation for characteristic XRD peaks of each crystallite.

^b The values are obtained from H₂-TPD.

^c The peak intensity of Ni in XRD pattern is too small to be detected.

Fig. 4.2a shows the wide-angle XRD patterns of the reduced materials. All the samples display diffraction peaks corresponding to Ni and CZ crystalline structures. The characteristic XRD peaks for CZ appeared at 25.8°, 33.1°, 47.5°, and 56.3°, corresponding to the (111), (200), (220), and (311) planes, respectively (JCPDS#34-0394). The XRD peak for the Ni (111) plane is detected at 2θ = 44.5° (JCPDS#04-0850). For 5Ni/CZ–IM, weak and broad diffraction peaks associated with the Ni phase are observed, indicating the formation of small

and dispersed Ni particles. As the Ni loading is increased to 10 and 15 wt.%, the intensity of the XRD peaks corresponding to the Ni phase for xNi/CZ–IM increased significantly. This suggests the formation of large isolated Ni nanoparticles, which limited the interaction with the CZ support. For xNi/CZ–OP, the two weak peaks at $2\theta = 44.5^\circ$ and 51.9° are ascribed to the Ni formation, indicating the good dispersion of Ni crystallites on the CZ support [79]. The average crystallite sizes of CZ and Ni were determined by the Scherrer equation using the CeO₂ (111) and Ni (111) peaks from the XRD patterns; the calculated values are presented in Table 1. The results confirm the smaller crystallites formed for both Ni and CZ in the xNi/CZ–OP catalysts than those in the xNi/CZ–IM catalysts, suggesting the strong interaction between Ni and CZ over xNi/CZ–OP, which prevents their agglomeration during pretreatment [80].

As the Ni loading was increased from 5 wt.% to 15 wt.% in xNi/CZ–OP, the CeO₂ (111) XRD peak shifted from the original position at $2\theta = 28.54^\circ$ to a higher diffraction angle at $2\theta = 28.64^\circ$. Moreover, an XRD peak at 30.11° , corresponding to the ZrO₂ phase, is noted with the increase in the Ni loading content in xNi/CZ–OP (**Fig. 4.2b**). This can be attributed to the insertion of Ni heterocations into the CZ network, where smaller Ni atoms substituted the Zr atoms, resulting in the segregated formation of ZrO₂ phase [25]. In contrast, the CeO₂ (111) phase in xNi/CZ–IM did not exhibit any shift in the peak position, indicating the absence of compositional changes with the variations in the Ni loading contents in xNi/CZ–IM.

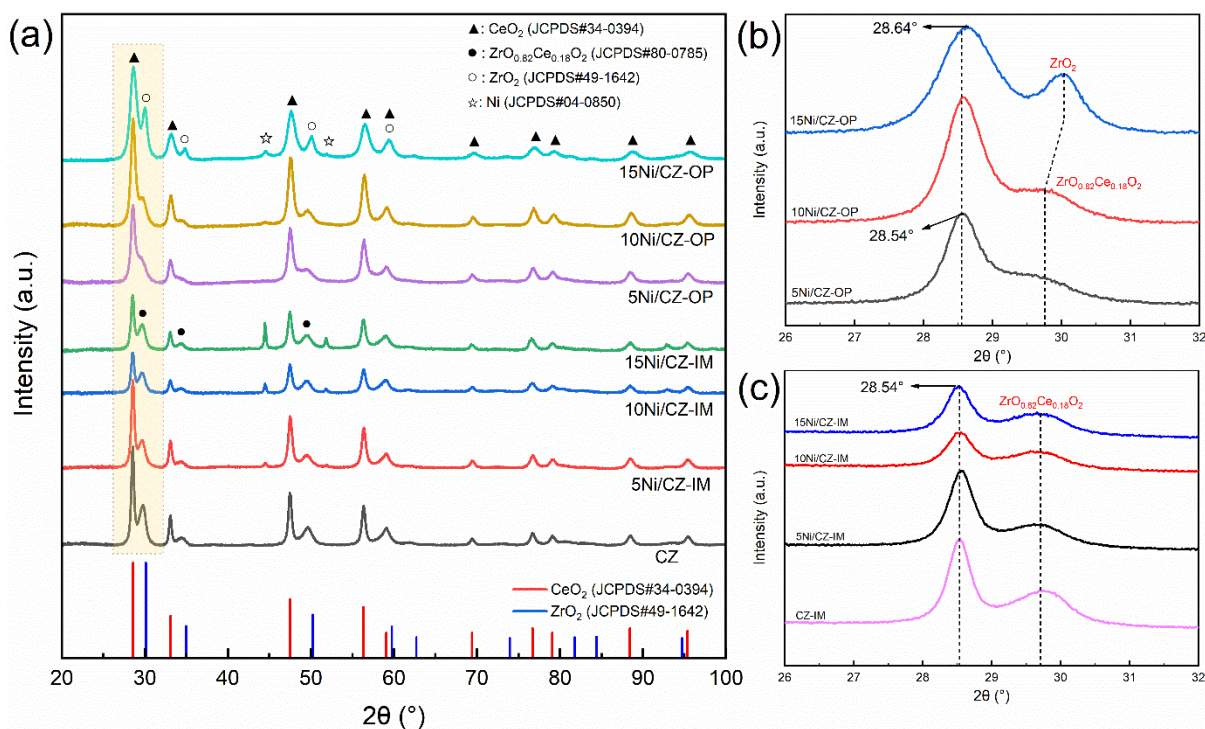


Figure 4.2. (a) XRD patterns of the reduced catalysts. (b, c) Enlarged XRD patterns of $x\text{Ni}/\text{CZ-OP}$ and $x\text{Ni}/\text{CZ-IM}$.

Fig. 4.3 shows the HRTEM images and EDS mapping of the $x\text{Ni}/\text{CZ-IM}$ and $x\text{Ni}/\text{CZ-OP}$ catalysts. From the results, the size of Ni nanoparticles for the $x\text{Ni}/\text{CZ-OP}$ catalysts is 2–13 nm, indicating the high Ni dispersion with small nanoparticle size due to the favorable interaction among Ni–Ce–Zr oxides. In contrast, isolated Ni nanoparticles with a larger size of 17–69 nm are observed in the $x\text{Ni}/\text{CZ-IM}$ catalysts, which is consistent with the results obtained from the XRD analyses.

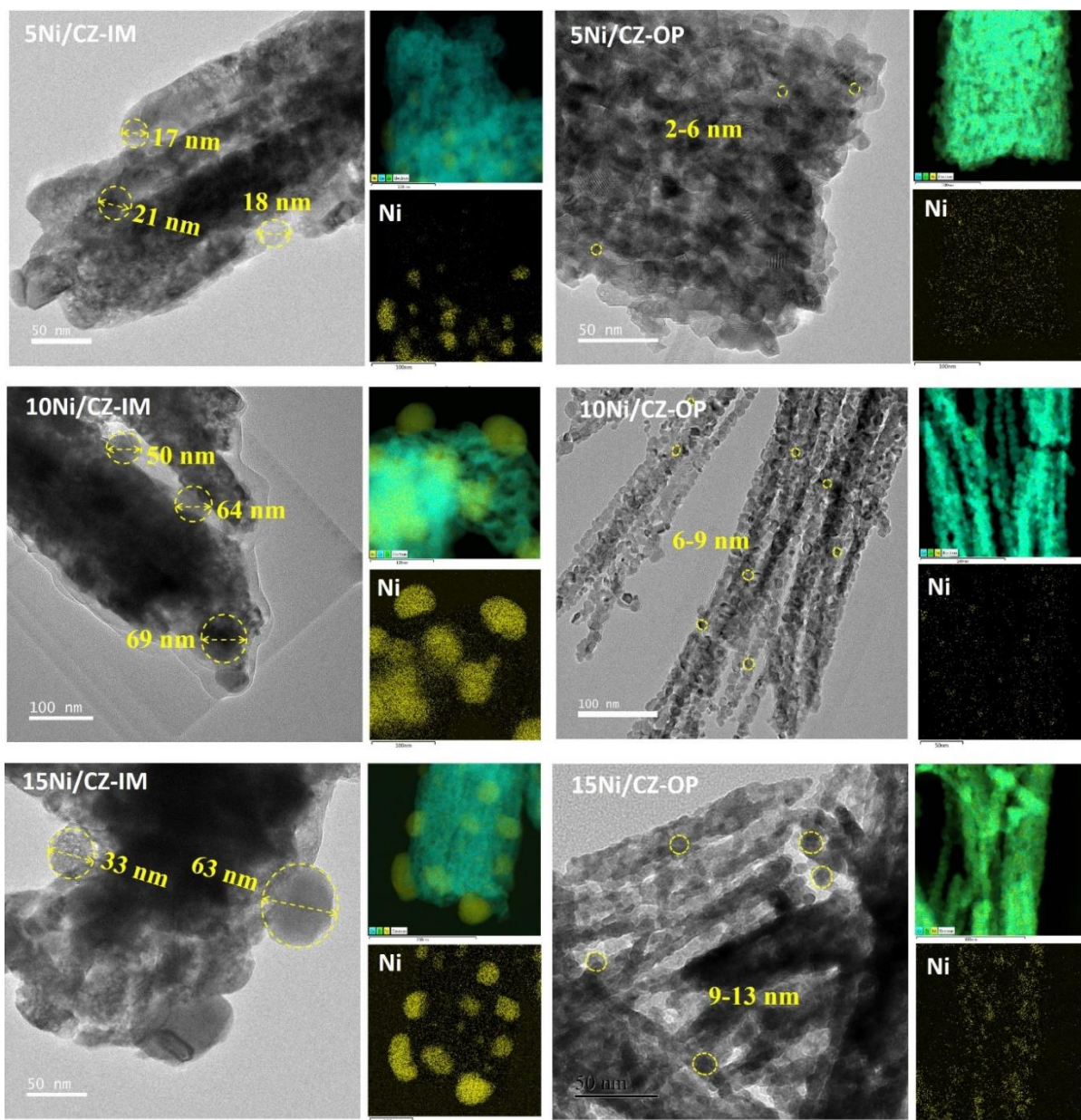


Figure 4.3. TEM images and EDS mapping of the prepared catalysts.

The Ni dispersion and active sites were determined by the H₂-TPD measurements (Fig. 4.4); the results are listed in Table 4.1. The 5Ni/CZ-OP catalyst demonstrated the highest Ni dispersion of 34.74%. With an increase in the Ni loading to 10 and 15 wt.%, the Ni dispersion slightly decreased to 25.82% and 19.02%, respectively, for the xNi/CZ-OP catalyst, and significantly decreased to 23.48% and 8.14%, respectively, for the xNi/CZ-OP catalysts.

Meanwhile, the number of Ni active sites increases with the Ni loading for the xNi/CZ–OP catalysts, thereby surpassing the values observed in the xNi/CZ–IM catalysts. This could be attributed to the increase in the Ni nanoparticle size from 45.9 nm to 67.9 nm with the increase in the Ni content of the xNi/CZ–IM catalysts. Consequently, the corresponding Ni dispersion decreases significantly, resulting in fewer Ni active sites. However, in the xNi/CZ–OP catalysts, the smaller Ni crystallites increases the Ni dispersion on the support surface. These findings correspond well with the results obtained from the XRD and HRTEM analyses, indicating the influence of the Ni–CZ interaction on the Ni nanoparticle size. For the xNi/CZ–OP catalysts, the small and uniformly distributed Ni nanoparticles can be embedded onto the CZ lattice with a strong interaction with the support, resulting in the formation of a Ni–CZ solid solution and increase in the active sites of the Ni species. In contrast, for the xNi/CZ–IM catalysts, larger Ni clusters are separated from the CZ support due the limited interaction between Ni and the CZ support.

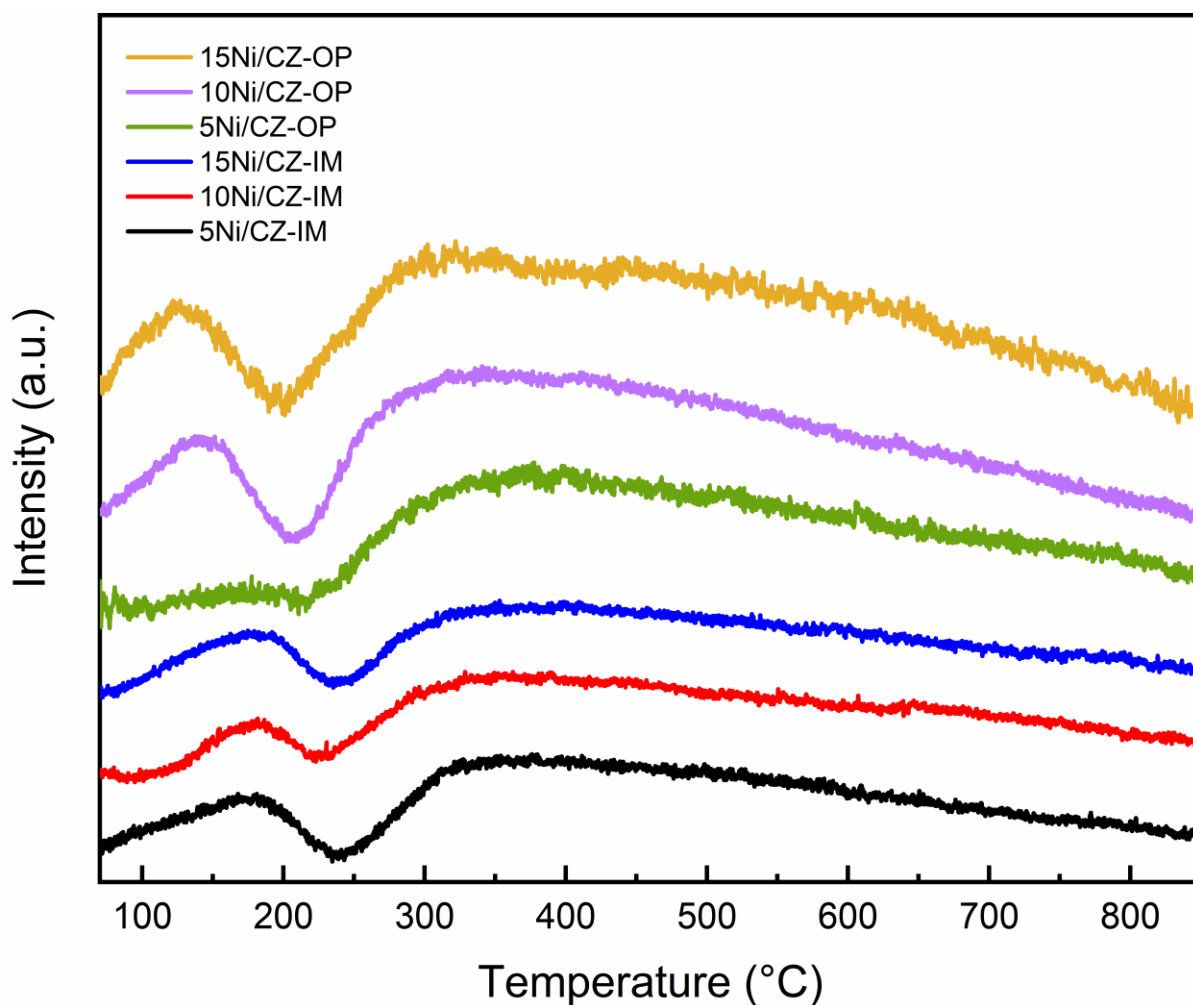


Figure 4.4. H₂-TPD profiles of the catalysts.

H₂-TPR experiments were performed to investigate the Ni–CZ interaction and reducibility of the Ni/CZ catalysts; the results are displayed in **Fig. 4.5**. All the samples have three main reduction peaks at 312°C (α peak), 354°C (β peak), and 406°C (γ peak). The α peak is assigned to the reduction of isolated NiO particles. The β peak corresponds to the reduction of dispersed NiO interacting with the CZ support without forming a chemical bond, whereas the γ peak is ascribed to the formation of the Ni–Ce–Ox solid solution [81, 82]. In addition, two additional peaks are observed at 215°C (δ) and 790°C (ϵ), which are attributed to the reduction of adsorbed oxygen species on the vacancy sites created by the incorporation

of Ni^{2+} to the ceria lattice and reduction of bulk CeO_2 , respectively [82, 83].

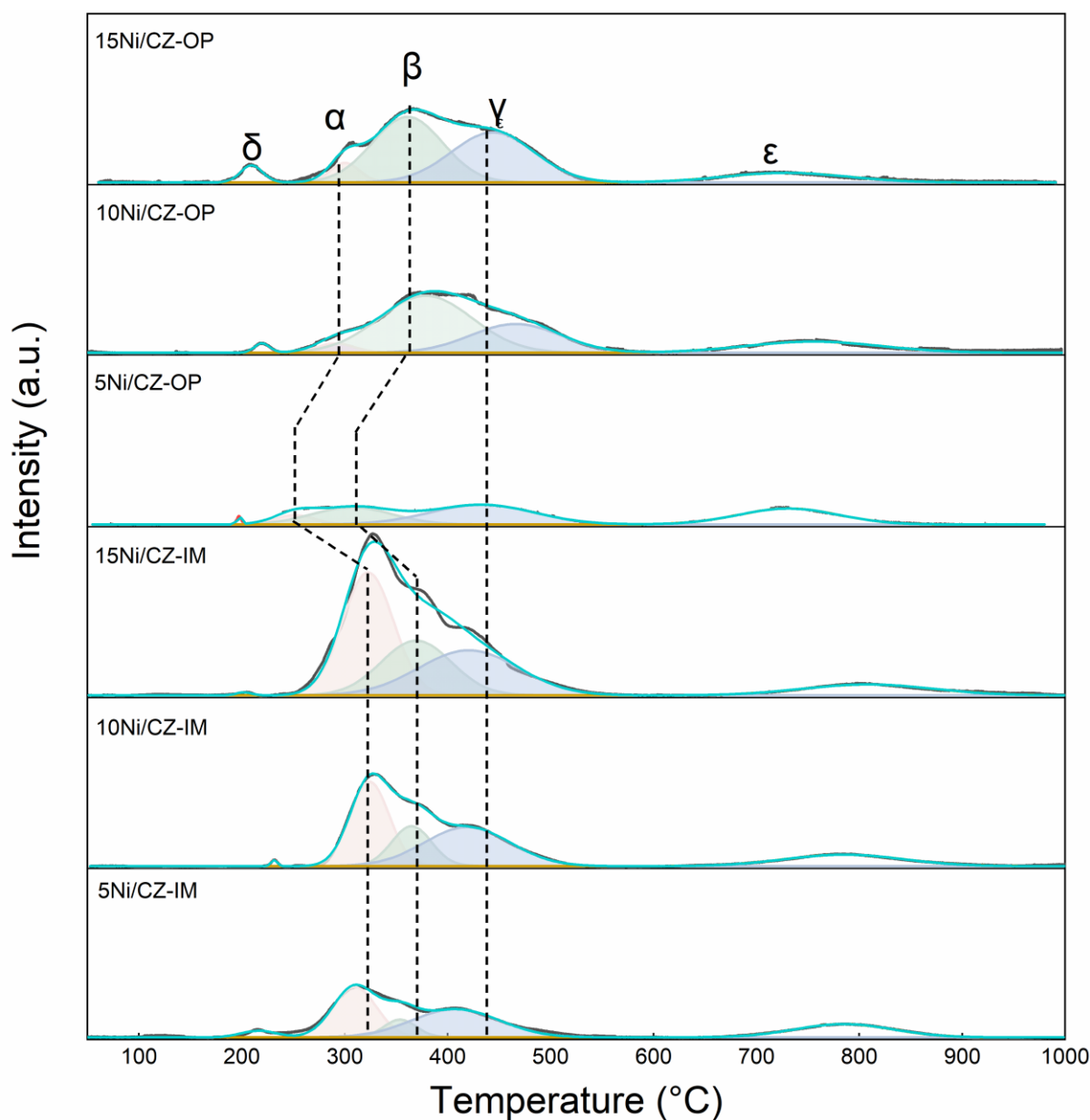


Figure 4.5. H_2 -TPR profiles of the catalysts (based on Table 4.2).

The quantitative analysis of H_2 consumption and corresponding deconvoluted peak areas are summarized in **Table 4.2**. H_2 consumption was estimated by integrating the H_2 -TPR profile. For the $x\text{Ni}/\text{CZ-IM}$ catalysts, the dominant reduction peak was the α peak corresponding to the formation of isolated large Ni nanoparticles, which weakened the

interaction between Ni and the support. In contrast, the β and γ peak areas in the xNi/CZ–OP catalysts are increased significantly with the increase in the Ni content up to 10 and 15 wt.%. Additionally, the xNi/CZ–OP catalysts display a higher number of oxygen vacancies than that of the xNi/CZ–IM catalysts, as demonstrated by the peak deconvolution (**Table 4.2**). Therefore, the xNi/CZ–OP catalysts exhibited a strong Ni–CZ interaction. In addition, the δ peak area increased from 0.66 to 3.47 as the Ni content increased in the xNi/CZ–OP catalysts. This further confirms the occurrence of a strong Ni–CZ interaction in the xNi/CZ–OP catalysts, thereby facilitating the formation of an Ni–CZ solid solution and generating more oxygen vacancies. Moreover, compared to the xNi/CZ–IM catalysts, the ϵ peak at 790°C shifted to a lower temperature of approximately 720°C in the xNi/CZ–OP catalysts. This indicates that the incorporation of Ni²⁺ into the ceria lattice of the xNi/CZ–OP catalysts resulted in the formation of Ni–Ce–O species and enhanced the lattice distortion of ceria [84, 85], thereby facilitating the reduction behavior of xNi/CZ–OP [86, 87].

Table 4.2. The H₂ consumption data and H₂-TPR peak areas of the catalysts

Sample	H ₂ consumption (mmol/g)	H ₂ -TPR peak area (*10 ⁶)/peak area percentage (%)				
		α	β	γ	δ	ϵ
5Ni/CZ-IM	0.453	59.9/32.36	15.7/8.49	67.5/36.48	6.39/3.45	35.6/19.22
10Ni/CZ-IM	0.651	90.5/34.12	43.6/16.46	92.2/34.77	1.09/0.41	37.8/14.24
15Ni/CZ-IM	0.846	171.0/38.88	105.9/24.04	123.4/28.02	1.25/0.28	38.7/8.78
5Ni/CZ-OP	0.565	9.98/6.72	37.5/25.22	56.5/38.00	0.98/0.66	43.7/29.41
10Ni/CZ-OP	0.688	9.56/3.52	145.5/53.65	71.0/26.17	3.86/1.42	41.3/15.23
15Ni/CZ-OP	0.747	15.8/5.27	126.6/42.25	114.3/38.14	10.41/3.47	32.5/10.86

Raman spectra were used to confirm the existence of oxygen vacancies and analyze structural properties of ceria nanomaterials based on their sensitivity to the Ce–O bond

vibration and lattice defects [68]. As shown in **Fig. 4.6**, the spectra exhibits a main band at 465 cm^{-1} , which is assigned to the F_{2g} fluorite structure vibration (Ce–O). A broad peak at 600 cm^{-1} corresponds to the defect band related to the oxygen vacancies in the ceria lattice (Ce–V) [25, 70]. The relative intensity ratios of the peaks ($I_{\text{Ce-V/Ce-O}}$) for all the catalysts were calculated; the results are shown in **Fig. 4.6**. The $I_{\text{Ce-V/Ce-O}}$ ratios for the xNi/CZ–OP catalysts are higher than those of the xNi/CZ–IM catalysts, indicating the greater abundance of oxygen vacancies in the former than that in the latter. Moreover, the $I_{\text{Ce-V/Ce-O}}$ ratio for xNi/CZ–OP continuously increases with the Ni loading content with the highest value of 0.39 obtained for 15Ni/CZ–OP. This further confirms the efficient formation of oxygen vacancies in the CZ lattice by the strong Ni–CZ interaction in the xNi/CZ–OP catalysts. However, $I_{\text{Ce-V/Ce-O}}$ decreases from 0.34 to 0.20 for the xNi/CZ–IM catalysts, implying that the Ni–CZ interaction is limited by the presence of isolated Ni nanoparticles. Therefore, lattice defects could be effectively generated through a combination of highly dispersed Ni and strong Ni–CZ interaction.

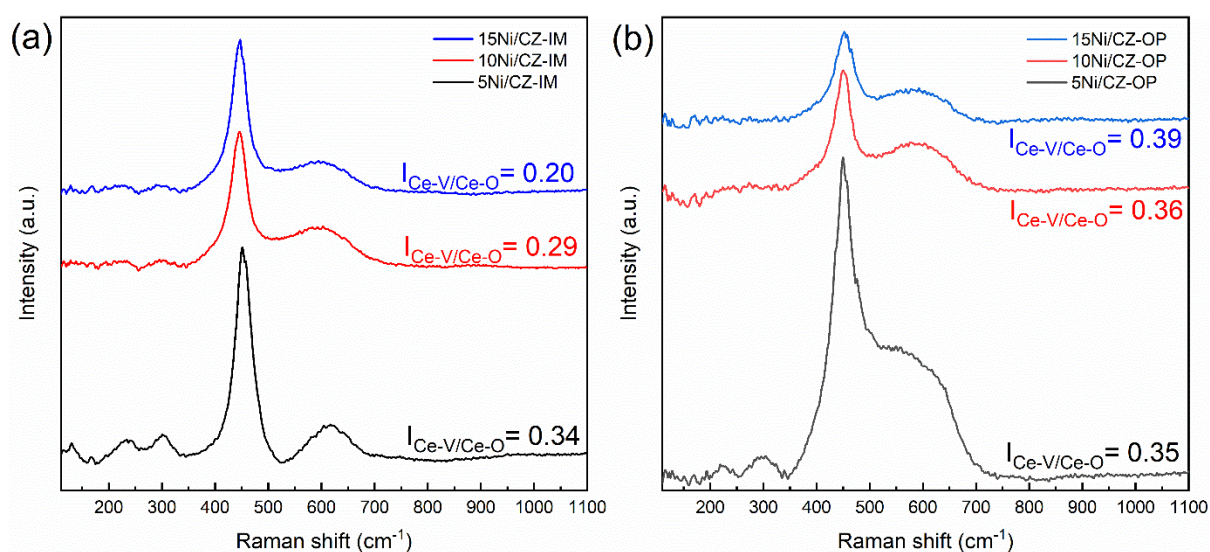


Figure 4.6. Raman spectra of the (b) xNi/CZ–OP and (c) xNi/CZ–IM catalysts.

XPS was also employed to clarify the surface chemical environment on the reduced catalysts. The XPS data of Ni 2p and Ce 3d are shown in **Figs. 4.7** and **Fig. 4.8**, respectively.

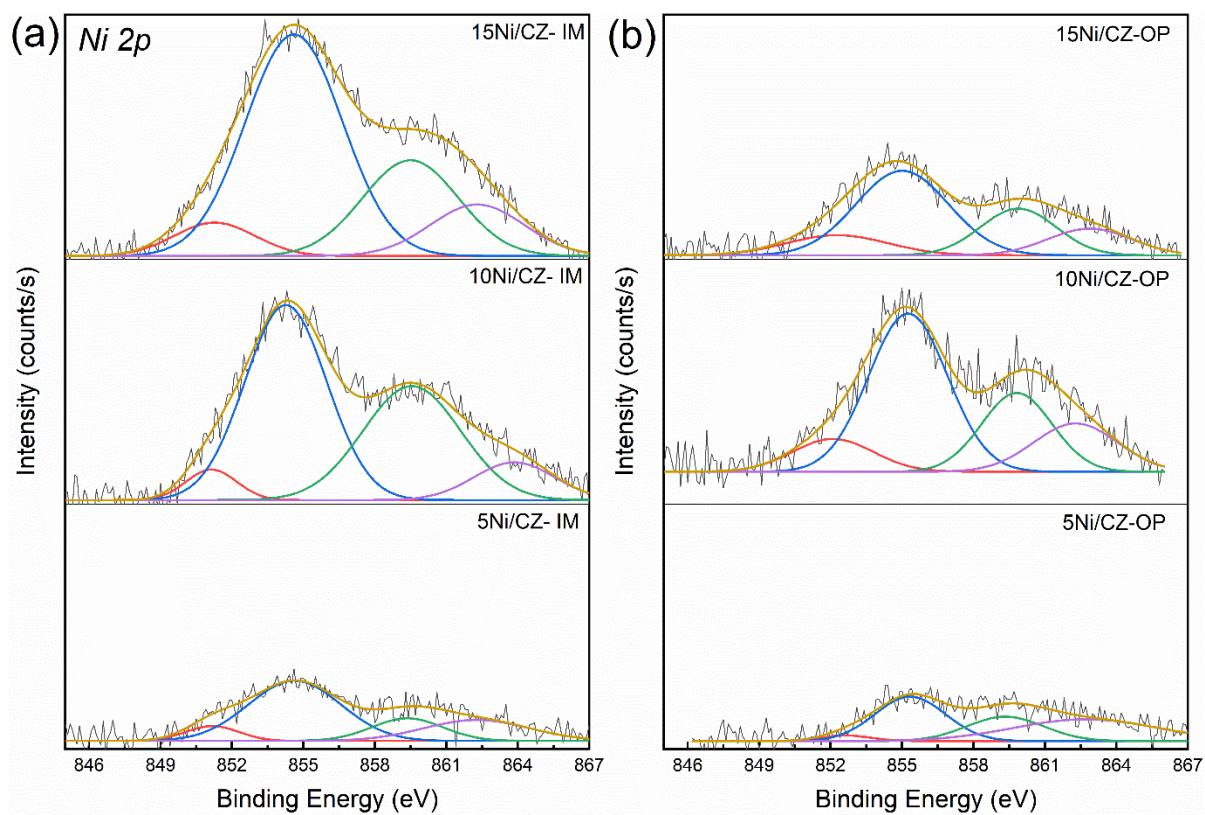


Figure 4.7. XPS data of Ni 2p for the reduced catalysts.

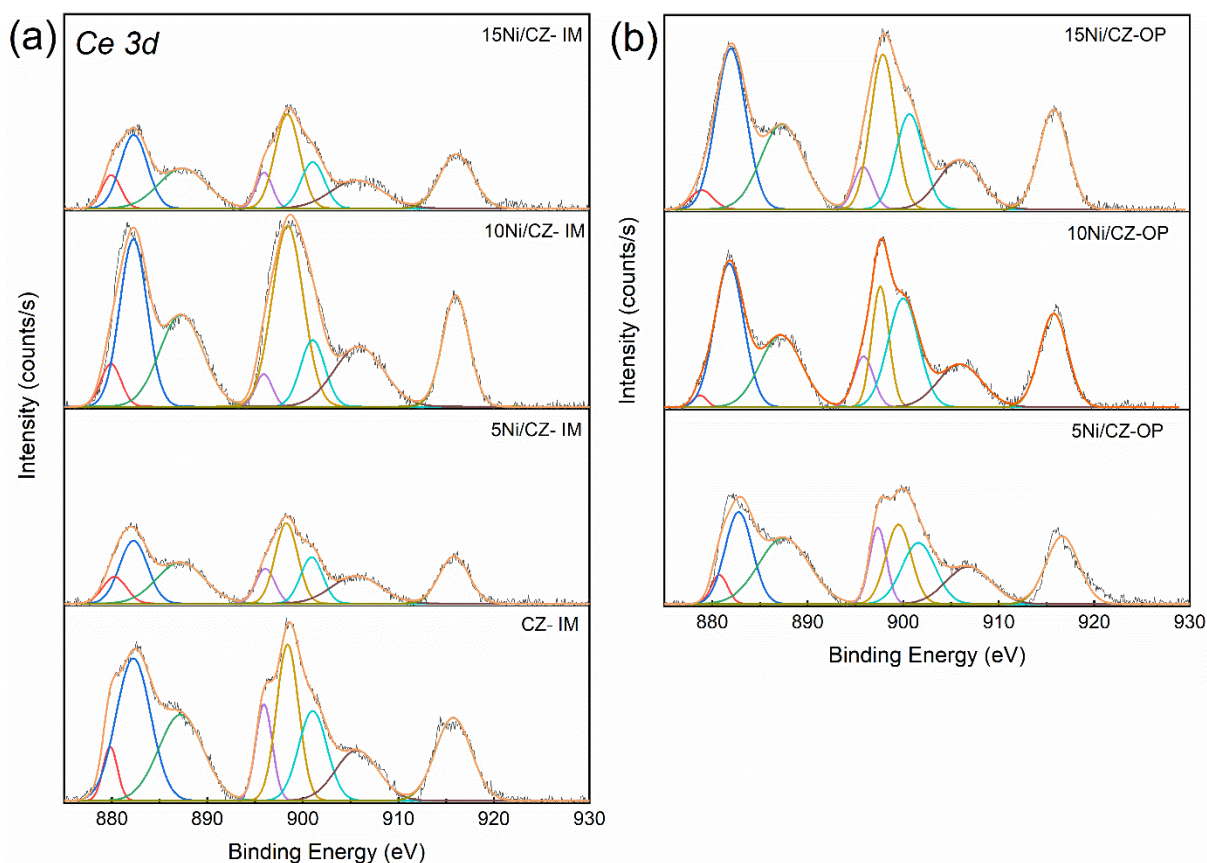


Figure 4.8. XPS data of Ce 3d for the (b) xNi/CZ–OP and (c) xNi/CZ–IM catalysts.

As shown in **Fig. 4.7**, there are four deconvoluted peaks at approximately 852.2, 855.0, 859.9, and 862.8 eV, which are assigned to Ni^0 , Ni^{2+} , and two satellite peaks of Ni $2p_{3/2}$, respectively [60, 88]. According to previous reports [12, 89], metallic Ni on the catalyst surface provides numerous active sites for the cleavage of C–C and C–H bonds in ethanol; thus, the Ni metal content is an important indicator of the catalyst performance in ESR. **Table 4.3** shows the calculated Ni^0 and Ni^{2+} content from the peak areas obtained through the deconvolution of the Ni 2p XPS data. For the xNi/CZ–OP catalysts, the Ni^0 content significantly increases from 8.44% to 20.68% with the Ni loading content, indicating the higher distribution and smaller size of Ni particles for 15Ni/CZ–OP [90, 91]. Conversely, no

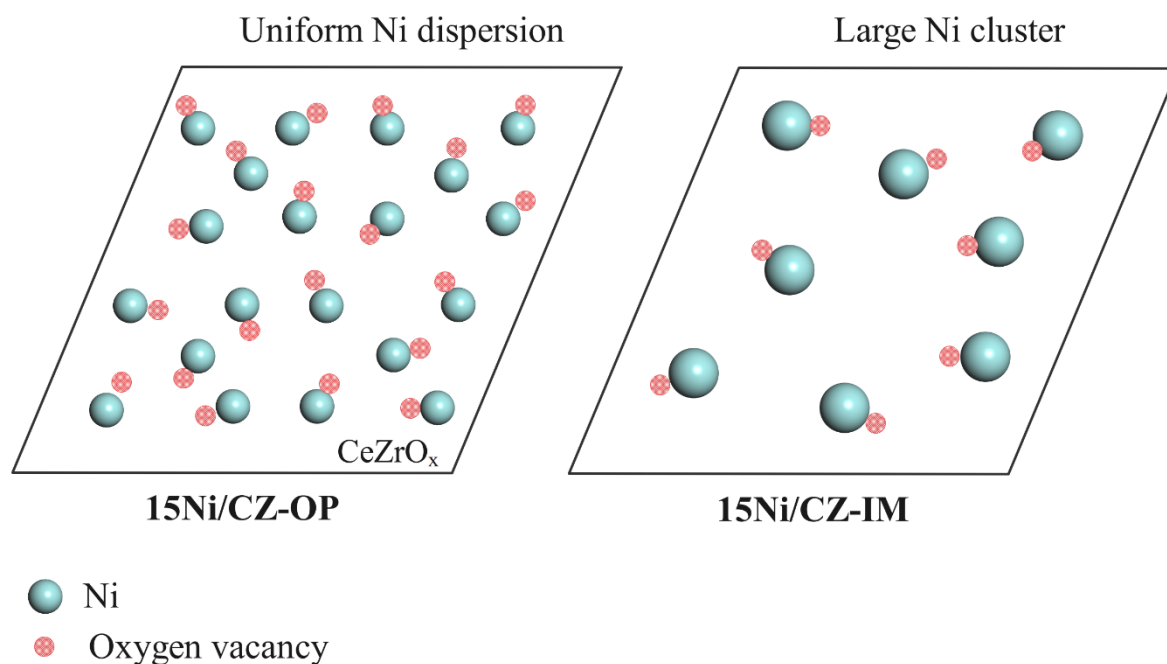
substantial change is noted for the Ni⁰ content of the xNi/CZ–IM catalysts, which is maintained in the range of 8.78%–12.53%. The Ce 3d spectra show the same trend as the Ni 2p spectra. **Fig. 4.8** depicts the Ce 3d spectra with the presence of eight peaks fitted to the Ce⁴⁺ and Ce³⁺ components. The percentages of Ce³⁺ in the xNi/CZ–OP catalysts remained consistently high in the range of 25–26%. In contrast, the Ce³⁺ content in the 10Ni/CZ–IM and 15Ni/CZ–IM are significantly lower at 13.06% and 14.44%, respectively (**Table 4.3**). The presence of uniformly distributed Ni nanoparticles in the xNi/CZ–OP catalysts is ascribed to the strong interaction between Ni and the support. This interaction promotes the incorporation of Ni into the CZ lattice, thereby generating more oxygen vacancies. However, the xNi/CZ–IM catalysts have low concentration of oxygen vacancies because of the presence of isolated Ni clusters, which hinder the interaction between Ni and CZ.

Table 4.3. The quantification of Ni metal, Ni²⁺, and Ce³⁺ contents from the XPS results.

Sample	Ni metal %	Ni ²⁺ %	Ce ³⁺ %
CZ	n.a.	n.a.	22.18
5Ni/CZ-IM	12.53	87.47	21.88
10Ni/CZ-IM	8.78	91.22	13.06
15Ni/CZ-IM	11.11	88.89	14.44
5Ni/CZ-OP	8.44	91.56	24.45
10Ni/CZ-OP	17.51	82.49	24.61
15Ni/CZ-OP	20.68	79.32	25.93

Scheme 4.1 illustrates the active sites over the xNi/CZ–OP and xNi/CZ–IM catalysts. In the IM method, the Ni precursor was added into the CZ support after the formation of the CZ crystalline structure, which limited the interaction between Ni and the CZ support. Consequently, isolated Ni clusters and limited oxygen vacancies were formed over xNi/CZ–

IM. In contrast, the strong Ni–CZ interaction over xNi/CZ–OP resulted in the uniform distribution of small Ni nanoparticles with abundant oxygen vacancies even at the high Ni loading contents. The OP method could promote the Ni–CZ interaction during the loading of precursors into the Teflon-lined stainless-steel autoclave before calcination. The calcination for xNi/CZ–OP resulted in the efficient formation of Ni–Ce–O_x species and NiO interactions with CZ at a high Ni content, resulting in a uniform Ni distribution with abundant oxygen vacancies after the reduction step.



Scheme 4.1. Illustration of the active sites over the Ni/CZ catalysts.

4.3.2 Catalytic performance of ESR

The ESR reaction test was mainly conducted at 550°C for 8 h to evaluate the steam-reforming ability of the catalysts and gain insights in the properties and processes of coke. During the reaction tests, hydrocarbon intermediates, such as CH₄, ethylene, and a trace

amount of ethane, were detected in the gas phase along with CO, CO₂, and H₂ (**Table 4.4**).

Table 4.4. Results of the ESR of the xNi/CZ catalysts at 550°C for 8 h.

Samples	C ₂ H ₅ OH conversion (%)	C-containing gas products selectivity (%)					C ₃ H ₆ O	CH ₃ CHO	H ₂ selectivity (%)	H ₂ production rate (μmol/g _{cat} ·min)	Amount of coke (mgc/gcat·h)
		CO	CO ₂	CH ₄	C ₂ H ₄	C ₂ H ₆					
CZ	99.89	3.09	19.35	15.79	46.41	5.37	0.01	9.97	31.11	493.6	0.35
5Ni/CZ-IM	96.55	26.90	59.30	12.38	0.00	0.00	0.60	0.81	74.74	690.3	3.17
10Ni/CZ-IM	90.82	21.32	61.56	15.80	0.00	0.00	0.57	0.75	72.31	707.4	12.86
15Ni/CZ-IM	97.86	24.47	58.43	13.87	2.96	0.00	0.18	0.08	75.74	613.0	32.92
5Ni/CZ-OP	100.00	23.13	64.88	11.98	0.00	0.00	0.00	0.01	76.45	674.1	2.10
10Ni/CZ-OP	99.41	23.91	62.20	13.65	0.00	0.00	0.13	0.12	74.59	749.3	-0.52
15Ni/CZ-OP	100.00	19.88	63.37	16.74	0.00	0.00	0.00	0.00	69.07	715.0	1.86

The liquid products collected with a condenser were analyzed to measure the unreacted ethanol, acetone, and acetaldehyde. **Fig. 4.9** shows a plot of the 8 h-on-stream results at 550°C for 5Ni/CZ-IM. Ethanol conversion, selectivity of carbon-containing gas products, liquid products selectivity, H₂ selectivity, and H₂ production rates were calculated based on the average values of the 8 h-on-stream reaction data. The calculated values are listed in

Table 4.4.

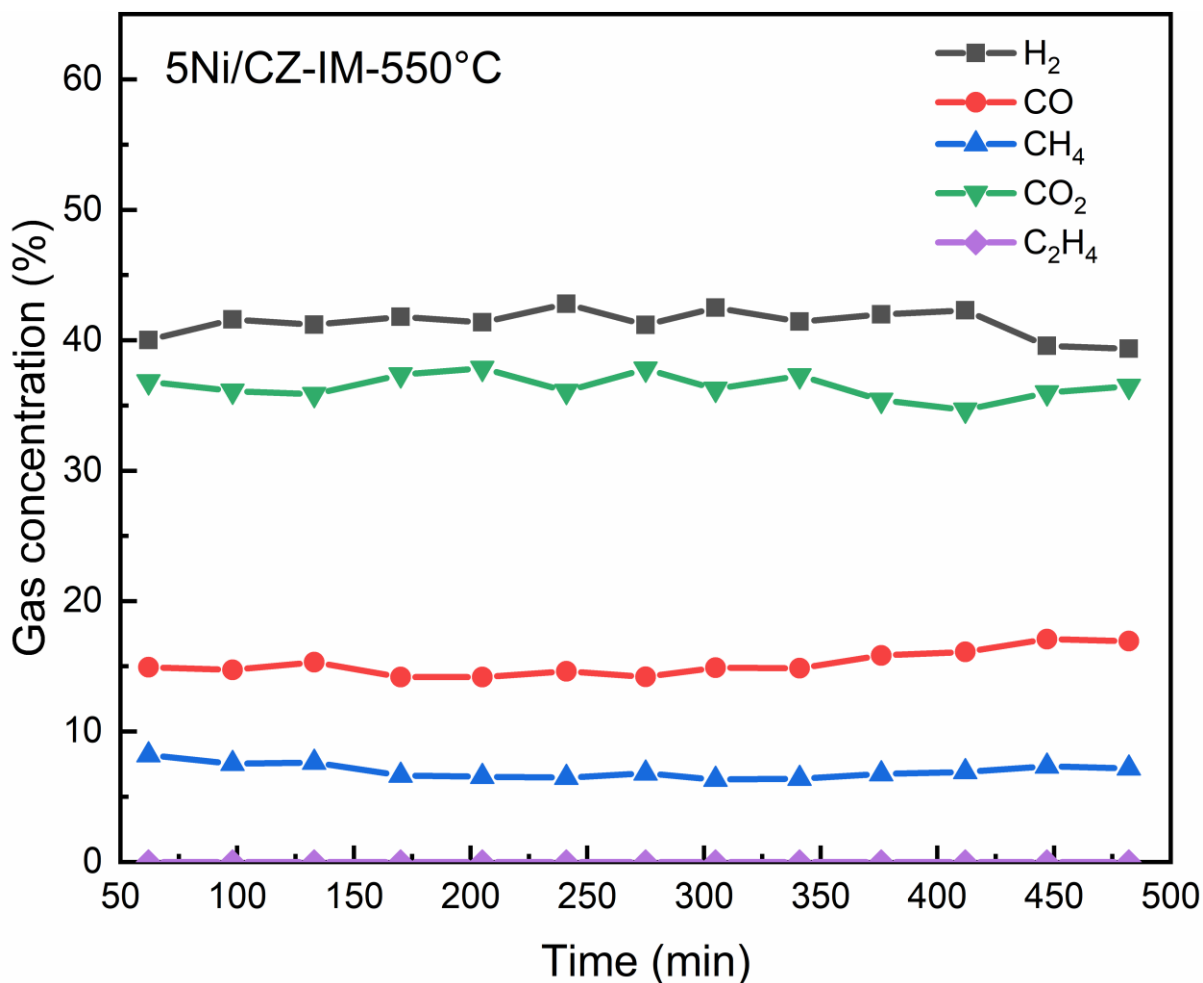


Figure 4.9. Gas production concentrations for the 5Ni/CZ-IM catalyst obtained from the 8 h ESR.

At the reaction temperature of 550°C, the xNi/CZ-IM catalysts achieved an ethanol conversion of over 90%, that is, 96.55%, 90.82%, and 97.86% for 5Ni/CZ-IM, 10Ni/CZ-IM, and 15Ni/CZ-IM catalysts, respectively. All xNi/CZ-OP catalysts achieved 100% ethanol conversion, and the selectivity of carbon-containing gases in these catalysts remained relatively unchanged (**Figs. 4.10a, c**). This indicates that the ESR reaction at 550°C almost reached a thermodynamic equilibrium. Furthermore, the liquid products formed in the xNi/CZ-OP catalysts were negligible, whereas the selectivity of the liquid products in the xNi/CZ-IM catalysts was higher (**Figs. 4.10b, c**). This suggests the better reforming ability of

the xNi/CZ–OP catalysts with more Ni metallic active sites, which is attributed to the superior capability of the Ni metal phase to activate C–H and C–C bonds in hydrocarbon molecules [42].

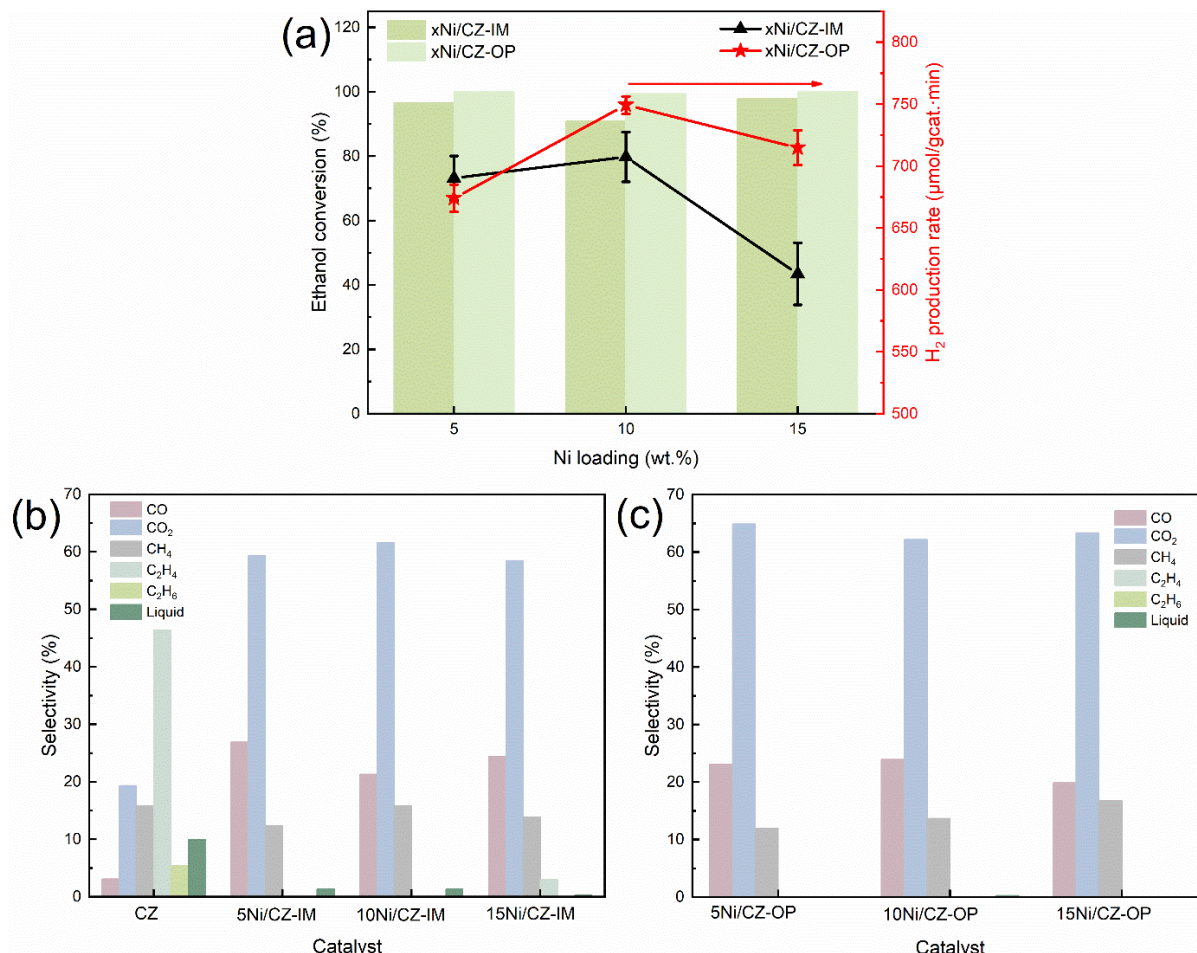


Figure 4.10. (a) Conversion of ethanol and average H₂ production rate, and (b, c) carbon-containing product selectivity of the xNi/CZ–IM and xNi/CZ–OP catalysts (Reaction conditions: S/C = 3, T = 550°C, GHSV = 10619 h⁻¹).

Fig. 4.10a shows the H₂ production rates of the catalysts. The H₂ production rates of 10Ni/CZ–IM and 15Ni/CZ–IM catalysts dropped from 707 μmol/g_{cat}·min to 613 μmol/g_{cat}·min, whereas that of the 10Ni/CZ–OP and 15Ni/CZ–OP catalysts remained high at

749 and 715 $\mu\text{mol}/\text{g}_{\text{cat}}\cdot\text{min}$, respectively. Notably, the coke behavior differed significantly between the xNi/CZ-IM and xNi/CZ-OP catalysts. **Table 4.4** presents the amount of coke formed during the reaction. The amounts of coke formed for 10Ni/CZ-IM and 15Ni/CZ-IM are 12.86 and 32.92 $\text{mgc}/\text{gcat}\cdot\text{h}$, respectively, which are considerably higher than those for the other catalysts (0.35–3.17 $\text{mgc}/\text{gcat}\cdot\text{h}$). In particular, a small amount of coke is formed over the xNi/CZ-OP catalysts.

The TGA and XRD results of the spent catalysts confirmed the different coke behaviors. The weight loss observed in the TGA profiles is primarily attributed to the oxidation of carbon species deposited on the spent catalysts during the ESR test at 550°C for 8 h. The TGA profiles (**Fig. 4.11**) can be divided into three regions to analyze the weight loss phenomena. At temperatures below 200°C, the weight loss is ascribed to the moisture removal and volatile impurity [46]. At 200–450°C, the weight increase is proportional to the Ni contents for the Ni-containing catalysts. In addition, the Ni metallic sites in the catalysts are transformed into the NiO phase under air flow, thereby increasing the catalyst weight [47]. At 450–600°C, the weight loss is ascribed to the coke combustion. The weight of 10Ni/CZ-IM and 15Ni/CZ-IM sharply drops with the significant coke formation. Meanwhile, xNi/CZ-OP exhibited the lowest weight loss, indicating its good resistance against coke formation because of the highly dispersed Ni particles and formation of abundant oxygen vacancies [49].

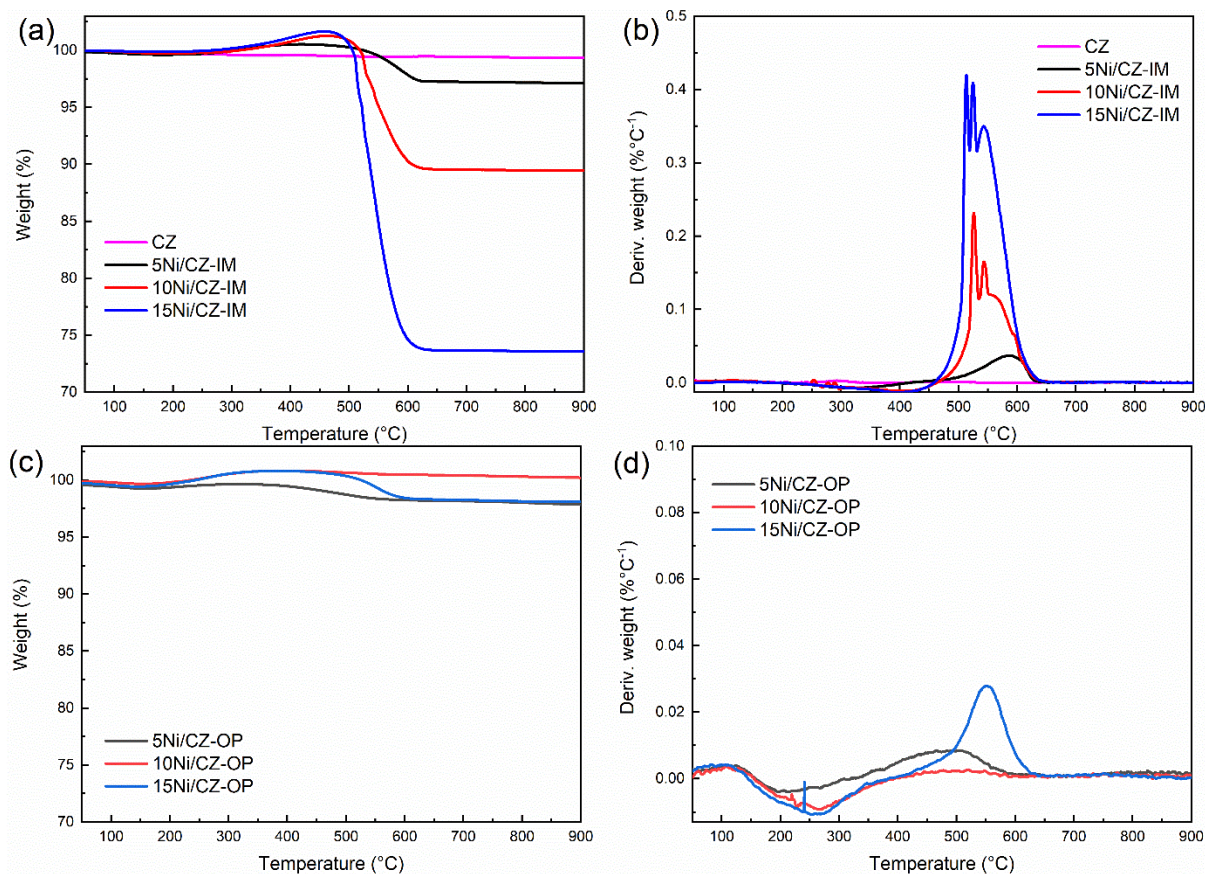


Figure 4.11. TGA/DTG profiles of the spent catalysts after the 8-h ESR at 550°C: (a, c) xNi/CZ–IM and (b, d) xNi/CZ–OP.

Fig. 4.12 illustrates the XRD patterns of the spent catalysts, whereby the characteristic XRD peaks are almost identical to those of the fresh catalysts, except for the appearance of a new peak at $2\theta = 26.1^\circ$ for the spent 15Ni/CZ–IM catalyst. This newly detected XRD peak at 26.1° is assigned to a coke phase [50], indicating the significant carbon deposition on the 15Ni/CZ–IM catalyst during the ESR tests, which is consistent with the TGA data obtained in this study.

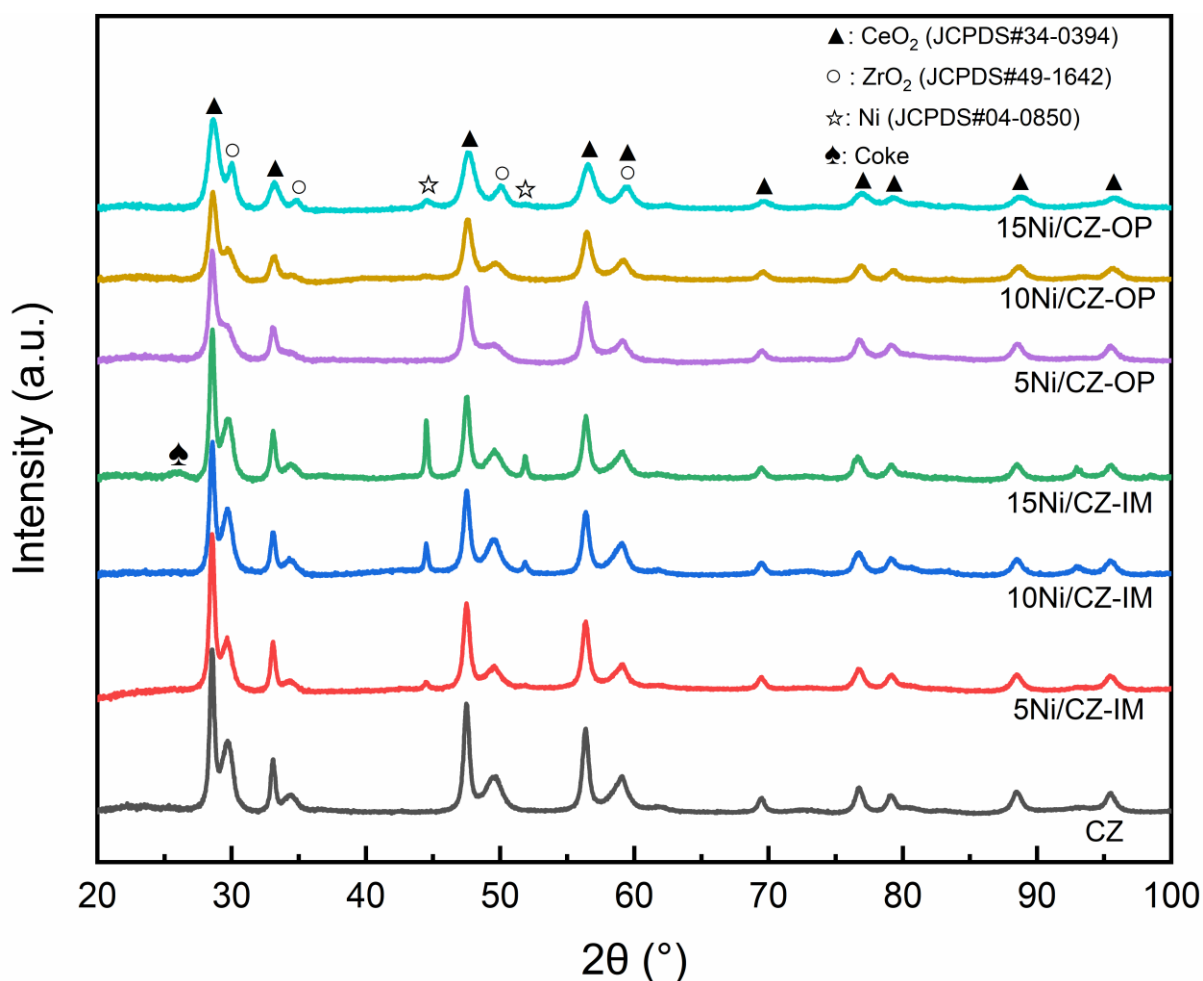


Figure 4.12. XRD patterns of the spent catalysts after the 8-h ESR at 550°C.

To further investigate the coking behavior of the catalysts, we selected 15Ni/CZ-IM and 15Ni/CZ-OP for a 30-h ESR reaction test. The results are summarized in **Table 4.5**. It was observed that the coke amount on the 15Ni/CZ-IM catalyst significantly increased to 62.66 mgc/gcat·h. Meanwhile, coke formation is not observed in the 15Ni/CZ-OP catalyst even after the 30-h reaction. Furthermore, the ethanol conversion for 15Ni/CZ-IM dropped notably to 57.21%, whereas that of 15Ni/CZ-OP is maintained at approximately 100%. Moreover, both catalysts exhibit a substantial difference in their H₂ production rate with values of 618.37 and 963.47 μmol/gcat·min for 15Ni/CZ-IM and 15Ni/CZ-OP, respectively.

Table 4.5. Results of the ESR of the xNi/CZ catalysts at 550°C for 30 h.

Samples	C ₂ H ₅ OH conversion (%)	C-containing gas products selectivity (%)					C ₃ H ₆ O	CH ₃ CHO	H ₂ selectivity (%)	H ₂ production rate (μmol/g _{cat} ·min)	Amount of coke (mgc/gcat.h)
		CO	CO ₂	CH ₄	C ₂ H ₄	C ₂ H ₆					
15Ni/CZ-IM	57.21	17.48	65.19	13.09	0.0	0.0	0.13	4.11	71.09	618.37	62.66
15Ni/CZ-OP	99.99	17.27	69.54	13.18	0.0	0.0	0.0	0.0	74.85	836.47	1.43

Fig. 4.13 presents the TGA and XRD patterns of the spent catalysts after the 30-h ESR reaction. The 15Ni/CZ-IM catalyst exhibits a weight loss of 51.1% with a significantly enhanced coke peak intensity in its XRD pattern. These results indicate that the carbon content on the xNi/CZ-IM catalyst increases with the reaction time. However, the TGA and XRD results do not demonstrate a carbon deposition on the 15Ni/CZ-OP catalyst, suggesting that it maintains a strong resistance against carbon deposition during long-term reactions.

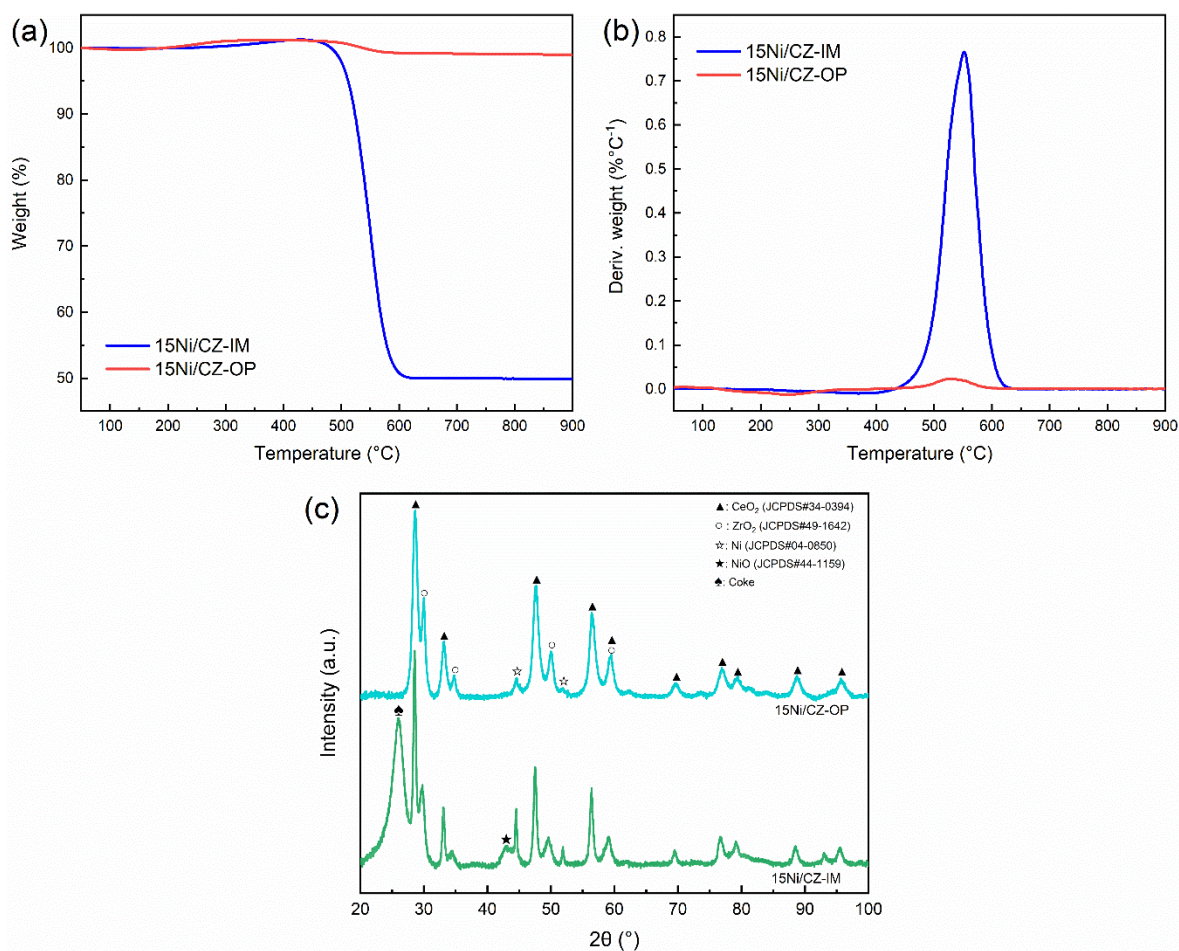


Figure 4.13. (a) TGA, (b) DTG profiles, and (c) XRD patterns of the spent 15Ni/CZ–IM and 15Ni/CZ–OP catalysts after the 30-h ESR at 550°C.

4.4. Conclusions

In this study, the xNi/CZ–OP catalyst exhibited superior catalytic performance in terms of H₂ production rate and coke amount. This could be attributed to the strong metal–support interaction between Ni and CZ, which resulted in highly dispersed active Ni metal in the support and minimized Ce particle size, as confirmed by the XRD analysis. Additionally, Ni was embedded in the CZ lattice, which improved the reducibility due to CeO₂ and increased the concentration of oxygen vacancies. Carbon deposition primarily occurred on the Ni surface via CH₄ decomposition ($\text{CH}_4 \rightarrow 2\text{H}_2 + \text{C}$). Owing to the abundant oxygen vacancies

and highly dispersed active Ni particles in the xNi/CZ–OP catalysts, active oxygen (O^*) could readily migrate to the coke precursor (C^*) on the Ni surface site, thereby facilitating the coke gasification reaction [92]. In contrast, in the xNi/CZ–IM catalysts, the presence of isolated Ni clusters inhibited the interaction between Ni and the CZ support, resulting in a deficiency in the oxygen vacancies and posing difficulties for the migration of O^* to C^* , which promote carbon formation [76].

PART IV - SUMMARY AND RECOMMENDATIONS FOR FUTURE WORK

5.1. Summary

This thesis has focused on the investigation of metal–support interactions and coking behavior over Ni/Ce_xZr_{1-x}Al₂O₃ catalysts for ethanol steam reforming. We extensively investigated the Ni-support interaction through variations in Ni content, alterations in the CeZrO_x/Al₂O₃ ratio, and employing different catalyst preparation methods. By optimizing the interaction between Ni and support, we improved the performance of the ethanol steam reforming (ESR) reaction and mitigated coke formation.

5.1.1 Developments and findings related to research objective 1

For xNi/CeZrO_x–Al₂O₃ (x=5,10,15,20 wt.%), depending on the Ni loading contents, the added Ni selectively interacts with CeZrO_x –Al₂O₃ , resulting in the stepwise locations of Ni over CeZrO_x–Al₂O₃. The selective interaction between Ni and CeZrO_x generates more oxygen vacancies. The Ni sites near the oxygen vacancies enhance reforming via steam activation, resulting in the highest hydrogen production rate. Ni selectively deposited on Al₂O₃ accelerates coking from the ethylene produced on the acidic sites, resulting in a high coke amount.

For optimizing the metal-support interactions in Ni/Ce_xZr_{1-x}O₂–Al₂O₃ catalysts, we applied different CZ/Al compositions (20CZA and 40CZA). 20Ni/20CZA contained large isolated Ni clusters over CZ with a lack of oxygen vacancies due to the limited Ni–CZ interaction over 20Ni/20CZA. The crystalline CZ structure in 40CZA induced a strong

interaction with the Ni species, even at 20 wt% of Ni, resulting in highly dispersed Ni nanoparticles and abundant oxygen vacancies over 20Ni/40CZA. The optimized catalytic properties on active sites over 20Ni/40CZA produced the highest H₂ production rate and minimized the coke amount in ESR. Specifically, the excellent coking resistance of 20Ni/40CZA at 550 °C was ascribed to the generation of O* on abundant oxygen vacancies and the efficient de-livery of O* from oxygen vacancies to C* on Ni over CZ, which resulted in faster gasification of C* than coking to CNTs.

5.1.2 Developments and findings related to research objective 2

Based on the aforementioned investigations, we identified the significance of the interaction between Ni and CeO₂ in the ethanol steam reforming (ESR) reaction. Subsequently, we utilized the Ni/CeZrO_x catalyst and employed various catalyst preparation methods (one-pot method and successive impregnation method) to delve deeper into the interaction between Ni and CeO₂.

Using the one-pot method, the Ni species over the Ni/CZ catalysts strongly interacted with the CZ support, resulting in smaller Ni nanoparticles with abundant oxygen vacancies. The successive impregnation method mainly generated an isolated Ni phase at a high Ni content, resulting in large Ni clusters with limited oxygen vacancies. The poor Ni dispersion over the Ni/CZ catalysts prepared by the successive impregnation method induced low ethanol conversions and hydrogen production rates. The large Ni clusters over the Ni/CZ catalysts prepared by the successive impregnation method achieved a fast-coking behavior, thereby increasing the coke amount. Coke gasification was demonstrated to dominate the Ni

surface with the Ni/CZ catalysts prepared by the one-pot method because of the high Ni dispersion and abundant oxygen vacancies.

5.2 Recommendation for future work

The formation of different types of active sites at the metal/support interface is one of the ways through which the support is believed to influence the reactivity. The amount of sites in the Ni/support interface correlates with the reaction rates for steam activation or coke deposition. Ni-CeO₂ interface (vs bare Ni active site) may provide more energetically favorable reaction pathways [93].

In future work, it is supported to investigate the formation of different types of active sites at the Ni/CeO₂ interface. This entails a comprehensive exploration and comparison between the catalytic activity of Ni-support interface and bare Ni active sites and their effects in the ESR reaction (H₂ production, liquid intermediates, coke generation, CO/CO₂ ratio, CO₂ adsorption on the support). In addition, there is a compelling need to elucidate how the formation of the Ni-support interface influences the morphological characteristics of the catalyst and modulates the interactions between the metal and support. The focus will extend to evaluating the impact of Ni-support interface formation on the acidity of Al₂O₃ and its role in modifying the surface properties that influence the reactivity of active oxygen species and the gasification of carbon precursors. Additionally, an investigation of alterations in the electron density and charge transfer properties of the catalyst associated with the formation of the Ni-support interface will be conducted. The implications of these changes for the ESR

reaction will be thoroughly scrutinized, providing valuable insights into the underlying mechanisms governing the catalytic processes.

References

- [1] W.-H. Chen, P.P. Biswas, A.T. Ubando, Y.-K. Park, V. Ashokkumar, J.-S. Chang, Design of experiment for hydrogen production from ethanol reforming: A state-of-the-art review, *Fuel*, 342 (2023). <https://doi.org/10.1016/j.fuel.2023.127871>.
- [2] F. Johnsson, J. Kjärstad, J.J.C.P. Rootzén, The threat to climate change mitigation posed by the abundance of fossil fuels, 19 (2019) 258-274. <https://doi.org/10.1080/14693062.2018.1483885>.
- [3] V. Goltsov, T. Veziroglu, L. Goltsova, Hydrogen civilization of the future—A new conception of the IAHE, *International Journal of Hydrogen Energy*, 31 (2006) 153-159. <https://doi.org/10.1016/j.ijhydene.2005.04.045>.
- [4] M. Ni, D.Y. Leung, M.K. Leung, K.J.F.p.t. Sumathy, An overview of hydrogen production from biomass, 87 (2006) 461-472. <https://doi.org/10.1016/j.fuproc.2005.11.003>.
- [5] A.M. Ranjekar, G.D. Yadav, Steam reforming of methanol for hydrogen production: A critical analysis of catalysis, processes, and scope, *Industrial & Engineering Chemistry Research*, 60 (2021) 89-113. <https://doi.org/10.1021/acs.iecr.0c05041>.
- [6] L. García, Hydrogen production by steam reforming of natural gas and other nonrenewable feedstocks, *Compendium of Hydrogen Energy* (2015) 83-107. <https://doi.org/10.1016/B978-1-78242-361-4.00004-2>.
- [7] Y. Ma, X.R. Wang, T. Li, J. Zhang, J. Gao, Z.Y. Sun, Hydrogen and ethanol: Production, storage, and transportation, *International Journal of Hydrogen Energy*, 46 (2021) 27330-27348. <https://doi.org/10.1016/j.ijhydene.2021.06.027>.
- [8] R.M. Navarro, M.C. Sánchez-Sánchez, M.C. Alvarez-Galvan, F.d. Valle, J.L.G. Fierro, Hydrogen production from renewable sources: biomass and photocatalytic opportunities, *Energy Environ. Sci.*, 2 (2009) 35-54. <https://doi.org/10.1039/b808138g>.
- [9] Y. Deng, S. Li, L. Appels, H. Zhang, N. Sweygers, J. Baeyens, R. Dewil, Steam reforming of ethanol by non-noble metal catalysts, *Renewable and Sustainable Energy Reviews*, 175 (2023). <https://doi.org/10.1016/j.rser.2023.113184>.
- [10] T. Qin, S. Yuan, Research progress of catalysts for catalytic steam reforming of high temperature tar: A review, *Fuel*, 331 (2023). <https://doi.org/10.1016/j.fuel.2022.125790>.
- [11] D. Liang, Y. Wang, Y. Wang, M. Chen, X. Xie, C. Li, J. Wang, L. Yuan, Dry reforming of methane for syngas production over noble metals modified M-Ni@S-1 catalysts (M = Pt, Pd, Ru, Au), *International Journal of Hydrogen Energy*, (2023). <https://doi.org/10.1016/j.ijhydene.2023.07.135>.
- [12] M. Chen, X. Feng, Y. Wang, D. Liang, C. Li, Z. Yang, J. Wang, Ethanol steam reforming over attapulgite-based MCM-41 supported Ni-Ce-Zr catalyst for hydrogen production, *Fuel*, 346 (2023). <https://doi.org/10.1016/j.fuel.2023.128373>.
- [13] A. Haryanto, Fernando, S., Murali, N., Adhikari, S., Current status of hydrogen production techniques by steam reforming of ethanol: a review, *Energy & Fuels*, 19 (2005) 2098-2106. <https://doi.org/10.1021/ef0500538>.
- [14] L.V. Mattos, G. Jacobs, B.H. Davis, F.B. Noronha, Production of hydrogen from ethanol: review of reaction mechanism and catalyst deactivation, *Chemical reviews*, 112 (2012) 4094-

4123. <https://doi.org/10.1021/cr2000114>.
- [15] J. Contreras, J. Salmones, J. Colín-Luna, L. Nuño, B. Quintana, I. Córdova, B. Zeifert, C. Tapia, G. Fuentes, Catalysts for H₂ production using the ethanol steam reforming (a review), 39 (2014) 18835-18853. <https://doi.org/10.1016/j.ijhydene.2014.08.072>.
- [16] D. Zanchet, J.B.O. Santos, S. Damyanova, J.M.R. Gallo, J.M.C. Bueno, Toward understanding metal-catalyzed ethanol reforming, ACS Catalysis, 5 (2015) 3841-3863. <https://doi.org/10.1021/cs5020755>.
- [17] C. Zhang, S. Li, G. Wu, J. Gong, Synthesis of stable Ni-CeO₂ catalysts via ball-milling for ethanol steam reforming, Catalysis Today, 233 (2014) 53-60. <https://doi.org/10.1016/j.cattod.2013.08.013>.
- [18] J.L. Contreras, J. Salmones, J.A. Colín-Luna, L. Nuño, B. Quintana, I. Córdova, B. Zeifert, C. Tapia, G.A. Fuentes, Catalysts for H₂ production using the ethanol steam reforming (a review), International Journal of Hydrogen Energy, 39 (2014) 18835-18853. <https://doi.org/10.1016/j.ijhydene.2014.08.072>.
- [19] M. Compagnoni, A. Tripodi, I. Rossetti, Parametric study and kinetic testing for ethanol steam reforming, Applied Catalysis B: Environmental, 203 (2017) 899-909. <https://doi.org/10.1016/j.apcatb.2016.11.002>.
- [20] C.K. Cheng, S.Y. Foo, A.A. Adesina, Steam reforming of glycerol over Ni/Al₂O₃ catalyst, Catalysis Today, 178 (2011) 25-33. <https://doi.org/10.1016/j.cattod.2011.07.011>.
- [21] Y. Wang, M. Craven, X. Yu, J. Ding, P. Bryant, J. Huang, X. Tu, Plasma-enhanced catalytic synthesis of ammonia over a Ni/Al₂O₃ catalyst at near-room temperature: Insights into the importance of the catalyst surface on the reaction mechanism, ACS Catal, 9 (2019) 10780-10793. <https://doi.org/10.1021/acscatal.9b02538>.
- [22] S. Soni, S. Kumar, B. Dalela, S. Kumar, P.A. Alvi, S. Dalela, Defects and oxygen vacancies tailored structural and optical properties in CeO₂ nanoparticles doped with Sm³⁺ cation, Journal of Alloys and Compounds, 752 (2018) 520-531. <https://doi.org/10.1016/j.jallcom.2018.04.157>.
- [23] B. Lu, J. Zhuang, J. Du, F. Gu, G. Xu, Z. Zhong, Q. Liu, F. Su, Highly dispersed Ni nanocatalysts derived from NiMnAl-Hydrotalcites as high-performing catalyst for low-temperature syngas methanation, Catalysts, 9 (2019). <https://doi.org/10.3390/catal9030282>.
- [24] Z. Xiao, C. Wu, L. Wang, J. Xu, Q. Zheng, L. Pan, J. Zou, X. Zhang, G. Li, Boosting hydrogen production from steam reforming of ethanol on nickel by lanthanum doped ceria, Applied Catalysis B: Environmental, 286 (2021). <https://doi.org/10.1016/j.apcatb.2021.119884>.
- [25] L.T. Do, E.W. Shin, Reinforcement of steam oxidative cracking of 1-methyl naphthalene by the synergistic combination of hydrogenation and oxidation over nickel-containing mixed oxide catalysts, Journal of Catalysis, 371 (2019) 245-254. <https://doi.org/10.1016/j.jcat.2019.02.001>.
- [26] P. Biswas, D. Kunzru, Steam reforming of ethanol for production of hydrogen over Ni/CeO₂-ZrO₂ catalyst: Effect of support and metal loading, International Journal of Hydrogen Energy, 32 (2007) 969-980. <https://doi.org/10.1016/j.ijhydene.2006.09.031>.
- [27] L. Zhou, L. Li, N. Wei, J. Li, J.-M. Basset, Effect of NiAl₂O₄ formation on Ni/Al₂O₃

- stability during dry reforming of methane, *ChemCatChem*, 7 (2015) 2508-2516. <https://doi.org/10.1002/cctc.201500379>.
- [28] P. Mierczynski, A. Mierczynska, R. Ciesielski, M. Mosinska, M. Nowosielska, A. Czyrkowska, W. Maniukiewicz, M. Szykowska, K. Vasilev, High active and selective Ni/CeO₂-Al₂O₃ and Pd-Ni/CeO₂-Al₂O₃ catalysts for oxy-steam reforming of methanol, *Catalysts*, 8 (2018). <https://doi.org/10.3390/catal8090380>.
- [29] A.L. Alberton, M.M.V.M. Souza, M. Schmal, Carbon formation and its influence on ethanol steam reforming over Ni/Al₂O₃ catalysts, *Catalysis Today*, 123 (2007) 257-264. <https://doi.org/10.1016/j.cattod.2007.01.062>.
- [30] D.G. Araiza, A. Gómez-Cortés, G. Díaz, Effect of ceria morphology on the carbon deposition during steam reforming of ethanol over Ni/CeO₂ catalysts, *Catalysis Today*, 349 (2020) 235-243. <https://doi.org/10.1016/j.cattod.2018.03.016>.
- [31] P. Osorio-Vargas, N.A. Flores-González, R.M. Navarro, J.L.G. Fierro, C.H. Campos, P. Reyes, Improved stability of Ni/Al₂O₃ catalysts by effect of promoters (La₂O₃, CeO₂) for ethanol steam-reforming reaction, *Catalysis Today*, 259 (2016) 27-38. <https://doi.org/10.1016/j.cattod.2015.04.037>.
- [32] T. Klimova, M. Calderón, J. Ramírez, Ni and Mo interaction with Al-containing MCM-41 support and its effect on the catalytic behavior in DBT hydrodesulfurization, *Applied Catalysis A: General*, 240 (2003) 29-40. [https://doi.org/10.1016/S0926-860X\(02\)00417-9](https://doi.org/10.1016/S0926-860X(02)00417-9).
- [33] C.K.S. Choong, Z. Zhong, L. Huang, Z. Wang, T.P. Ang, A. Borgna, J. Lin, L. Hong, L. Chen, Effect of calcium addition on catalytic ethanol steam reforming of Ni/Al₂O₃: I. Catalytic stability, electronic properties and coking mechanism, *Applied Catalysis A: General*, 407 (2011) 145-154. <https://doi.org/10.1016/j.apcata.2011.08.037>.
- [34] L.T. Do, C. Nguyen-Huy, E.W. Shin, Different metal support interactions over NiK/Mixed oxide catalysts and their effects on catalytic routes in steam catalytic cracking of vacuum residue, *ChemistrySelect*, 3 (2018) 1827-1835. <https://doi.org/10.1002/slct.201702819>.
- [35] B. Hoffer, A. Dickvanlangeveld, J. Janssens, R. Bonne, C. Lok, J. Moulijn, Stability of highly dispersed Ni/Al₂O₃ catalysts: Effects of pretreatment, *Journal of Catalysis*, 192 (2000) 432-440. <https://doi.org/10.1006/jcat.2000.2867>.
- [36] T. Sukonket, A. Khan, B. Saha, H. Ibrahim, S. Tantayanon, P. Kumar, R. Idem, Influence of the catalyst preparation method, surfactant amount, and steam on CO₂ reforming of CH₄ over 5Ni/Ce_{0.6}Zr_{0.4}O₂ catalysts, *Energy & Fuels*, 25 (2011) 864-877. <https://doi.org/10.1021/ef101479y>.
- [37] E. Ozensoy, J. Szanyi, C.H. Peden, Interaction of water with ordered θ -Al₂O₃ ultrathin films grown on NiAl (100), *The Journal of Physical Chemistry B*, 109 (2005) 3431-3436. <https://doi.org/10.1021/jp0449206>.
- [38] S. Dekkar, S. Tezkratt, D. Sellam, K. Ikkour, K. Parkhomenko, A. Martinez-Martin, A.C. Roger, Dry reforming of methane over Ni-Al₂O₃ and Ni-SiO₂ Catalysts: Role of preparation methods, *Catalysis Letters*, 150 (2020) 2180-2199. <https://doi.org/10.1007/s10562-020-03120-3>.
- [39] Y. Li, X. Wang, C. Song, Spectroscopic characterization and catalytic activity of Rh

- supported on CeO₂-modified Al₂O₃ for low-temperature steam reforming of propane, *Catalysis Today*, 263 (2016) 22-34. <https://doi.org/10.1016/j.cattod.2015.08.063>.
- [40] X. Li, Q. Li, W. Li, X. Zhang, L. Zhong, C. Zhang, Q. Fang, G. Chen, Enhancement of SCR performance of monolithic Mn–Ce/Al₂O₃/cordierite catalysts by using modified deposition precipitation method, *Asia-Pacific Journal of Chemical Engineering*, 14 (2019). <https://doi.org/10.1002/apj.2318>.
- [41] J. Ashok, N. Dewangan, S. Das, P. Hongmanorom, M.H. Wai, K. Tomishige, S. Kawi, Recent progress in the development of catalysts for steam reforming of biomass tar model reaction, *Fuel Processing Technology*, 199 (2020). <https://doi.org/10.1016/j.fuproc.2019.106252>.
- [42] S. Ahmed, A. Aitani, F. Rahman, A. Al-Dawood, F. Al-Muhaish, Decomposition of hydrocarbons to hydrogen and carbon, *Applied Catalysis A: General*, 359 (2009) 1-24. <https://doi.org/10.1016/j.apcata.2009.02.038>.
- [43] M. Ni, D.Y.C. Leung, M.K.H. Leung, A review on reforming bio-ethanol for hydrogen production, *International Journal of Hydrogen Energy*, 32 (2007) 3238-3247. <https://doi.org/10.1016/j.ijhydene.2007.04.038>.
- [44] J.H. Song, S.J. Han, I.K. Song, Hydrogen production by steam reforming of ethanol over mesoporous Ni–Al₂O₃–ZrO₂ catalysts, *Catalysis Surveys from Asia*, 21 (2017) 114-129. <https://doi.org/10.1007/s10563-017-9230-5>.
- [45] Y. Wang, D. Liang, C. Wang, M. Chen, Z. Tang, J. Hu, Z. Yang, H. Zhang, J. Wang, S. Liu, Influence of calcination temperature of Ni/Attapulgitite on hydrogen production by steam reforming ethanol, *Renewable Energy*, 160 (2020) 597-611. <https://doi.org/10.1016/j.renene.2020.06.126>.
- [46] C. Wu, P.T. Williams, Hydrogen production from steam reforming of ethanol with nano-Ni/SiO₂ catalysts prepared at different Ni to citric acid ratios using a sol–gel method, *Applied Catalysis B: Environmental*, 102 (2011) 251-259. <https://doi.org/10.1016/j.apcatb.2010.12.005>.
- [47] H. Ma, L. Zeng, H. Tian, D. Li, X. Wang, X. Li, J. Gong, Efficient hydrogen production from ethanol steam reforming over La-modified ordered mesoporous Ni-based catalysts, *Applied Catalysis B: Environmental*, 181 (2016) 321-331. <https://doi.org/10.1016/j.apcatb.2015.08.019>.
- [48] F. Rahbar Shamskar, M. Rezaei, F. Meshkani, The influence of Ni loading on the activity and coke formation of ultrasound-assisted co-precipitated Ni–Al₂O₃ nanocatalyst in dry reforming of methane, *International Journal of Hydrogen Energy*, 42 (2017) 4155-4164. <https://doi.org/10.1016/j.ijhydene.2016.11.067>.
- [49] X. Zhai, S. Ding, Z. Liu, Y. Jin, Y. Cheng, Catalytic performance of Ni catalysts for steam reforming of methane at high space velocity, *International Journal of Hydrogen Energy*, 36 (2011) 482-489. <https://doi.org/10.1016/j.ijhydene.2010.10.053>.
- [50] D. Li, L. Zeng, X. Li, X. Wang, H. Ma, S. Assabumrungrat, J. Gong, Ceria-promoted Ni/SBA-15 catalysts for ethanol steam reforming with enhanced activity and resistance to deactivation, *Applied Catalysis B: Environmental*, 176-177 (2015) 532-541. <https://doi.org/10.1016/j.apcatb.2015.04.020>.

- [51] C. Montero, A. Ochoa, P. Castaño, J. Bilbao, A.G. Gayubo, Monitoring Ni⁰ and coke evolution during the deactivation of a Ni/La₂O₃- α -Al₂O₃ catalyst in ethanol steam reforming in a fluidized bed, *Journal of Catalysis*, 331 (2015) 181-192. <https://doi.org/10.1016/j.jcat.2015.08.005>.
- [52] J. Vicente, J. Ereña, C. Montero, M.J. Azkoiti, J. Bilbao, A.G. Gayubo, Reaction pathway for ethanol steam reforming on a Ni/SiO₂ catalyst including coke formation, *International Journal of Hydrogen Energy*, 39 (2014) 18820-18834. <https://doi.org/10.1016/j.ijhydene.2014.09.073>.
- [53] J. Valecillos, S. Iglesias-Vazquez, L. Landa, A. Remiro, J. Bilbao, A.G. Gayubo, Insights into the Reaction Routes for H₂ Formation in the Ethanol Steam Reforming on a Catalyst Derived from NiAl₂O₄ Spinel, *Energy Fuels*, 35 (2021) 17197-17211. <https://doi.org/10.1021/acs.energyfuels.1c01670>.
- [54] M. Wang, S.Y. Kim, Y. Men, E.W. Shin, Influence of metal-support interactions on reaction pathways over Ni/CeZrO_x-Al₂O₃ catalysts for ethanol steam reforming, *International Journal of Hydrogen Energy*, 47 (2022) 33765-33780. <https://doi.org/10.1016/j.ijhydene.2022.07.274>.
- [55] S.Y. Kim, M. Wang, H. Nguyen-Phu, D.H. Jeong, E.W. Shin, Investigating the influence of Ni-Ce_xZr_{1-x}O₂ interaction on oxygen vacancy and catalytic behavior of Ni/Ce_xZr_{1-x}O₂ catalysts for ethanol steam reforming, *Journal of Catalysis*, 416 (2022) 240-252. <https://doi.org/10.1016/j.jcat.2022.11.009>.
- [56] S. Anil, S. Indrajaya, R. Singh, S. Appari, B. Roy, A review on ethanol steam reforming for hydrogen production over Ni/Al₂O₃ and Ni/CeO₂ based catalyst powders, *International Journal of Hydrogen Energy*, 47 (2022) 8177-8213. <https://doi.org/10.1016/j.ijhydene.2021.12.183>.
- [57] C. Sun, P. Summa, Y. Wang, K. Świrk Da Costa, A. Miró i Rovira, S. Casale, K. Świerczek, C. Hu, M. Rønning, P. Da Costa, Boosting CO₂ reforming of methane via the metal-support interaction in mesostructured SBA-16-derived Ni nanoparticles, *Applied Materials Today*, 26 (2022). <https://doi.org/10.1016/j.apmt.2021.101354>.
- [58] Y. Zeng, H. Ma, H. Zhang, W. Ying, D. Fang, Ni-Ce-Al composite oxide catalysts synthesized by solution combustion method: Enhanced catalytic activity for CO methanation, *Fuel*, 162 (2015) 16-22. <https://doi.org/10.1016/j.fuel.2015.08.046>.
- [59] N. Wang, K. Shen, L. Huang, X. Yu, W. Qian, W. Chu, Facile route for synthesizing ordered mesoporous Ni-Ce-Al oxide materials and their catalytic performance for methane dry reforming to hydrogen and syngas, *ACS Catalysis*, 3 (2013) 1638-1651. <https://doi.org/10.1021/cs4003113>.
- [60] M.N. Barroso, A.E. Galetti, M.F. Gomez, L.A. Arrúa, M.C. Abello, Ni-catalysts supported on Zn_xMg_{1-x}Al₂O₄ for ethanol steam reforming: influence of the substitution for Mg on catalytic activity and stability, *Chemical Engineering Journal*, 222 (2013) 142-149. <https://doi.org/10.1016/j.cej.2013.02.051>.
- [61] A. Singhania, S.M. Gupta, Nickel nanocatalyst ex-solution from ceria-nickel oxide solid solution for low temperature CO oxidation, *Journal of Nanoscience and Nanotechnology*, 18 (2018) 4614-4620. <https://doi.org/10.1166/jnn.2018.15342>.

- [62] R. Yang, X. Li, J. Wu, X. Zhang, Z. Zhang, Y. Cheng, J. Guo, Hydrotreating of crude 2-ethylhexanol over Ni/Al₂O₃ catalysts: Surface Ni species-catalytic activity correlation, *Applied Catalysis A: General*, 368 (2009) 105-112. <https://doi.org/10.1016/j.apcata.2009.08.021>.
- [63] J.P. Bortolozzi, T. Weiss, L.B. Gutierrez, M.A. Ulla, Comparison of Ni and Ni-Ce/Al₂O₃ catalysts in granulated and structured forms: Their possible use in the oxidative dehydrogenation of ethane reaction, *Chemical Engineering Journal*, 246 (2014) 343-352. <https://doi.org/10.1016/j.cej.2014.02.078>.
- [64] X. Huang, W. Mo, X. He, X. Fan, F. Ma, D. Tax, Effects of promoters on the structure, performance, and carbon deposition of Ni-Al₂O₃ catalysts for CO₂-CH₄ Reforming, *ACS Omega*, 6 (2021) 16381-16390. <https://doi.org/10.1021/acsomega.1c00918>.
- [65] Q. Wei, X. Gao, L. Wang, Q. Ma, Rational design of nickel-based catalyst coupling with combined methane reforming to steadily produce syngas, *Fuel*, 271 (2020). <https://doi.org/10.1016/j.fuel.2020.117631>.
- [66] F. Tavares, H.O. Mohamed, S.R. Kulkarni, N. Morlanés, P. Castaño, Decreasing the coking and deactivation of a reforming Ni-Ce/Al₂O₃ catalyst with intraparticle SiC in hydrogen production routes, *Fuel*, 337 (2023). <https://doi.org/10.1016/j.fuel.2022.127058>.
- [67] G. Pantaleo, V.L. Parola, F. Deganello, R.K. Singha, R. Bal, A.M. Venezia, Ni/CeO₂ catalysts for methane partial oxidation: Synthesis driven structural and catalytic effects, *Applied Catalysis B: Environmental*, 189 (2016) 233-241. <https://doi.org/10.1016/j.apcatb.2016.02.064>.
- [68] Z. Xiao, Y. Li, F. Hou, C. Wu, L. Pan, J. Zou, L. Wang, X. Zhang, G. Liu, G. Li, Engineering oxygen vacancies and nickel dispersion on CeO₂ by Pr doping for highly stable ethanol steam reforming, *Applied Catalysis B: Environmental*, 258 (2019). <https://doi.org/10.1016/j.apcatb.2019.117940>.
- [69] L. Katta, P. Sudarsanam, G. Thrimurthulu, B.M. Reddy, Doped nanosized ceria solid solutions for low temperature soot oxidation: Zirconium versus lanthanum promoters, *Applied Catalysis B: Environmental*, 101 (2010) 101-108. <https://doi.org/10.1016/j.apcatb.2010.09.012>.
- [70] D. Harshini, D.H. Lee, J. Jeong, Y. Kim, S.W. Nam, H.C. Ham, J.H. Han, T.-H. Lim, C.W. Yoon, Enhanced oxygen storage capacity of Ce_{0.65}Hf_{0.25}M_{0.1}O_{2-δ} (M=rare earth elements): Applications to methane steam reforming with high coking resistance, *Applied Catalysis B: Environmental*, 148-149 (2014) 415-423. <https://doi.org/10.1016/j.apcatb.2013.11.022>.
- [71] F. Hu, S. Tong, K. Lu, C.-M. Chen, F.-Y. Su, J. Zhou, Z.-H. Lu, X. Wang, G. Feng, R. Zhang, Reduced graphene oxide supported Ni-Ce catalysts for CO₂ methanation: The support and ceria promotion effects, *Journal of CO₂ Utilization*, 34 (2019) 676-687. <https://doi.org/10.1016/j.jcou.2019.08.020>.
- [72] K. Pavithra, S.M.S. Kumar, Embedding oxygen vacancies at SnO₂-CNT surfaces via a microwave polyol strategy towards effective electrocatalytic reduction of carbon-dioxide to formate, *Catalysis Science & Technology*, 10 (2020) 1311-1322. <https://doi.org/10.1039/C9CY01960J>.

- [73] C. Kosri, S. Kiatphuengporn, T. Butburee, S. Youngjun, S. Thongratkaew, K. Faungnawakij, C. Yimsukanan, N. Chanlek, P. Kidkhunthod, J. Wittayakun, P. Khemthong, Selective conversion of xylose to lactic acid over metal-based Lewis acid supported on γ - Al_2O_3 catalysts, *Catalysis Today*, 367 (2021) 205-212. <https://doi.org/10.1016/j.cattod.2020.04.061>.
- [74] D.N. Futaba, T. Yamada, K. Kobashi, M. Yumura, K. Hata, Macroscopic wall number analysis of single-walled, double-walled, and few-walled carbon nanotubes by X-ray diffraction, *Journal of The American Chemical Society*, 133 (2011) 5716-5719. <https://doi.org/10.1021/ja2005994>.
- [75] C. Montero, A. Remiro, B. Valle, L. Oar-Arteta, J. Bilbao, A.G. Gayubo, Origin and nature of coke in ethanol steam reforming and its role in deactivation of $\text{Ni/La}_2\text{O}_3$ - $\alpha\text{Al}_2\text{O}_3$ catalyst, *Industrial & Engineering Chemistry Research*, 58 (2019) 14736-14751. <https://doi.org/10.1021/acs.iecr.9b02880>.
- [76] Y.C. Sharma, A. Kumar, R. Prasad, S.N. Upadhyay, Ethanol steam reforming for hydrogen production: Latest and effective catalyst modification strategies to minimize carbonaceous deactivation, *Renewable and Sustainable Energy Reviews*, 74 (2017) 89-103. <https://doi.org/10.1016/j.rser.2017.02.049>.
- [77] Y. Shi, K. Han, F. Wang, Ni-Cu alloy nanoparticles confined by physical encapsulation with SiO_2 and chemical metal-support interaction with CeO_2 for methane dry reforming, *Inorganic Chemistry*, 61 (2022) 15619-15628. <https://doi.org/10.1021/acs.inorgchem.2c02466>.
- [78] S. Lin, J. Wang, Y. Mi, S. Yang, Z. Wang, W. Liu, D. Wu, H. Peng, Trifunctional strategy for the design and synthesis of a $\text{Ni-CeO}_2@/\text{SiO}_2$ catalyst with remarkable low-temperature sintering and coking resistance for methane dry reforming, *Chinese Journal of Catalysis*, 42 (2021) 1808-1820. [https://doi.org/10.1016/S1872-2067\(21\)63789-0](https://doi.org/10.1016/S1872-2067(21)63789-0).
- [79] Ni J, Leng W, Mao J, et al. Tuning electron density of metal nickel by support defects in Ni/ZrO_2 for selective hydrogenation of fatty acids to alkanes and alcohols, *Applied Catalysis B: Environmental*, 253 (2019) 170-178. <https://doi.org/10.1016/j.apcatb.2019.04.043>.
- [80] Zhou G, Barrio L, Agnoli S, et al. High activity of $\text{Ce}_{1-x}\text{Ni}_x\text{O}_{2-y}$ for H_2 production through ethanol steam reforming: tuning catalytic performance through metal-oxide interactions, *Angewandte Chemie International Edition*, 49(50) (2010) 9680-9684. <https://doi.org/10.1002/anie.201004966>.
- [81] C. Italiano, J. Llorca, L. Pino, M. Ferraro, V. Antonucci, A. Vita, CO and CO_2 methanation over Ni catalysts supported on CeO_2 , Al_2O_3 and Y_2O_3 oxides, *Applied Catalysis B: Environmental*, 264 (2020) 118494. <https://doi.org/10.1016/j.apcatb.2019.118494>.
- [82] Zhang S, Muratsugu S, Ishiguro N, et al. Ceria-doped Ni/SBA-16 catalysts for dry reforming of methane, *Acs Catalysis*, 3(8) (2013) 1855-1864. <https://doi.org/10.1016/j.apcatb.2019.118494>.
- [83] A.L.A. Marinho, F.S. Toniolo, F.B. Noronha, F. Epron, D. Duprez, N. Bion, Highly active and stable Ni dispersed on mesoporous CeO_2 - Al_2O_3 catalysts for production of syngas by dry reforming of methane, *Applied Catalysis B: Environmental*, 281 (2021) 119459. <https://doi.org/10.1016/j.apcatb.2020.119459>.
- [84] Barrio L, Kubacka A, Zhou G, et al. Unusual physical and chemical properties of Ni in

- Ce_{1-x}Ni_xO_{2-y} oxides: Structural characterization and catalytic activity for the water gas shift reaction, *The Journal of Physical Chemistry C*, 114:29 (2010) 12689-12697. <https://doi.org/10.1021/jp103958u>.
- [85] D. Kim, K. Stowe, F. Muller, W. Maier, Mechanistic study of the unusual catalytic properties of a new NiCe mixed oxide for the CO₂ reforming of methane, *Journal of Catalysis*, 247 (2007) 101-111. <https://doi.org/10.1016/j.jcat.2007.01.011>.
- [86] Y. Lyu, J. Jocz, R. Xu, E. Stavitski, C. Sievers, Nickel speciation and methane dry reforming performance of Ni/Ce_xZr_{1-x}O₂ prepared by different synthesis methods, *ACS Catalysis*, 10 (2020) 11235-11252. <https://doi.org/10.1021/acscatal.0c02426>.
- [87] F. Zhang, Z. Liu, X. Chen, N. Rui, L.E. Betancourt, L. Lin, W. Xu, C.-j. Sun, A.M.M. Abeykoon, J.A. Rodriguez, J. Teržan, K. Lorber, P. Djinović, S.D. Senanayake, Effects of Zr doping into ceria for the dry reforming of methane over Ni/CeZrO₂ catalysts: In Situ studies with XRD, XAFS, and AP-XPS, *ACS Catalysis*, 10 (2020) 3274-3284. <https://doi.org/10.1021/acscatal.9b04451>.
- [88] Z. Ni, X. Djitcheu, X. Gao, J. Wang, H. Liu, Q. Zhang, Effect of preparation methods of CeO₂ on the properties and performance of Ni/CeO₂ in CO₂ reforming of CH₄, *Scientific Reports*, 12 (2022) 5344. <https://doi.org/10.1038/s41598-022-09291-w>.
- [89] H. Tian, C. Pei, Y. Wu, S. Chen, Z.-J. Zhao, J. Gong, Tunable metal-oxide interaction with balanced Ni⁰/Ni²⁺ sites of Ni Mg_{1-x}O for ethanol steam reforming, *Applied Catalysis B: Environmental*, 293 (2021) 120178. <https://doi.org/10.1016/j.apcatb.2021.120178>.
- [90] C. Sun, K. Świrk, Y. Wang, K.S. Scheidl, D.W. Breiby, M. Rønning, C. Hu, P. Da Costa, Tailoring the yttrium content in Ni-Ce-Y/SBA-15 mesoporous silicas for CO₂ methanation, *Catalysis Today*, 382 (2021) 104-119. <https://doi.org/10.1016/j.cattod.2021.07.031>.
- [91] X. Jia, X. Zhang, N. Rui, X. Hu, C.-j. Liu, Structural effect of Ni/ZrO₂ catalyst on CO₂ methanation with enhanced activity, *Applied Catalysis B: Environmental*, 244 (2019) 159-169. <https://doi.org/10.1016/j.apcatb.2018.11.024>.
- [92] C. Zhang, P. Zhang, S. Li, G. Wu, X. Ma, J. Gong, Superior reactivity of skeletal Ni-based catalysts for low-temperature steam reforming to produce CO-free hydrogen, *Physical Chemistry Chemical Physics*, 14 (2012). <https://doi.org/10.1039/C2CP24059A>.
- [93] L. Foppa, T. Margossian, S.M. Kim, C. Muller, C. Coperet, K. Larmier, A. Comas-Vives, Contrasting the role of Ni/Al₂O₃ interfaces in water-gas shift and dry reforming of methane, *Journal of the American Chemical Society*, 139 (2017) 17128-17139. <https://doi.org/10.1021/jacs.7b08984>.

LIST OF PUBLICATIONS

1. **Wang M**, Kim S Y, Men Y, et al. Influence of metal-support interactions on reaction pathways over $\text{Ni/CeZr}_x\text{-Al}_2\text{O}_3$ catalysts for ethanol steam reforming[J]. International Journal of Hydrogen Energy, 2022, 47(79): 33765-33780.
2. Kim S Y^{*}, **Wang M**^{*}, Nguyen-Phu H, et al. Investigating the influence of Ni- $\text{Ce}_x\text{Zr}_{1-x}\text{O}_2$ interaction on oxygen vacancy and catalytic behavior of $\text{Ni/Ce}_x\text{Zr}_{1-x}\text{O}_2$ catalysts for ethanol steam reforming[J]. Journal of Catalysis, 2022, 416: 240-252.
3. **Wang M**, Kim S Y, Jamsaz A, et al. Effect of active sites distributions on temperature dependent-coke formation over $\text{Ni/Ce}_x\text{Zr}_{1-x}\text{O}_2\text{-Al}_2\text{O}_3$ catalysts for ethanol steam reforming: coke precursor gasification[J]. Applied Surface Science, 2023: 158746.
4. **Wang M**, Kim S Y, Jamsaz A, et al. Metal-support interactions over $\text{Ni/CeO}_2\text{-ZrO}_2$ catalysts for ethanol steam reforming and their effects on the coke gasification[J]. Catalysis Today, 2024, 425: 114341.
5. Jamsaz A, Pham-Ngoc N, **Wang M**, et al. Synergistic effect of macroporosity and crystallinity on catalyst deactivation behavior over macroporous $\text{Ni/Ce}_x\text{Zr}_{1-x}\text{O}_2\text{-Al}_2\text{O}_3$ for dry reforming of methane[J]. Chemical Engineering Journal, 2023, 476: 146821.